Aashish Sah

IMPLEMENTATION OF QUANTUM DRIVING OF SUPERCONDUCTING QUBIT FOR GATE ERROR ANALYSIS

ABSTRACT

Aashish Sah: Implementation of quantum driving of superconducting qubit for gate error analysis
Master's thesis
Tampere University
Science and Engineering, M.Sc.
December 2020

Quantum computers possesses an inherent parallelism that allows for an exponential speedup in carrying out certain tasks compared to classical computers. Superconducting-circuit, a promising candidate for the physical implementation of a qubit from a non-linear LC oscillator, where the nonlinearity is introduced by the Josephson junction. The state of the qubit is controlled by a single-mode electromagnetic field, which is stored in a coplanar waveguide resonator. Consequently, desired gate operation can be performed on the qubit by applying microwave pulse through the drive resonator for a certain interaction time. The quality of the gate operation, measured by the gate error, depends on the properties of the microwave pulse such as amplitude, phase and interaction time.

Essentially, the goal is to build a fault-tolerant quantum computer, which employs a large number of physical qubits for the implementation of error correction codes, in particular surface codes. Consequently, large number of physical qubits consumes significant amount of energy. However, by minimizing the intrinsic sources of error such as state preparation, measurement errors and imperfect gate operation, one can significantly decrease the required number of physical qubits for the execution of surface codes.

In this thesis, we focus on improving the error from the Pauli-X gate operation by optimizing the drive state of the resonator. Traditionally, a classical drive is used to implement the Pauli-X gate rotation. Alternatively, we propose a quantum driving of the qubit, where the description of the classical field is replaced by the quantum approximation of the classical field, namely, coherent drive state. A coherent state is characterized by the average photon number $\bar{n}$, thus we investigate a relationship between average photon number and the performance of the gate operation, numerically and experimentally.

We observe from numerical simulations that by increasing the average photon number in the drive resonator, the gate error is significantly reduced. With an average photon occupation $\bar{n} = 120$, we obtain a gate error of $\varepsilon = 0.41\,\%$. Additionally, we further improve the gate error by decreasing the coupling strength g between the qubit and the drive.

For quantum driving experiments, we design a superconducting-circuit with a qubit–resonator coupling of $g/2\pi = 7.5\,\mathrm{MHz}$. The experimental characterization of the sample yields a enhanced qubit lifetime $T_1 \sim 26\,\mu\mathrm{s}$ and dephasing time $T_2 \sim 5\,\mu\mathrm{s}$. Furthermore, a photon number calibration is carried out using power spectroscopy of the qubit. The results of photon calibration measurement are essential for the implementation of the full gate operation protocol, which will be conducted in the future.

Keywords: Quantum computing, superconducting circuit, quantum driving, gate error

PREFACE

I offer my earnest gratitude to Assoc. Prof. Mikko Möttönen for providing me with an exciting opportunity to work on this thesis, which was carried out in the Quantum Computing and Devices (QCD) group in the Department of Applied Physics at Aalto University.

I would like to convey my sincere thanks to Assoc. Prof. Tapio Niemi and Dr. Jouko Nieminen for officially supervising this thesis at Tampere University. I am eternally grateful for all the meaningful discussions we have had over the course of this thesis and in general, during my stay at Tampere University. Their guidance have definitely nurtured and prepared me for a hopeful future in scientific work. I would also like to acknowledge Prof. Marco Ornigotti for the encouraging discussion on quantum optics, which has helped me to understand circuit quantum electrodynamics with a refined detail.

I would like to thank M.Sc. Aarne Keränen for his insightful suggestions and comments on this thesis. I would also like to thank Dr. Suman Kundu for the stimulating discussions on just about any topic related to this thesis. I would also like to offer my sincere appreciation to M.Sc. Timm Mörstedt and M.Sc. Andras Marton Gunyho for all their help during my time in the QCD group. In addition, I would like to take this opportunity to thank all the past and present members of the QCD group, whose significant contributions in organising the lab-related tasks has helped me conduct my work mostly remotely. The proper documentation of all the relevant work has definitely been a blessing, especially during pandemic measures enforced on the campus.

Finally, I express my sincere gratitude to my family and friends for their continuing support all this time. Last but not the least, I thank Daria for her immense help with just about everything.

Tampere, 30th December 2020

Aashish Sah

CONTENTS

LIST OF SYMBOLS AND ABBREVIATIONS

$\hat{a}^{\dagger}$	annihilation operator
K_{B}	Boltzmann's constant
$\lvert n \rangle$	coherent state
$[a, b] = ab - ba$	commutation relation
$\hat{a}$	creation operator
I_{C}	critical current of the Josephson Junction
CPW	coplanar waveguide
CQED	cavity quantum electrodynamics
cQED	circuit quantum electrodynamics
χ	dispersive shift
$\hat{\rho} = \lvert \psi \rangle \langle \psi \rvert$	density operator
Δ	detuning between the transmon and the resonator
$\hat{D}(\alpha)$	displacement operator
ω_{dr}	driving resonator frequency
E_{C}	charging energy
e	electron's charge
ε	error resulting from the gate operation
F	fidelity
ϕ_0	flux quantum
$\lvert n \rangle$	Fock state
$\omega_{\mathrm{ge}} = \omega_{\mathrm{q}}$	transmon or qubit frequency
g	vacuum Rabi coupling constant
n_{g}	gate charge
$\hat{H}_{\mathrm{int}}^{I}$	interaction Hamiltonian in the interaction picture
C_{J}	Josephson Junction capacitance
E_{J}	Josephson coupling energy
L_{J}	Josephson inductance

JC	Jaynes–Cummings
JJ	Josephson junction
$\bar{n}$	average photon number
$\hat{\sigma}_{\mathrm{x}}$	Pauli-X gate, $\begin{bmatrix} 0 & 1 \\ 1 & 0 \end{bmatrix}$
$\hat{\sigma}_{\mathrm{y}}$	Pauli-Y gate, $\begin{bmatrix} 0 & -i \\ i & 0 \end{bmatrix}$
$\hat{\sigma}_{\mathrm{z}}$	Pauli-Z gate, $\begin{bmatrix} 1 & 0 \\ 0 & -1 \end{bmatrix}$
Tr_{E}	partial trace
t_{π}	π-pulse length
$\omega(t)$	microwave pulse amplitude in Hz
n_{g}	normal state resistance measured at room temperature
ω_{r}	readout resonator frequency
RF	radio frequency
I_{S}	super-current of the Josephson Junction
SS	sweet spot
$\mathrm{Tr}(A)$	trace of a matrix A, $\mathrm{Tr}(\mathrm{A}) = \sum_i A_{ii}$
$\mathrm{Tr}(\hat{O})$	trace of an operator O, $\mathrm{Tr}(\hat{O}) = \sum_i \langle i | \hat{O} | i \rangle$
T_2	dephasing time
T_1	relaxation time
TWPA	traveling wave parametric amplifier

1 INTRODUCTION

At first, information may sound a very abstract concept, but at a fundamental level, it is represented by physical devices that are governed by the laws of physics [1]. All computations are carried out on a physical entity by manipulating the associated physical degrees of freedom. Naturally, an inevitable quest for a physical system that implements large amount of computations by requiring a minimum amount of energy possible was pursued by scientists from all fields alike. Physicist Rolf Landauer approached the problem from the thermodynamics standpoint by studying the minimum energy needed to store a bit of information [2]. Following the work established by Landauer, Paul Benioff and Charles Bennett formalized the theory of computation in the framework of thermodynamics and proposed a quantum system for computation and information processing in their seminal papers [3, 4], respectively. Thus, the idea of quantum computers came to existence for the first time around 1980.

Around the same time, Richard Feynman contributed to the on-going discussions on quantum computers with a slightly different perspective. Feynman puts forward an insightful idea of simulating the evolution of a quantum system by mapping the problem to another quantum system realized as an universal quantum computer [5]. Accordingly, the need for a quantum computer is stemmed from an exponential complexity that comes about when simulating a Hilbert space of even an elementary problem in quantum mechanics. Therefore, by harnessing the quantum degrees of freedom like superposition, in principle, computations on a quantum computer can outperform a classical computer. This gave rise to a novel field of quantum computation and information processing.

Astonishingly, a simple algorithm exploiting the inherent advantages of quantum mechanics proved to perform substantially faster than an equivalent classical algorithm in solving a hypothetical problem [6]. This raised interest in researchers of different backgrounds for testing the performance of quantum algorithms. Quantum algorithm that offers an exponential speedup in taking discrete logarithms and factoring of large numbers [7], and an algorithm offering a quadratic speedup in searching an unstructured large dataset were soon introduced [8]. Furthermore, Shor's factoring algorithm culminated a rich field of research in quantum cryptography, offering an inherently secure communications compared to an existing classical cryptography protocols [9, 10].

The quantum algorithms discussed above are only the manifestation of a rigorous mathematical studies and must be validated experimentally. Surely, we require a physical hardware implemented as a quantum computer to perform and validate these algorithms. A suitable candidate for the physical implementation of a quantum computer must satisfy the DiVincenzo criteria listed in ref. [11]. There are numerous promising candidates for the realization of a physical quantum computer, where the unit of a quantum information (qubit) is implemented as trapped ions [12] and anyons [13, 14], quantum dots [15], nuclear spin [16], photon polarization [17], and superconducting circuit [18, 19, 20] to name a few. Each of these physical systems have some advantages and disadvantages over the others.

While researchers have demonstrated a simplified version of Shor's algorithm using a nuclear spin quantum computer [21], there has not yet been much progress otherwise in the experimental implementation of aforementioned algorithms. Recently, Google achieved a so-called quantum supremacy by sampling the output of a pseudo-random quantum circuit in 200 s, where a classical computer would have taken approximately 10,000 y [22]. Even though the tackled problem did not bear much practical significance to the real-world applications, the achievement does serve as a testimony to the strength of quantum computers.

Superconducting quantum computers have attracted a significant interest from both industries and academia. They offer tremendous advantage over many other candidates in terms of scalability and reproducibility, owing it to an existing state-of-the-art microfabrication technology. In addition, superconducting circuits allow for a good measurement and control of the qubits. However, there are certain weaknesses, such as limitations in identification and characterization of the decoherence sources in the superconducting circuit and non-uniformity in the design of the qubit introduced by the fabrication processes. These issues need to be addressed in order for superconducting quantum computer to succeed as a viable candidate.

In order to perform basic quantum operations for computational purposes, a qubit must be coupled to a system that can prepare, control and measure the state of the qubit. Consequently, the coupling of the qubit to an external system also induces decoherence that makes the qubit inherently a very fragile entity, despite its underlying physical implementation. As a result, when performing a quantum operation, decoherence induced by the system may contribute to drastic errors. In addition, the errors may originate from an imprecise control of the qubit, imperfect state preparation or the measurement of the state of the qubit. For a quantum computer to be able to perform any arbitrary computations, the quantum operations must be below certain error threshold such that the error correction codes may be applied to facilitate fault-tolerant quantum computation [23, 24].

In recent years, a tremendous amount of work has been carried out to perfect a su-

perconducting circuit, where decoherence-induced relaxation and dephasing time have improved significantly compared to its earlier versions [25, 26]. In this thesis, we have utilized one such widely used superconducting qubit, a transmon qubit, that allowed us to obtain the relaxation time of approximately 26 µs and the dephasing time of about 5 µs. This is a substantial enhancement compared to the 2-ns lifetime of the Cooper pair box, which was the first type of a superconducting qubit [27].

The enhanced lifetime of the transmon has allowed for a fault-tolerant quantum computation using the surface codes, an error correction code for superconducting qubits [28]. The physical implementation of the surface code requires a large number of physical qubits. Therefore, it consumes a significant amount of energy. However, one can essentially decrease the number of physical qubits remarkably by further improving the error resulting from the quantum operation. In this thesis, we attempt to minimize the error by optimizing the methods that allow for a precise control of the qubit. To that extent, we outline the theoretical framework used in the course of this thesis in chapters 2 and 3. The methods developed for a comprehensive study of the task at hand are described in chapter 4. The results and the discussions are presented in chapters 5 and 6, respectively.

In chapter 2, we provide a set of mathematical tools necessary for a quantum-mechanical description of superconducting circuits. In particular, we adopt the density operator formalism of the quantum mechanics to describe an interacting quantum system, and present a recipe for the quantization of a harmonic oscillator. Additionally, we briefly layout the important concepts of quantum computation and information processing. Chapter 3 introduces a quantum theory of superconducting circuits, often called circuit quantum electrodynamics (cQED). cQED, essentially, is a study of light–matter interaction, where the matter corresponds to a superconducting qubit and light refers to a single-mode electromagnetic field sustained inside a coplanar waveguide resonator. The interaction between the qubit and the waveguide facilitates a quantum (gate) operation, which we are aiming to optimize for the minimization of the gate error. Therefore, we study the coupled Hamiltonian under different approximations to obtain an optimal interaction time for the Pauli-X gate rotation, corresponding to a bit flip quantum operation.

In chapter 4, we present numerical schemes for the implementation of the Pauli-X gate and devise methods to minimize the gate error. For experiments, we design a superconducting circuit using an electromagnetic simulation software. We briefly discuss the measurement setup and propose a gate protocol for quantum driving experiments. In chapter 5, we examine the numerical results and observe an improvement in the gate error with a higher photon occupation in the drive resonator and a smaller coupling of the drive to the qubit. Additionally, experimental results from the sample characterization and photon calibration measurements are presented. Finally, in chapter 6, the work carried out during the course of the thesis is summarized and remarks on future development are briefly discussed.

2 GENERAL THEORETICAL BACKGROUND

In this section, we present the theoretical background in the framework of cavity and circuit quantum electrodynamics. At first, we briefly outline the density operator formalism of quantum mechanics as opposed to the state vector formalism. Then, we describe the quantization procedure for a harmonic oscillator, which turned out to be an essential tool in this thesis work. Finally, we introduce some important concepts on quantum information theory that are central to the theme of this thesis.

2.1 Density operator formalism

The predictions of quantum mechanics go beyond the classical intuition that we inherit from the observations we make in our everyday life. Therefore, instead of relying on our intuition, we resort to the postulates of quantum mechanics to provide us a set of mathematical rules to study quantum systems. However, there exist different formulations of postulates of quantum theory that lead to same mathematical idea but introduce different physical interpretation [29]. In this thesis, we adopt the postulates formulated by the Copenhagen interpretation. We introduce the postulate for both closed and open quantum system as it is needed to describe interacting and non-interacting quantum systems.

The postulates are formulated in the following way: (i) a physical state of an isolated quantum system is represented by a unit vector in a Hilbert space $\mathcal{H}$, a complex vector space equipped with a scalar inner product, and (ii) the dynamics of the quantum state is governed by the Schrödinger equation [30].

These postulates described in terms of a state vector only prescribe a closed quantum system, one that does not interact with the environment. For all practical purposes, we require an open quantum system, one that can be examined through the environment for information processing. This is true for all quantum systems under experimental investigation.

Density operator formalism introduced by John von Neumann provides an excellent description of an open system. The density operator formalism describes the dynamics of a pure state, which represents a complete information about a physical state as well as mixed state that corresponds to an incomplete information of a physical state [31]. We

present the mathematical formulation of the postulates in the density operator formalism.

The density operator of a system is defined as [30]

$$\hat{\rho} = \sum_i p_i \left| \psi_i \right\rangle \left\langle \psi_i \right|, \tag{2.1}$$

where $\{p_i\}$ are the probabilities of the system being in the states $\{\left| \psi_i \right\rangle\}$ upon a measurement. The density operator must: be self-adjoint, have non-negative spectrum and have a unit trace. The density operator formalism also allows us to quantify degree of "pureness" of a physical state. The density operator agrees with the inequality $\mathrm{Tr}(\hat{\rho}^2) \leq 1$, yielding equality if and only if $\hat{\rho}$ is a pure state. A completely mixed state has equal probabilities for all the states $\{\left| \psi_i \right\rangle\}$.

In density operator formalism, the expected value of an operator A is given by

$$\langle \hat{A} \rangle = \mathrm{Tr}(\hat{\rho} A). \tag{2.2}$$

The temporal evolution of the density operator is given by the Liouville–von Neumann equation [32]

$$i\hbar \frac{\mathrm{d}}{\mathrm{d}t} \hat{\rho}(t) = [\hat{H}(t), \hat{\rho}(t)], \tag{2.3}$$

where the self-adjoint $\hat{H}$ is a Hamiltonian operator. For a time-independent Hamiltonian, the solution of the Liouville–von Neumann yields unitary evolution

$$\hat{\rho}(t) = \hat{\mathcal{U}}(t) \rho(0) \hat{\mathcal{U}}^\dagger(t), \tag{2.4}$$

with the unitary operator

$$\hat{\mathcal{U}}(t) = \exp \left[-\frac{i}{h} \int_0^t \hat{H}(t') \mathrm{d}t' \right]. \tag{2.5}$$

In the framework of open quantum systems, we consider a quantum system and the environment together as a closed system. In our discussion, we regard the system to be open because we are only interested in the detailed description of the evolution of the system and not the environment. Thus, we average out the degrees of freedom of the environment and study the resulting effective evolution of the system.

We present a quantum operation namely, partial trace to implement the averaging of the environmental degrees of freedom and define the reduced density operator of the bipartite system $\mathcal{H} = \mathcal{H}_{\mathbf{S}} \otimes \mathcal{H}_{\mathbf{E}}$ for the description of the system of interest. For $\hat{\rho} \in \mathcal{H}$, the reduced density operator describing the system is given by $\hat{\rho}_{\mathrm{S}} = \mathrm{Tr}_{\mathrm{E}}(\hat{\rho})$. Partial trace

$\mathrm{Tr_E}$ is the trace averaging out environmental degrees of freedom and is defined by [32]

$$\mathrm{Tr_E}(\hat{\rho}) = \sum_j \big(\hat{\mathbb{1}} \otimes \langle j|\big) \hat{\rho} \big(\hat{\mathbb{1}} \otimes |j\rangle\big). \tag{2.6}$$

where $\{|j\rangle\} \in \mathcal{H_E}$ are the basis states of the environment and the identity operator $\hat{\mathbb{1}} \in \mathcal{H_S}$.

2.2 Quantum harmonic oscillator

In our discussion above, we have kept the definition of a quantum system and the environment to an abstract level. In this thesis, we are utilizing a superconducting-circuit to physically realize a two-level quantum system as a qubit and a quantized electromagnetic field as the environment. Interestingly, both the qubit and the quantized electromagnetic field are described as harmonic oscillators but in a quantum regime. Thus, motivated by this necessity, we provide a recipe to quantize a harmonic oscillator and use the recipe later to describe both the system and its environment.

The Hamiltonian formalism[1] is central to the discussion of a quantum system, especially when it comes to the quantization procedure given that the eigenfrequency of the Hamiltonian is known. Hamiltonian of an harmonic oscillator in the classical case is well-known and given by

$$H = \frac{p^2}{2m} + \frac{x^2}{2}m\omega^2. \tag{2.7}$$

Equation (2.7) manifests itself into simple harmonic motion of a particle with mass *m* in a quadratic potential with an angular frequency ω. In order to describe quantum harmonic oscillator instead of a classical one, we promote the coordinate x and its conjugate momentum p to operators through canonical quantization $x \to \hat{x}; p \to \hat{p} = \frac{\hbar}{\mathrm{i}}\frac{\partial}{\partial \hat{x}}$. Substituting these changes into equation (2.7) yields

$$\hat{H} = \frac{\hat{p}^2}{2m} + \frac{\hat{x}^2}{2}m\omega^2, \tag{2.8}$$

which is a standard form for a quantum harmonic oscillator with the commutation relation $[\hat{x}, \hat{p}] = \mathrm{i}\hbar$. The eigenvalue spectrum of equation (2.8) can typically be obtained from the Schrödinger equation using a wavefunction either in the position or momentum representation. Alternatively, we can study and produce the same eigenvalue spectrum in a representation-free manner by adopting the Dirac formalism [34].

To generate the spectrum of a quantum harmonic oscillator in the Dirac formalism, we introduce dimensionless operators $\hat{X} = \sqrt{\frac{m\omega}{\hbar}}\hat{x}$ and $\hat{P} = \sqrt{\frac{1}{\hbar m\omega}}\hat{p}$ with the commutation

---

[1]A detailed discussion of the Hamiltonian formalism can be found in any classical mechanics textbook such as [33].

relation $[\hat{X}, \hat{P}] = \mathrm{i}$ and express the Hamiltonian in terms of $\hat{X}$ and $\hat{P}$: $\hat{H} = \frac{1}{2}\hbar\omega(\hat{X}^2 + \hat{P}^2)$. Then, by introducing the annihilation and creation operators $\hat{a} = \frac{1}{\sqrt{2}}(\hat{X} + \mathrm{i}\hat{P})$ and $\hat{a}^\dagger = \frac{1}{\sqrt{2}}(\hat{X} - \mathrm{i}\hat{P})$ with the commutation relation $[\hat{a}, \hat{a}^\dagger] = 1$, we obtain the Hamiltonian of a quantum harmonic oscillator

$$\hat{H} = \hbar\omega\left(\hat{a}^\dagger\hat{a} + \frac{1}{2}\right). \tag{2.9}$$

The annihilation and creation operators $\hat{a}$ and $\hat{a}^\dagger$ respectively are non-Hermitian operators and therefore, do not correspond to any physical observables. However, all physical observables can be expressed in terms of $\hat{a}$ and $\hat{a}^\dagger$. The eigenvalue spectrum of the Hamiltonian is thus simplified to the spectrum of the number operator $\hat{N} \equiv \hat{a}^\dagger\hat{a}$. The spectrum of $\hat{N}$ is obtained from the commutation relations $[\hat{N}, \hat{a}] = -\hat{a}$ and $[\hat{N}, \hat{a}^\dagger] = \hat{a}^\dagger$ and is given by [34]

$$\hat{N}|n\rangle = n|n\rangle, \; n = 0, 1, 2\ldots, \tag{2.10}$$

where $\{|n\rangle\}$ represents the Fock or number states. By limiting the discussion to number states, we successfully attain a discrete eigenenergy spectrum for the quantum harmonic oscillator

$$\hat{H}|n\rangle = E_n|n\rangle, \tag{2.11}$$

where $E_n = \hbar\omega(n + \frac{1}{2})$. It is important to observe that the energy spacing of the adjacent levels is equal. This observation will play an important role in the design of the qubit.

The apparent naming convention for the creation and the annihilation operators can readily be seen from their actions on the Fock state

$$\hat{a}|n\rangle = \sqrt{n}|n-1\rangle, \tag{2.12}$$
$$\hat{a}^\dagger|n\rangle = \sqrt{n+1}|n+1\rangle. \tag{2.13}$$

We observe that the annihilation operator destroys an excitation, whereas the creation operator promotes an excitation. Additionally, the equation (2.13) reflects that the number states $|n\rangle$ can be generated from the vacuum state through the repeated action of the creation operator [35]

$$|n\rangle = \frac{\hat{a}^\dagger}{\sqrt{n!}}|0\rangle. \tag{2.14}$$

2.3 Quantum information

In classical information theory, the formulation of algorithms and gate operations does not rely on the exact physical implementation of a Boolean bit. Similarly, quantum informa-

tion theory disregards the intricate details of a physical qubit in order to describe simple quantum operations or complex algorithms. In this section, we tailor our discussion of this dense field to fit the necessary details required to follow this thesis. In particular, we introduce a mathematical description of a single qubit, and also provide a tool, namely, Bloch sphere for the visualization of the state of the qubit. Furthermore, we briefly discuss single quantum gates and the fidelity of the gate operation.

2.3.1 Qubits

In quantum information theory, an equivalent description of a boolean bit is given by a qubit. While a bit only takes values in $\{0, 1\}$, a qubit is essentially defined in a two-dimensional complex vector space $\mathbb{C}^2$ and can take infinitely many distinct states. Mathematically, we observe this in Dirac notation as

$$|\psi\rangle = \alpha |0\rangle + \beta |1\rangle, \tag{2.15}$$

where $\{|0\rangle, |1\rangle\}$ are the computational basis states that may correspond to, for example, the ground and the excited state of a truncated two-level system, and $\alpha, \beta \in \mathbb{C}$ are the coefficients and often called probability amplitudes. When the qubit is measured, it collapses to either state $|0\rangle$ or state $|1\rangle$ with probabilities $|\alpha|^2$ or $|\beta|^2$, respectively. The probability amplitude must satisfy the condition $|\alpha|^2 + |\beta|^2 = 1$. Mathematically speaking, the superposition allows an infinite amount of information to be stored on a qubit, since there are infinite possibilities to form a superposition state. However, the measurement of the qubit collapses it to either $|0\rangle$ or $|1\rangle$, thus preventing any apparent paradoxes that may arise from such a description [30].

2.3.2 Bloch sphere

One can build a nice intuition of operations performed on a single qubit using a graphical representation. Utilizing the condition $|\alpha|^2 + |\beta|^2 = 1$, one can parameterize the qubit state up to an irrelevant global phase factor using polar (θ) and azimuthal (φ) angles on a three-dimensional coordinate system. This can readily be expressed as

$$|\psi\rangle = \cos\left(\frac{\theta}{2}\right) |0\rangle + e^{i\varphi} \sin\left(\frac{\theta}{2}\right) |1\rangle, \tag{2.16}$$

where the angles (θ, φ) define a point on the unit sphere, also known as Bloch sphere. In addition to aiding in a nice visual representation of a single qubit state, Bloch sphere provides a powerful tool to represent simple gate operations through rotations around the principle coordinate axes, see figure 3.8b.

It is useful to express the qubit in the density operator form to accommodate the discus-

sion of pure and mixed states. Thus, we write the state in the density operator form [30]

$$\hat{\rho}_{\mathrm{q}} = \frac{1}{2}\left(\hat{\mathbb{1}} + \sum_{i=\mathrm{x,y,z}} \hat{\sigma}_i u_i \right), \tag{2.17}$$

where $\hat{\mathbb{1}}$ is the identity operator, $\hat{\sigma}_i$ represent Pauli operators, and u_i are the components of a real vector $\mathbf{u} \in \mathbb{R}^3$, which is referred to as Bloch vector. The Bloch vector satisfies the condition $\mathbf{u} \leq 1$, where the equality corresponds to the pure state and the inequality defines a mixed state. Thus, one can visualize the pure state as points on the surface of the Bloch sphere, while the mixed states as points inside of the sphere.

One of the most important results that we obtain from the discussion of the Bloch sphere and the qubit in density operator form is the relationship between the expected value of the Pauli vector $\hat{\boldsymbol{\sigma}} = [\hat{\sigma}_{\mathrm{x}}, \hat{\sigma}_{\mathrm{y}}, \hat{\sigma}_{\mathrm{z}}]$ and the Bloch vector, which is given by [32]

$$\langle \hat{\boldsymbol{\sigma}} \rangle = \mathrm{Tr}(\hat{\rho}_{\mathrm{q}} \hat{\boldsymbol{\sigma}}) = \mathbf{u}. \tag{2.18}$$

2.3.3 Single-qubit gate

Any complex computation performed on a classical or a quantum computer can be broken down to a series of simple gate operations. It is therefore necessary to study the details of a single qubit gate in order to facilitate intricate computations. Typically, a gate operation manipulates the state of the qubit to perform some logical operation. Mathematically, we write the action of a probability conserving gate operation on a qubit as [36]

$$\hat{\chi}(\hat{\rho}_{\mathrm{q}}) = \sum_i \hat{K}_i \hat{\rho}_{\mathrm{q}} \hat{K}_i^\dagger, \tag{2.19}$$

where $\{\hat{K}_i\}$ are the collection of Kraus operators, obeying the completeness relation $\sum_i = \hat{K}_i \hat{K}_i^\dagger = \hat{\mathbb{1}}$. For example, a quantum NOT gate operation on a qubit results in swapping of the basis states and is given by

$$\hat{\chi}_{\mathrm{NOT}}(\hat{\rho}_{\mathrm{q}}) = \hat{\sigma}_{\mathrm{x}} \hat{\rho}_{\mathrm{q}} \hat{\sigma}_{\mathrm{x}}. \tag{2.20}$$

A quantum NOT gate is usually referred to as a Pauli-X gate or simply a X gate operation. The resulting operation is conveniently visualized on the Bloch sphere as a π-rotation of the Bloch vector around the x-axis. Similarly, there are quantum gates such as Pauli-Y and Pauli-Z, which are obtained by an equivalent π-rotation around the y- and z- axes, respectively.

2.3.4 Gate fidelity and error

It is important to establish a measure to quantify the quality of gate operations. A widely used measure is the fidelity F, which is defined as [37, 38]

$$F(\hat{\rho}_{\mathrm{exp}}, \hat{\rho}_{\mathrm{ideal}}) = \mathrm{Tr}(\hat{\rho}_{\mathrm{exp}}, \hat{\rho}_{\mathrm{ideal}}), \tag{2.21}$$

where $\hat{\rho}_{\mathrm{exp}}$ and $\hat{\rho}_{\mathrm{ideal}}$ are the resulting quantum states from experimental and ideal gate operations, respectively. Consequently, the gate fidelity measures an overlap between two quantum states. For a perfect gate operation, the fidelity takes the value of 1, while the worst possible gate operation yields $F = 0$.

An alternative measure of the performance of a gate operation is given by the gate error

$$\varepsilon(\hat{\rho}_{\mathrm{exp}}, \hat{\rho}_{\mathrm{ideal}}) = 1 - F(\hat{\rho}_{\mathrm{exp}}, \hat{\rho}_{\mathrm{ideal}}), \tag{2.22}$$

which is also sometimes referred to as infidelity.

3 THEORETICAL BACKGROUND ON CIRCUIT QUANTUM ELECTRODYNAMICS

The study of the light–matter interaction led to the invention of a laser, a prominent discovery of 21st century. Not long after, an emerging theory of cavity quantum electrodynamics (CQED) pushed the frontier of light–matter interaction to an unparalleled direction. CQED studies the interaction of quantized electromagnetic field with atoms confined in high finesse optical cavities. This opened up a wide range of opportunities to experimentally demonstrate quantum effects like superposition, entanglement of atoms with photons, quantum teleportation, generation of non-classical states of light and many purely quantum-mechanical phenomena [39, 40, 41]. Recently, CQED has spawned numerous fields studying similar interactions. In particular, for quantum computing and information processing related tasks [42, 43]. One such field is circuit quantum electrodynamics (cQED) [44].

In this chapter, we present methods to describe light–matter interaction with superconducting circuits and study the associated CQED-like physics in a different light. We utilize existing circuit elements and use it to describe an atom and an optical cavity. Not surprisingly, one can argue how classical circuit elements could be used to demonstrate quantum phenomena. To tackle this, we make a transition from the classical description of electrical circuits to quantum-mechanical through a quantization procedure discussed in chapter 2. In doing so, we reveal unique quantum behaviour of an electrical circuit and use the associated quantum degrees of freedom to demonstrate quantum information processing related tasks.

We start with the description of a coplanar waveguide (CPW) resonator as a single-mode harmonic LC oscillator, resembling an optical cavity and an anharmonic LC oscillator realized from a non-linear element referred to as the Josephson junction, replacing an atom, which we call a qubit or a two-level system. We present resonator-qubit interaction by borrowing the concepts from CQED, precisely by investigating the spectrum of the Jaynes–Cummings Hamiltonian with a few approximations. Finally, we will describe methods to implement a quantum NOT gate and to minimize the error resulting from the gate operation.

3.1 Microwave resonators

In CQED, an optical cavity stores quantized electromagnetic excitations, i.e., photons of the visible spectrum of electromagnetic radiation. Usually, two highly reflecting mirrors form an optical cavity. In cQED, CPW resonator functions as an optical cavity but stores microwave photons. In this section, we present the quantum-mechanical description of a CPW resonator.

3.1.1 Quantum LC oscillator

In section 2.2, we presented the recipe for the quantization of a harmonic oscillator and we make use of this in the quantum-mechanical description of a simple LC oscillator. The discussion of a LC oscillator is important in order to describe a CPW resonator, which is treated as a sequence of coupled LC oscillators [45], see figure 3.2c.
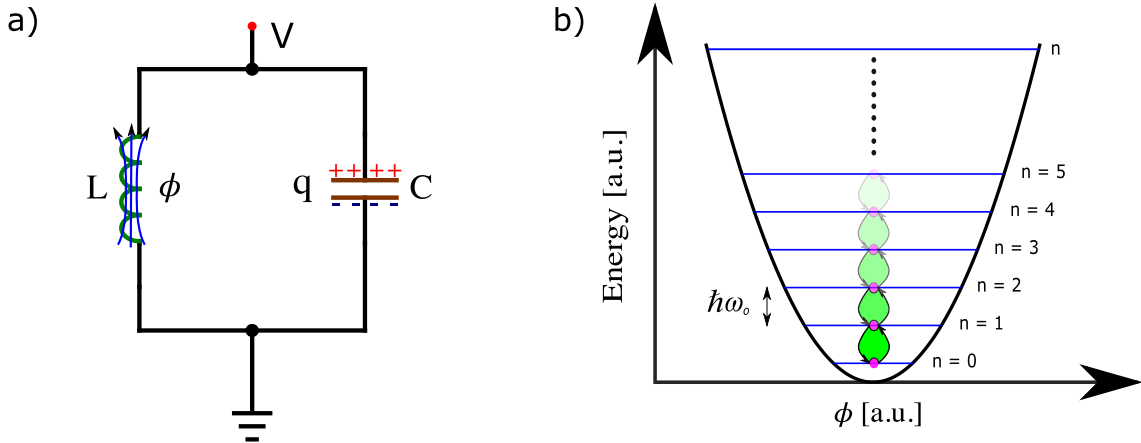
Figure 3.1. *Quantum LC oscillator. **a)** Lumped-element model, Capacitor (capacitance C) and inductor (inductance L) connected in parallel makes up a LC oscillator with resonant frequency $\omega_0 = \frac{1}{\sqrt{LC}}$. The voltage V applied at the node creates a charge $q = CV$ on the capacitor and the current $I = -\frac{\mathrm{d}q}{\mathrm{d}t}$ flowing through the inductor gives rise to a magnetic flux $\phi = LI$. **b)** Equally spaced, non-degenerate discrete eigenenergies of a quantum LC oscillator.*

The charge oscillation in the circuit induces the oscillation of electric and magnetic fields between the plates of the capacitor and inside the inductor, respectively. Both electric and magnetic fields have energy density associated with them, which give rise to the total energy of the LC oscillator as the sum of the capacitive $\frac{q^2}{2C}$ and the inductive $\frac{LI^2}{2}$ energy. Furthermore, we utilize the definition of the flux ϕ and the resonant frequency ω_0 in the inductive energy term to construct the classical Hamiltonian for the LC oscillator

$$H = \frac{q^2}{2C} + \frac{\phi^2}{2}C\omega_0^2. \tag{3.1}$$

We immediately recognize the form of equation (3.1) resembling equation (2.7) describ-

ing a mechanical oscillator, where C represents the mass, q the momentum and ϕ the position. Following the recipe outlined in section 2.2, we attain discrete energy levels of the quantum LC oscillator

$$\hat{H} = \hbar\omega_0\Big(\hat{a}^\dagger\hat{a} + \frac{1}{2}\Big) = \hbar\omega_0\Big(\hat{N} + \frac{1}{2}\Big),\tag{3.2}$$

where as before the commutation relations yield $[\hat{\phi}, \hat{q}] = \mathrm{i}\hbar$ and $[\hat{a}, \hat{a}^\dagger] = 1$. The quantized charge $\hat{q}$ and flux $\hat{\phi}$ operators in terms of the ladder operators are given by

$$\hat{q} = \mathrm{i}\sqrt{\frac{\hbar\omega_0 C}{2}}(\hat{a}^\dagger - \hat{a}), \qquad (3.3) \qquad\qquad \hat{\phi} = \sqrt{\frac{\hbar}{2\omega_0 C}}(\hat{a}^\dagger + \hat{a}), \qquad (3.4)$$

with $Z_0 = \sqrt{\frac{L}{C}}$ as the characteristic impedance of the circuit. This is an example of a zero-mode resonator, since there is only one frequency ω_0 allowed by the oscillator. Similar to a quantized electromagnetic field in an optical cavity, the eigenenergy spectrum of a quantum LC oscillator is equally-spaced by $\hbar\omega_0$ and non-degenerate as shown in figure 3.1b. Thus, we call these discrete excitations of the electromagnetic field in a LC oscillator, microwave photons. However, we will use the terms microwave photons and photons interchangeably.

In addition, we observe that the ground state $|n = 0\rangle$ corresponds to the case where there is no photons in the oscillator. We can inject photons from the environment to the oscillator and therefore, create an excitation in the LC oscillator. Mathematically, this scenario is represented by an operation $\hat{a}^\dagger|0\rangle = |1\rangle$. Similarly, we can remove a photon from the oscillator to the environment through operation $\hat{a}|1\rangle = |0\rangle$, leaving the oscillator at the ground state. The physical realization of injecting and removing photons to and from the oscillator can be different. However, the mathematical description of the process remains unique.

3.1.2 Coplanar waveguide resonator

In order to observe quantum effects in an electrical circuit, certain factors need to be taken into consideration. Coupling of an electrical circuit to the dissipative environment and thermal noise being the most common ones. Thus, we require high-quality LC resonator with a very low photon loss rate and must be operated at sub-millikelvin temperatures. Transmission line resonator realized as CPW structure (see figure 3.2) fulfills both conditions. Furthermore, it can be physically realized with the state-of-the-art microfabrication techniques.

In the treatment of the quantum LC oscillator as a simple LC circuit, we employed the lumped-element model, that is, when the physical dimensions of the circuit elements are much smaller than the wavelength of microwave frequencies. In the case of a CPW, this is

no longer true since the length of the resonator is comparable to used wavelength. Thus, it is required for us to resort to the distributed-element model [45].
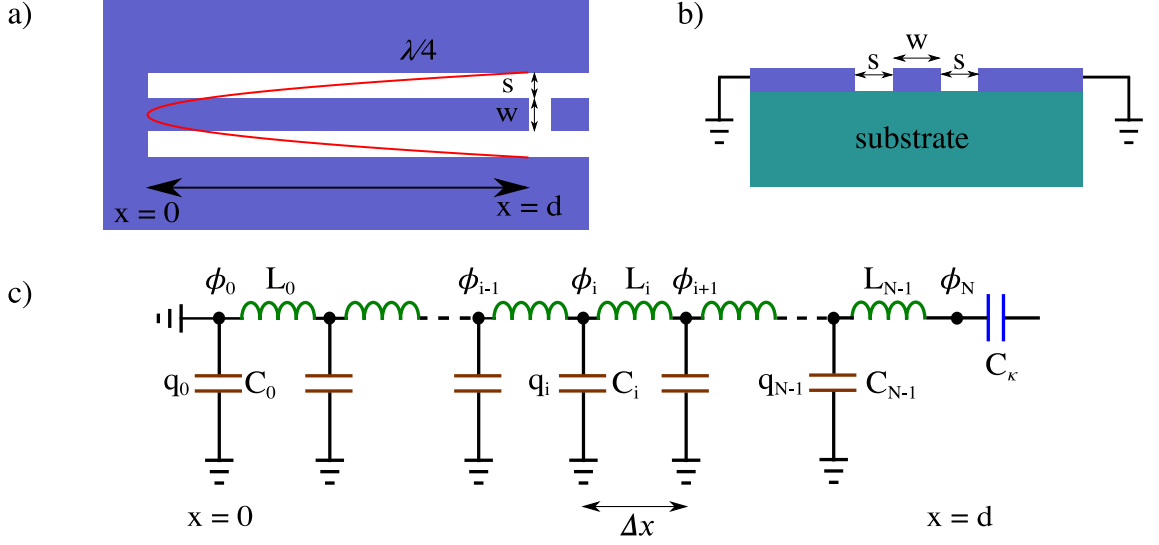
Figure 3.2. *Schematic representation of a two-dimensional CPW resonator. **a)** Top view of a CPW resonator with the center conductor width w, the spacing between the conductor and ground plane s and the length of the resonator d. The CPW forms a $\frac{\lambda}{4}$ resonator realized with one closed end (short-circuit at x = 0) and one open end (open-circuit at x = d). **b)** Cross-section of the waveguide realized as a thin superconducting metal (Niobium) islands on top of a thick dielectric substrate (Si wafer). The adjacent planes are grounded while the center conductor is set to a floating potential. **c)** Equivalent distributed-element model. At x = d, the waveguide is coupled to external feedlines through the capacitor C_κ.*

In the distributed-element model, CPW is divided into a discrete number of lumped-element LC oscillators, see figure 3.2c. CPWs have uniform capacitance c and inductance l per unit length, which are dictated by the geometry of the waveguide, i.e., values of w and s and material parameters [46]. Thus, the capacitances and inductances for each discrete LC oscillators are $C_i = C_r = c\Delta x$ and $L_i = L_r = l\Delta x$, respectively. We observe that at each node i, we have the charge q_i on the capacitor C_i and the flux $\phi_{i+1} - \phi_i$ on the inductor L_i. Putting this all together, we write the classical Hamiltonian of the CPW as

$$H_R = \sum_{i=0}^{N-1} \frac{1}{2C_r} q_i^2 + \frac{1}{2L_r} (\phi_{i+1} - \phi_i)^2. \tag{3.5}$$

To utilize the quantization procedure discussed in section 2.2, we require discrete eigenmodes of CPW in the approximation of the distributed-element method. To this end, we express the Hamiltonian from equation (3.5) in the continuum limit by replacing the charge with a charge density field $\rho(x_i) = \frac{q_i}{\Delta x}$ and the flux with a flux field $\phi(x_i) = \phi_i$. With $\lim_{\Delta x \to 0} \frac{\phi_{i+1} - \phi_i}{\Delta x} = \partial_x \phi_i$ and replacing $\sum_{i=0}^{N-1} \to \int_0^d$, we get the massless Klein–Gordon

quantum field theory [47]

$$H_{\mathrm{R}} = \int_0^d \left[\frac{1}{2c}\rho(x)^2 + \frac{1}{2l}[\partial_x\phi(x)]^2 \right] \mathrm{d}x. \tag{3.6}$$

In general, the voltage $V(x,t)$ is between the center conductor and the ground plane. Thus, the generalized coordinate flux field is a function of both time t and position x, since it is defined as $\phi(x,t) = \int_{-\infty}^t V(x,t')\mathrm{d}t'$. As a result, the charge density field being canonical momentum of the flux field satisfies $\rho(x,t) = c\partial_t\phi(x,t)$. By employing the Hamilton's principle in equation (3.6), we reduce the description of the field theory to just the flux field and recognize that it satisfies the wave-equation

$$\left(\partial_t^2 - v^2\partial_x^2 \right)\phi(x,t) = 0, \tag{3.7}$$

where $v = \frac{1}{\sqrt{lc}}$ is the speed of microwave photons in the CPW. By writing the solution to equation (3.7) as the product of separable spatial and temporal eigenmodes

$$\phi(x,t) = \sum_{k=0}^{\infty} u_k(x)\phi_k(t) \tag{3.8}$$

with temporal eigenmodes obeying $\ddot{\phi}_k = -\omega_k^2\phi_k$, we attain a second-order homogeneous ordinary differential equation for spatial wavefunction

$$\partial_x^2 u_k(x) = -k_k^2 u_k(x), \tag{3.9}$$

where temporal mode frequency ω_k dictates oscillation in time and the spatial mode wavenumber $k_k = \frac{\omega_k}{v}$ - oscillation in space. The solution to equation (3.9) takes the form

$$u_k(x) = U_k\cos(k_kx + \varphi_k), \tag{3.10}$$

where U_k and φ_k are the amplitude and phase corresponding to the spatial eigenmode u_k, respectively. By imposing the boundary condition for $\frac{\lambda}{4}$-resonator, i.e., vanishing voltage at the short-circuit end $\phi(0,t) = 0$ and maximal current at the open end $\left.\frac{\partial\phi(x,t)}{\partial x}\right|_{\mathrm{x=d}} = 0$, we attain

$$k_k = (2k+1)\frac{\pi}{2d}, \tag{3.11}$$

$$\omega_k = vk_k = (2k+1)\frac{\pi}{2\sqrt{L_{\mathrm{r}}C_{\mathrm{r}}}}. \tag{3.12}$$

The amplitude U_k is chosen in a such a way that the spatial mode function is normalized, i.e., it satisfies $\frac{1}{d}\int_0^d u_k(x)u_m(x)dx = \delta_{km}$. With this discrete eigenmode solution, we

express the continuum limit of the Hamiltonian in equation (3.6) as

$$H_{\mathrm{R}} = \sum_{k=0}^{\infty} \frac{q_k^2}{2C_{\mathrm{r}}} + \frac{\phi_k^2}{2} C_{\mathrm{r}} \omega_k^2.$$ (3.13)

We notice that the inductance of the CPW is treated to be mode dependent since $L_k = \frac{1}{\omega_k^2 C_{\mathrm{r}}} = \frac{4L_{\mathrm{r}}}{(2k+1)^2\pi^2}$. Now, the Hamiltonian in equation (3.13) assumes exactly the form required for us to employ the quantization procedure. We promote the conjugate variables (q_k, ϕ_k) to quantum operators $(\hat{q}_k, \hat{\phi}_k)$ with commutation relations $[\hat{q}_k, \hat{\phi}_{k'}] = \mathrm{i}\hbar\delta_{kk'}$ and $[\hat{a}_k, \hat{a}_{k'}^\dagger] = \delta_{kk'}$. The resulting eigenenergy spectrum of equation (3.13) yields

$$\hat{H}_{\mathrm{R}} = \sum_{k=0}^{\infty} \hbar\omega_k \Big(\hat{a}_k^\dagger \hat{a}_k + \frac{1}{2}\Big).$$ (3.14)

The mode dependent quantized charge $\hat{q}_k$ and flux $\hat{\phi}_k$ operators read

$$\hat{q}_k = \mathrm{i}\sqrt{\frac{\hbar\omega_k C_{\mathrm{r}}}{2}}(\hat{a}_k^\dagger - \hat{a}_k) \qquad (3.15) \qquad \hat{\phi}_k = \sqrt{\frac{\hbar}{2\omega_k C_{\mathrm{r}}}}(\hat{a}_k^\dagger + \hat{a}_k).$$ (3.16)

where $Z_k = \sqrt{\frac{L_k}{C_{\mathrm{r}}}}$ is mode-specific characteristic impedance of the CPW. The diagonalized Hamiltonian in equation (3.14) is sometimes referred to as the bath of independent harmonic oscillators. Consequently, CPWs are multi-mode LC resonators. In general, the harmonic frequency modes ω_k can be selectively chosen for excitation and usually it is the fundamental mode, i.e., $k = 0$. Thus, it allows us to replace the sum with just a single term $\hat{H}_{\mathrm{R}} = \hbar\omega_{\mathrm{r}}\Big(\hat{a}^\dagger\hat{a} + \frac{1}{2}\Big)$, where $\omega_0 = \omega_{\mathrm{r}}$ uniquely defines resonator frequency. This is known as single-mode approximation, which we will make use of in rest of the discussion of CPW resonator. It is also relevant that the higher modes $k > 0$ won't get thermally excited due to low temperature.

3.1.3 Coherent states

The Fock states used earlier to describe the quantum LC oscillators do not have any classical counterpart, since even in the presence of photons, the expected value of the electric field between the center conductor and the ground plane is 0. Thus, the Fock states do not represent a classical field with non-zero amplitude. Coherent states provide the best approximation to classical fields, however with the hint of some non-classical behaviour including quantum fluctuations in the coherent states. A coherent state is formed from superposition of the Fock states [35]

$$|\alpha\rangle = \mathrm{e}^{-|\alpha|^2/2} \sum_n \frac{\alpha^n}{\sqrt{n!}} |n\rangle \,.$$ (3.17)

Consequently, they are the eigenstates of the annihilation operator $\hat{a}\,|\alpha\rangle = \alpha\,|\alpha\rangle$, which results in average photon occupation of $\bar{n} = \langle\alpha|\,\hat{n}\,|\alpha\rangle = |\alpha|^2$ in a given coherent state $|\alpha\rangle$. The probability of finding n photons in a coherent state $|\alpha\rangle$ is given by the Poisson's distribution

$$p(n) = \mathrm{e}^{-\bar{n}}\frac{\bar{n}^n}{n!},\tag{3.18}$$

with the standard deviation relative to the photon number given by $\Delta n/\bar{n} = 1/\sqrt{\bar{n}}$. This results in a decrease of quantum fluctuations as the photon number increases, suggesting mapping to a Gaussian distribution as seen in most classical fields. Often, we require a procedure to construct the quantum description from the classical ones. In the case of generating coherent states from classical fields, we do so by applying the displacement operator

$$\hat{D}(\alpha) = \exp(\alpha\hat{a}^\dagger - \alpha^*\hat{a}),\tag{3.19}$$

to the vacuum state and attain the coherent state $|\alpha\rangle = \hat{D}(\alpha)\,|0\rangle$. This operation can be thought as shifting vacuum state by a vector α in the phase space, which essentially trades off uncertainty in quadrature components to produce classical fields. One can play with these uncertainty relations and produce exotic states of the microwave field, namely squeezed states [39].
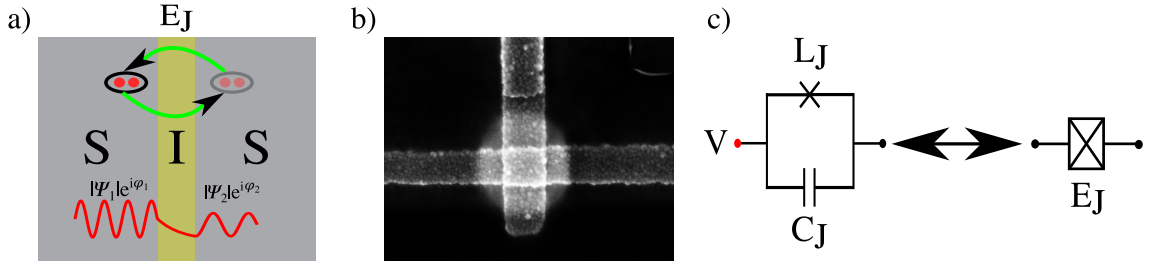
3.2 Superconducting qubit

So far, we have successfully replaced an optical cavity by a CPW in our route to devise CQED-like experiments in the spirit of circuit-QED (cQED). Now, we would like to find similar description for an atom using an electrical circuit. To be more precise, this electrical circuit does not need to exhibit all the properties of an atom but one, i.e., the anharmonic energy spectrum. We wish to use the atom for storing quantum information, which requires any two states to be uniquely defined. Consequently, a LC oscillator fails this requirement as a candidate for an atom since the transition frequency is always the same for all the states. However, if one could introduce non-linearity in the LC oscillator then one can successfully make the spectrum of a LC oscillator anharmonic and therefore, construct a suitable candidate for a qubit. As it happens, this non-linearity can be introduced in a circuit by employing a Josephson junction.

3.2.1 Josephson junction

Josephson junctions are nonlinear superconducting-circuit elements realized as two superconducting electrodes separated by a thin insulting barrier, see figures 3.3a and 3.3b. Both of these superconductors can be effectively described by macroscopic wave functions Ψ_1 and Ψ_2 and associated gauge-invariant phases φ_1 and φ_2 [48, 49]. The absolute value of the wave function contains information about the density of Cooper pairs,

whereas the phase of the wave function essentially encodes all the necessary details we need to study the nonlinear behaviour we are interested in.

Figure 3.3. *Josephson junction.* **a)** *Superconductor-Insulator-Superconductor (SIS) interface forming a typical Josephson junction, facilitating quantum tunneling of Cooper pairs through a thin insulating tunnel barrier (weak link).* **b)** *SEM image of a SIS junction realized from electron-beam lithography in conjunction with the shadow evaporation technique.* **c)** *Circuit representation of a Josephson junction, considered as a LC oscillator with a junction capacitance C_{J} and an inductance L_{J}. The short-hand notation with symbol E_{J} indicates the junction energy.*

Quantum tunneling of Cooper pairs in the absence of an external dc bias (V) leads to a non-zero DC supercurrent flowing through the insulating barrier; this is known as the DC Josephson effect. On the contrary, if a DC bias is applied, it leads to a non-zero AC supercurrent due to the AC Josephson effect. This non-classical behaviour manifests itself into a set of Josephson equations relating the voltage, the current and the phase difference $\varphi = \varphi_2 - \varphi_1$,

$$I_{\mathrm{S}} = I_{\mathrm{C}} \sin(\varphi) \,, \tag{3.20}$$

$$\frac{\mathrm{d}\varphi}{\mathrm{d}t} = \frac{2\pi}{\phi_0} V \,, \tag{3.21}$$

where I_{C} is the critical current sustained by the junction that depends on material parameters, and $\phi_0 = \frac{h}{2e}$ is the flux quantum. The current-phase relationship in equation (3.20) signifies the DC Josephson effect. The AC Josephson effect comes from a more fundamental prediction that the evolution of the phase difference depends on the bias voltage as specified by equation (3.21). In the presence of a constant DC bias voltage, we find $\varphi(t) = \varphi(0) + \frac{2\pi}{\phi_0} Vt$, revealing a very important relationship between the phase difference and the external flux. Furthermore, since the relationship between the flux and the voltage is defined as $\phi(t) = \int_0^t V(t')\mathrm{d}t'$, we get the AC supercurrent $I_{\mathrm{S}}(t) = I_{\mathrm{C}} \sin\left(2\pi \frac{\phi(t)}{\phi_0}\right)$ by setting $\varphi(0) = 0$.

As we have established the relationship between the voltage and the current for a Joseph-

son junction, we find the energy stored in the junction to be

$$E = \int_0^t I_S V(t') \mathrm{d}t' , \tag{3.22a}$$

$$= I_C \int_0^\phi \sin\left(2\pi \frac{\phi'}{\phi_0}\right) \mathrm{d}\phi' , \tag{3.22b}$$

$$= \frac{\phi_0 I_C}{2\pi}\left[1 - \cos\left(2\pi \frac{\phi}{\phi_0}\right)\right] = E_J\left[1 - \cos\left(2\pi \frac{\phi}{\phi_0}\right)\right] , \tag{3.22c}$$

where $E_J = \frac{\phi_0 I_C}{2\pi}$ is the Josephson coupling energy, which is the energy associated with the tunneling rate of Cooper pairs. Additionally, we recognize that the energy stored in the junction depends on the external flux ϕ, similar to the inductive energy in a LC circuit. Thus, we define the Josephson inductance L_J from the relation $\phi = L_J I_S$ and observe

$$V = \frac{\mathrm{d}\phi}{\mathrm{d}t} = L_J \frac{\mathrm{d}I_S}{\mathrm{d}t} \implies L_J(\phi) = \frac{L_C}{\cos\left(2\pi \frac{\phi}{\phi_0}\right)} , \tag{3.23}$$

where $L_C = \frac{\phi_0}{2\pi I_C}$ is the Josephson inductance at zero flux. We acknowledge that L_J is a nonlinear function of the external flux ϕ, which is exactly what we hoped to achieve. Josephson junction also has a capacitance C_J, since the junction resembles a typical capacitor with two superconducting metal islands separated by an insulating barrier. Consequently, a Josephson junction can be regarded as a nonlinear LC oscillator, see figure 3.3c, with the Hamiltonian

$$H_{JJ} = \frac{q^2}{2C_J} + E_J\left[1 - \cos\left(2\pi \frac{\phi}{\phi_0}\right)\right] . \tag{3.24}$$

3.2.2 Charge qubit

Equipped with the Josephson junction as a non-linear LC oscillator, we begin our exposition of the first of a kind superconducting qubit, a charge qubit [18]. A charge qubit can be physically realized in the form of Cooper pair box (CPB), that is, a Josephson junction connected to a DC voltage source through a gate capacitor C_G as depicted in figure 3.4a.

Due to the unequally spaced energy spectrum of a Josephson junction (fig. 3.4b), the qubit space can be formed by limiting the eigenmodes to the ground state $|g\rangle$ and the excited state $|e\rangle$. The truncation of the higher modes can be done by selectively driving transition frequency ω_{ge}. In a charge qubit, this is done by applying a bias voltage to the junction through the gate capacitor. To see this, we express the Hamiltonian of a CPB in the so-called number-phase representation [18, 50] by defining the number operator as
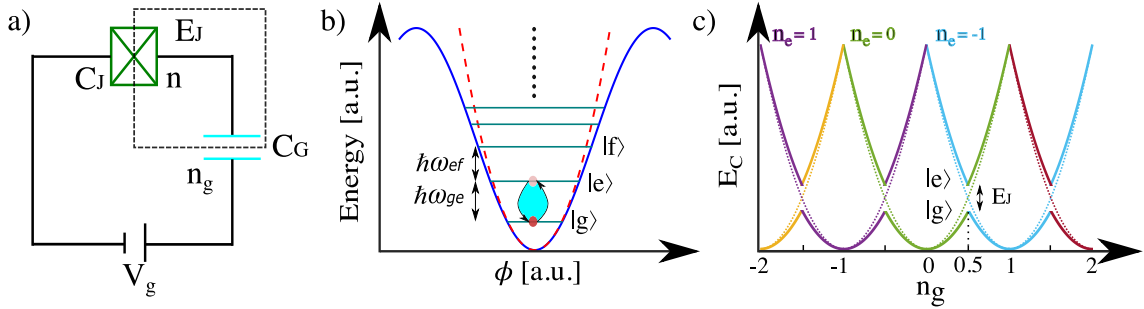
Figure 3.4. *Cooper pair box.* **a)** *Lumped-circuit model of a charge qubit. A Josephson junction connected to an external voltage source through gate capacitor C_{G}.* **b)** *Eigenenergy spectrum of a Josephson junction with an unequal transition frequency of the adjacent states, labelled $|\mathrm{g}\rangle, |\mathrm{e}\rangle, |\mathrm{f}\rangle, ...$ to make a distinction from the number states of a harmonic LC oscillator.* **c)** *Energy spectrum of Cooper-pair box.*

$\hat{q}|n\rangle = -2en|n\rangle$, yielding

$$H_{\mathrm{CPB}} = 4E_{\mathrm{C}}(n - n_{\mathrm{g}})^2 + E_{\mathrm{J}}\left[1 - \cos\left(2\pi\frac{\phi}{\phi_0}\right)\right], \tag{3.25}$$

where $E_{\mathrm{C}} = \frac{e^2}{2C_\Sigma}$ is the charging energy (energy required to put an electron on the island) with the total capacitance $C_\Sigma = C_{\mathrm{J}} + C_{\mathrm{G}}$, n represents the number of Cooper pairs on the island and $n_{\mathrm{g}} = \frac{C_{\mathrm{G}}V_g}{2e}$ is the gate charge used to control the state of the charge qubit. Consequently, we yield the same commutation relationship $[\hat{n}, \hat{\phi}] = \mathrm{i}\hbar$ as in the charge–phase representation.

The energy spectrum of equation (3.25) is computed by solving the Schrödinger equation $\hat{H}_{\mathrm{CPB}}|\phi\rangle = E_k|\phi\rangle$ in phase basis and is shown in figure 3.4c. In case $E_{\mathrm{J}} = 0$, the spectrum consists of a bunch of parabolas corresponding to the number of Cooper pairs on the junction as a function of the gate charge n_{g} (dashed lines in figure 3.4c). For $E_{\mathrm{J}} \ll E_{\mathrm{C}}$, the charge degeneracy at odd multiples of $n_{\mathrm{g}} = \frac{1}{2}$ splits up and thus yields avoided crossings. By confining the gate charge in the range $0 < n_{\mathrm{g}} < 1$, we effectively create a two level system marked with $|\mathrm{g}\rangle$ and $|\mathrm{e}\rangle$ as the ground and the excited state, respectively, see figure 3.4c.

3.2.3 Transmon qubit

Charge qubit introduces an excellent anharmonicity to the energy levels. However, the charge dispersion, i.e., the dependence of the energy on the gate charge is significant as well. This leads to a very small dephasing time, which renders a charge qubit less useful in quantum information processing related tasks. This can be circumvented by increasing the Josephson coupling energy such that $40 < \frac{E_{\mathrm{J}}}{E_{\mathrm{C}}} < 100$. In doing so, we increase the fluctuation of the number of Cooper pairs on the junction and thus make the qubit less susceptible to charge noise as indicated by flat energy bands (fig. 3.5c). Practically, this

is done by adding a large capacitor in parallel with the junction as shown in figure 3.5a. Such type of qubits are called transmons [25].
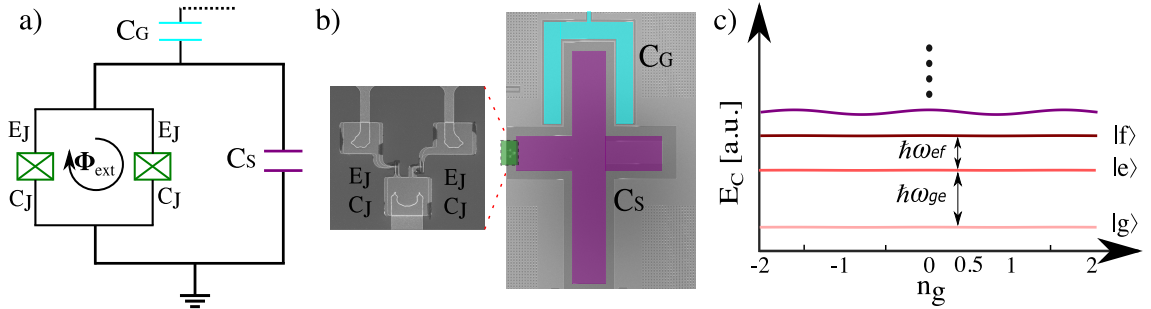
Figure 3.5. *Transmon qubit. **a)** Lumped-element model of a transmon qubit. Two Josephson junctions connected in parallel forming a DC SQUID. The DC SQUID is connected in parallel with a large shunting capacitance C_{S}. This parallel combination of a DC SQUID and a shunt capacitance is coupled to a CPW resonator through the gate capacitance C_{G}. **b)** SEM image of a physically realized transmon qubit, where the qubit island (purple cross) represents the shunt capacitance with a SQUID fabricated on the left arm. The qubit island is coupled to the CPW resonator through a coupler (light-blue horseshoe) island. **c)** Energy spectrum of a transmon, where the Bloch bands are flat due to increased capacitance (decreased charging energy).*

Additionally, a single Josephson junction is replaced by a parallel combination of two Josephson junctions forming direct current superconducting quantum interference device (DC SQUID) [48], see figure 3.5a. The parallel junctions form a loop, where incoming supercurrent splits at the input port and interferes at the exit port. The flow of supercurrent and resulting intereference depends on the external flux ϕ_{ext} applied to the junction consequently, making the Josephson coupling energy tunable as a function of external flux [25]

$$E_{\mathrm{J}}(\phi_{\mathrm{ext}}) = E_{\mathrm{J}\Sigma} \cos\left(\frac{\pi\phi_{\mathrm{ext}}}{\phi_0}\right)\sqrt{1 + d^2 \tan^2\left(\frac{\pi\phi_{\mathrm{ext}}}{\phi_0}\right)}, \tag{3.26}$$

where $E_{\mathrm{J}\Sigma}$ is the sum of the Josephson coupling energy of both junctions and $d = \frac{\Delta E_{\mathrm{J}}}{E_{\mathrm{J}\Sigma}}$ with ΔE_{J} being the difference in the Josephson coupling energy of both junctions. For the maximum range of flux tunability, it is preferred to make both junctions symmetric such that $E_{\mathrm{J}\Sigma} = 2E_{\mathrm{J}}$ and $d = 0$, resulting in $E_{\mathrm{J}}(\phi_{\mathrm{ext}}) = E_{\mathrm{J}\Sigma} \cos\left(\frac{\pi\phi_{\mathrm{ext}}}{\Phi_0}\right)$. In practice, there is always some asymmetricity introduced when fabricating the junction. With these additions to the Hamiltonian of a CPB, we express the Hamiltonian of the transmon as

$$H_{\mathrm{Q}} = 4E_{\mathrm{C}}(n - n_{\mathrm{g}})^2 + E_{\mathrm{J}}\left[1 - \cos\left(2\pi\frac{\phi}{\phi_0}\right)\right], \tag{3.27}$$

where the sum capacitance $C_{\Sigma} = 2C_{\mathrm{J}} + C_{\mathrm{G}} + C_{\mathrm{S}}$ in charging energy E_{C} now includes contributions from a large shunting capacitor C_{S} and capacitance from two Josephson junctions, and the Josephson coupling energy $E_{\mathrm{J}} = E_{\mathrm{J}}(\phi_{\mathrm{ext}})$ is thus flux-dependent. Having the classical Hamiltonian ready, we move on to the quantization procedure. How-

ever to do this, we make few observations regarding the cosine potential of the Josephson junction. The ground $|g\rangle$ and excited $|e\rangle$ states are confined deep in the lower energy levels compared to the height (E_J) of the potential well. Additionally, due to flat lowest energy levels, we set $n_g = 0$ since, essentially there is no charge dispersion present at these levels. With these observations and $\delta = 2\pi\frac{\phi}{\phi_0}$, we Taylor expand $\cos\delta = 1 - \frac{\delta^2}{2} + \frac{\delta^4}{24} - \mathcal{O}(\delta^6)$ and rewrite the Hamiltonian from equation (3.27) as

$$H_Q = \frac{n^2}{2C'} + \frac{\delta^2}{2L'} - E_J\frac{\delta^4}{24} + \mathcal{O}(\delta^6),\tag{3.28}$$

where $C' = \frac{1}{8E_C}$ and $L' = \frac{1}{E_J}$. The first two terms of the equation (3.28) take the similar form as a harmonic oscillator. Thus, by defining the Josephson plasma frequency $E_p = \hbar\omega_p = \frac{1}{\sqrt{L'C'}} = \sqrt{8E_J E_C}$, we write

$$H_Q = \frac{n^2}{2C'} + \frac{\delta^2}{2}C'E_p^2 - E_J\frac{\delta^4}{24} + \mathcal{O}(\delta^6).\tag{3.29}$$

By limiting the equation (3.29) to the first two terms, we observe that the resulting equation resembles quantum harmonic oscillator. With the recipe outlined in section 2.2, we quantize equation (3.29) by promoting conjugate variables (n, δ) to quantum operators, obeying the commutation relationship $[\hat{n}, \hat{\delta}] = i$. This yields

$$\hat{n} = \left(\frac{E_J}{8E_C}\right)^{\frac{1}{4}}\frac{i}{\sqrt{2}}(\hat{b}^\dagger - \hat{b})\qquad(3.30)\qquad\hat{\delta} = \left(\frac{8E_C}{E_J}\right)^{\frac{1}{4}}\frac{1}{\sqrt{2}}(\hat{b}^\dagger + \hat{b}),\qquad(3.31)$$

where creation and annihilation operators satisfy usual commutation relation $[\hat{b}, \hat{b}^\dagger] = 1$. Plugging equations (3.30) and (3.31) into the Hamiltonian in equation (3.29) and disregarding higher order terms, we get

$$\hat{H}_Q = \hbar\omega_p(\hat{b}^\dagger\hat{b} + \frac{1}{2}) - \frac{E_C}{12}(\hat{b}^\dagger + \hat{b})^4.\tag{3.32}$$

Under the rotating wave approximation (RWA), i.e, only taking the terms that have equal number of $\hat{b}^\dagger$ and $\hat{b}$ in $(\hat{b}^\dagger + \hat{b})^4$, we attain

$$\hat{H}_Q = \hbar\omega_{ge}\hat{b}^\dagger\hat{b} + \frac{1}{2}\hbar\omega_p - \frac{E_C}{2}\hat{b}^\dagger\hat{b}^\dagger\hat{b}\hat{b},\tag{3.33}$$

where $\omega_q = \omega_{ge} = (\sqrt{8E_J E_C} - E_C)/\hbar$ is the transition frequency from $|g\rangle$ to $|e\rangle$, commonly referred to as qubit frequency. The RWA approximation is valid because when the frame is rotating at $\omega_q \gg E_C/\hbar$, terms that have unequal amount of $\hat{b}^\dagger$ and $\hat{b}$ will average out if they oscillate at higher frequencies [51].

We make two observations here: first, the qubit frequency is a result of a correction to the Josephson plasma frequency by E_C, this frequency shift is known as *Lamb shift*, and second, the third term in equation (3.33) is referred to as *Kerr nonlinearity*, which results

in a shift of $E_{\mathrm{C}}/\hbar$ in the transition frequency between adjacent states $|k\rangle$ and $|k+1\rangle$. For example, transition frequency between $|e\rangle$ to $|f\rangle$ is given by $\omega_{\mathrm{ef}} = \omega_{\mathrm{ge}} - E_{\mathrm{C}}/\hbar$. Since the Josephson coupling energy is flux-tunable, the qubit frequency $\omega_{\mathrm{q}}(\phi_{\mathrm{ext}}) = (\sqrt{8E_{\mathrm{J}}(\phi_{\mathrm{ext}})E_{\mathrm{C}}} - E_{\mathrm{C}})/\hbar$ can be tuned to the desired value by changing external flux. This will turn out to be a very important property in demonstrating quantum gate operations.

3.3 Transmon–resonator interaction

Having replaced the role of an optical cavity and an atom by a CPW and a transmon qubit, respectively, we move forward to introduce the coupled interaction of a resonator with an artificial atom. Essentially, we are interested in reproducing the results of quantized light-matter interaction, first demonstrated in CQED, with superconducting-circuits, while using the results in a different light to develop unique techniques for implementing quantum information processing related tasks.

3.3.1 Coupling between the transmon and the resonator

Drawing parallelism from an atom coupled to an optical cavity, we describe coupling of a transmon to the waveguide resonator in a similar manner as shown in figures 3.6a and 3.6b.
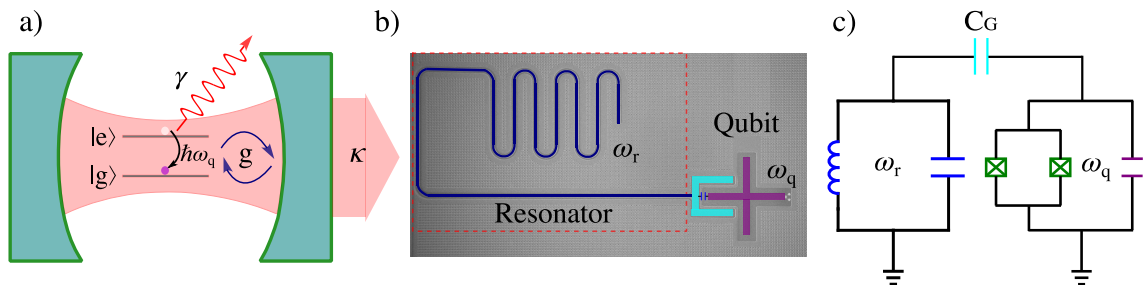
Figure 3.6. *Light–matter interaction.* ***a)*** *A schematic illustration of an atom coupled to an optical cavity. The atom is effectively modelled as a two-level system with transition frequency ω_{q} between states $|\mathrm{g}\rangle$ and $|\mathrm{e}\rangle$. The coherent coupling between the optical cavity and the atom is quantified by the vacuum Rabi coupling g. The incoherent coupling of an atom to the outside environment is dictated by spontaneous emission rate γ and transmission loss rate κ.* ***b)*** *SEM image of a transmon coupled to a resonator, conveying similar coupling scheme as in (**a**).* ***c)*** *Lumped-element model of a coupled transmon–resonator system.*

The coupling of an atom to a cavity is influenced by dipole interaction [39] in CQED, whose details are encapsulated in the interaction Hamiltonian $\hat{H}_{\mathrm{int}} = -\hat{d} \cdot \hat{E}(t)$. In cQED, the interaction arises from capacitive coupling of a transmon to a resonator, facilitated by horseshoe-like coupler as depicted in figure 3.6b. The other factor contributing to this interaction is due to a purely quantum-mechanical effect known as zero-point voltage

fluctuations [35]. In the absence of a microwave photon in the transmon or the resonator, i.e., in a vacuum state $n = 0$, there are non-zero voltage fluctuations induced at the nodes. To observe this, we first recognize the voltage operator is dictated by

$$\hat{V}_{\rm Q} = -\frac{2e}{C_\Sigma}\hat{n} = -\frac{2e}{C_\Sigma}\left(\frac{E_{\rm J}}{8E_{\rm C}}\right)^{\frac{1}{4}}\frac{\rm i}{\sqrt{2}}(\hat{b}^\dagger - \hat{b})\,, \tag{3.34}$$

$$\hat{V}_{\rm R} = \frac{\hat{q}}{C_{\rm r}} = \frac{\rm i}{C_{\rm r}}\sqrt{\frac{\hbar\omega_{\rm r}C_{\rm r}}{2}}(\hat{a}^\dagger - \hat{a})\,, \tag{3.35}$$

where $\hat{n}$ and $\hat{q}$ are given by equations (3.30) and (3.15), respectively. Utilizing this, we obtain

$$V_{\rm rms}^{\rm q,0} = \sqrt{\langle 0|\,\hat{V}_{\rm Q}^2\,|0\rangle - \langle 0|\,\hat{V}_{\rm Q}\,|0\rangle^2} = \sqrt{\langle 0|\,\hat{V}_{\rm Q}^2\,|0\rangle} = \frac{\sqrt{2}e}{C_\Sigma}\left(\frac{E_{\rm J}}{8E_{\rm C}}\right)^{\frac{1}{4}}\,, \tag{3.36}$$

$$V_{\rm rms}^{\rm r,0} = \sqrt{\langle 0|\,\hat{V}_{\rm R}^2\,|0\rangle - \langle 0|\,\hat{V}_{\rm R}\,|0\rangle^2} = \sqrt{\langle 0|\,\hat{V}_{\rm R}^2\,|0\rangle} = \sqrt{\frac{\hbar\omega_{\rm r}}{2C_{\rm r}}}\,. \tag{3.37}$$

where $V_{\rm rms}^{\rm q,0}$ and $V_{\rm rms}^{\rm r,0}$ are the zero-point voltage fluctuations induced at the transmon and resonator nodes, respectively. Voltage fluctuations in the resonator give rise to strong electric field fluctuations between the center conductor and the ground plane, establishing close analogy with the dipole interaction observed in CQED. Combining all this together, the coupling of a transmon to a resonator is described by the interaction Hamiltonian [52]

$$\hat{H}_{\rm I} = -C_{\rm G}\hat{V}_{\rm Q} \otimes \hat{V}_{\rm R}\,, \tag{3.38}$$

$$= -C_{\rm G}V_{\rm rms}^{\rm q,0}V_{\rm rms}^{\rm r,0}(\hat{b}^\dagger - \hat{b}) \otimes (\hat{a}^\dagger - \hat{a})\,, \tag{3.39}$$

$$= -\hbar g(\hat{b}^\dagger - \hat{b}) \otimes (\hat{a}^\dagger - \hat{a})\,, \tag{3.40}$$

where voltage fluctuations and the gate capacitance are absorbed in a single term $g = C_{\rm G}V_{\rm rms}^{\rm q,0}V_{\rm rms}^{\rm r,0}/\hbar$ called the vacuum Rabi coupling constant.

3.3.2 Jaynes–Cummings model

The dynamics of a transmon coupled to a resonator can be effectively studied by constructing the Hamiltonian of transmon, resonator and their coupled interaction. Thus, we obtain

$$\hat{H} = \hat{H}_{\rm R} + \hat{H}_{\rm Q} + \hat{H}_{\rm int}\,, \tag{3.41}$$

$$= \hbar\omega_{\rm r}\hat{a}^\dagger\hat{a} + \hbar\omega_{\rm q}\hat{b}^\dagger\hat{b} - \frac{E_{\rm C}}{2}\hat{b}^\dagger\hat{b}^\dagger\hat{b}\hat{b} - \hbar g(\hat{b}^\dagger - \hat{b}) \otimes (\hat{a}^\dagger - \hat{a})\,, \tag{3.42}$$

where we have disregarded the zero-point energy by a suitable choice of energy reference. By expressing the transmon and the interaction Hamiltonian in the qubit eigenbasis with completeness relation $\sum_j |j\rangle\langle j| = \mathbb{1}_{\rm Q}$ and invoking RWA since the prefactor satis-

fies the relation $g \ll \omega_{\rm r}, \omega_{\rm q}$, we obtain [25]

$$\hat{H}_{\rm g-JC} \approx \hbar\omega_{\rm r}\hat{a}^\dagger\hat{a} + \hbar\sum_j \omega_j \left|j\right\rangle\left\langle j\right| + \hbar\sum_j g_{j,j+1}\left(\left|j\right\rangle\left\langle j+1\right| \otimes \hat{a}^\dagger + \left|j+1\right\rangle\left\langle j\right| \otimes \hat{a}\right),$$

(3.43)

where $g_{j,j+1} = g\sqrt{j+1}$ is the Rabi coupling constant associated with eigenstates $\left|j\right\rangle$ and $\left|j+1\right\rangle$. Equation (3.43) is a generalized Jaynes–Cummings (JC) Hamiltonian that describes a multi-level transmon qubit interacting with single-mode resonator. For a two-level approximation, we truncate higher levels and attain the standard JC Hamiltonian [53]

$$\hat{H}_{\rm JC} = \hbar\omega_{\rm r}\hat{a}^\dagger\hat{a} + \frac{\hbar\omega_{\rm q}}{2}\hat{\sigma}_z + \hbar g(\hat{\sigma}_- \otimes \hat{a}^\dagger + \hat{\sigma}_+ \otimes \hat{a}),$$

(3.44)

where we have used the fact that $g_{01} = g\sqrt{0+1} = g$. The interaction Hamiltonian in the standard JC model leads us to a very important observation that the term $\hat{\sigma}_- \otimes \hat{a}^\dagger$ signifies emission of a photon to the resonator due to the relaxation of the transmon from $\left|{\rm e}\right\rangle$ to $\left|{\rm g}\right\rangle$ state, whereas the term $\hat{\sigma}_+ \otimes \hat{a}$ indicates the absorption of a photon from the resonator to create an excitation from $\left|{\rm g}\right\rangle$ to $\left|{\rm e}\right\rangle$ in the transmon.
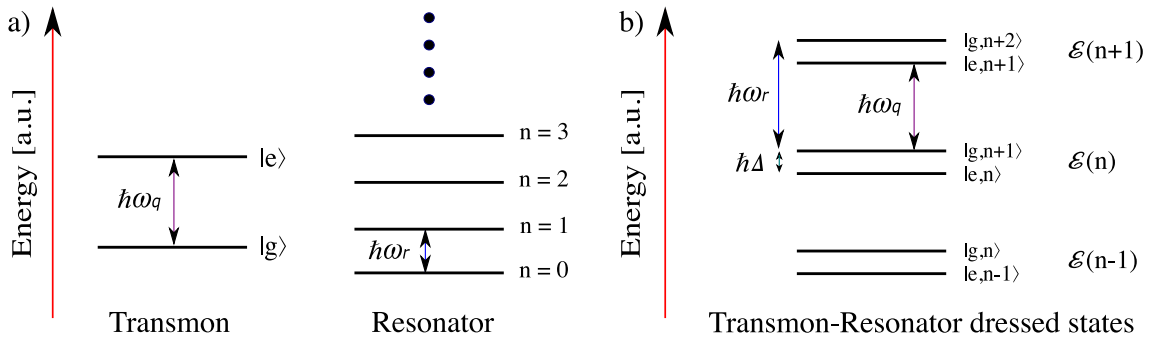
Figure 3.7. *Dressed states.* **a)** *Individual eigenstates of an uncoupled Hamiltonian. The eigenstates of a transmon are truncated to the ground and the excited states with transition frequency w_q (left). Eigenstates of a single-mode resonator with transition frequency $\omega_{\rm r}$ (right).* **b)** *Eigenstates (dressed) of the coupled Hamiltonian, where the eigenstates are grouped into natural manifolds $\mathcal{E}(n)$ with equal energy spacing given by $\hbar\omega_{\rm q}$ and $\hbar\omega_{\rm r}$.*

The combined state of an uncoupled Hamiltonian $\hat{H}_{\rm Q} + \hat{H}_{\rm R}$ is described by the product state $\left|j,n\right\rangle = \left|j\right\rangle \otimes \left|n\right\rangle$ of the transmon and the resonator, where the transmon can either be in state $\left|{\rm g}\right\rangle$ or $\left|{\rm e}\right\rangle$ and the resonator can be in any of the number state as depicted in figure 3.7a. However when the transmon–resonator interaction takes place, the eigenstates (dressed states) of the coupled Hamiltonian $\hat{H}_{\rm Q} + \hat{H}_{\rm R} + \hat{H}_{\rm int}$ are formed out of the superposition states of manifolds $\mathcal{E}(n)$ grouped in the energy space as shown in figure 3.7b. The eigenstate corresponding to a manifold $\mathcal{E}(n)$ is a superposition of product states $\left|e,n\right\rangle$ and $\left|g,n+1\right\rangle$, which has an energy difference of $\hbar(\omega_{\rm r} - \omega_{\rm q}) = \hbar\Delta$ between the product states.

3.3.3 Temporal evolution

The standard JC Hamiltonian in equation (3.44) does not contain any incoherent coupling to the environment, thus the Hamiltonian describing the system can be considered closed. Temporal dynamics of such system are dictated by unitary evolution. As such, the dynamics of the JC model can be solved in numerous ways [35, 53]: by constructing time-dependent Schrödinger equation for the product state of the transmon and the resonator, by first finding the dressed states as eigenstates of the coupled Hamiltonian, and, finally, by employing state-operator approach as outlined in section 2.1. We utilize the state-operator scheme to solve the dynamics of the JC model for the resonant case, i.e, detuning $\Delta = \omega_{\mathrm{r}} - \omega_{\mathrm{q}} = 0$. To this end, we write

$$\hat{H} = \hat{H}_0 + \hat{H}_{\mathrm{int}} \tag{3.45}$$

$$= \hbar\omega(\hat{a}^\dagger\hat{a} + \frac{\hat{\sigma}_z}{2}) + \hbar g(\hat{\sigma}_- \otimes \hat{a}^\dagger + \hat{\sigma}_+ \otimes \hat{a}), \tag{3.46}$$

where $\omega = \omega_{\mathrm{r}} = \omega_{\mathrm{q}}$. Writing the JC Hamiltonian in the form of equation (3.45) allows us to think of the interaction term $\hat{H}_{\mathrm{int}}^I$ as a perturbation to the uncoupled hamiltonian $\hat{H}_0$. Additionally, this form hints us at solving the dynamics in the interaction picture, where the evolution of the observables are described by $\hat{H}_0$ and evolution of the states are determined by $\hat{H}_{\mathrm{int}}^I = e^{i\hat{H}_0/\hbar}\hat{H}_{\mathrm{int}}e^{-i\hat{H}_0/\hbar}$ [31]. In doing so, we attain the interaction Hamiltonian in the interaction picture

$$\hat{H}_{\mathrm{int}}^I = \hbar g(\hat{\sigma}_- \otimes \hat{a}^\dagger + \hat{\sigma}_+ \otimes \hat{a}). \tag{3.47}$$

We define the density operator $\hat{\rho} = \hat{\rho}_{\mathrm{Q}} \otimes \hat{\rho}_{\mathrm{R}}$ of transmon–resonator system with $\hat{\rho}_{\mathrm{Q}}$ and $\hat{\rho}_{\mathrm{R}}$ describing the density operators of the transmon and the resontor, respectively. The evolution of the system in the interaction picture is given by the Liouville von–Neumann equation (2.3)

$$i\hbar\frac{\mathrm{d}\hat{\rho}(t)}{\mathrm{d}t} = [\hat{H}_{\mathrm{int}}^I, \hat{\rho}(t)], \tag{3.48}$$

whose solution takes the form of equation (2.4) with unitary operator

$$\hat{\mathcal{U}}(t) = \exp\left[-igt(\hat{\sigma}_- \otimes \hat{a}^\dagger + \hat{\sigma}_+ \otimes \hat{a})\right]. \tag{3.49}$$

With operators $\hat{\sigma}_+ = \begin{pmatrix} 0 & 1 \\ 0 & 0 \end{pmatrix}$ and $\hat{\sigma}_- = \begin{pmatrix} 0 & 0 \\ 1 & 0 \end{pmatrix}$ in a matrix form, the unitary operator can be expanded in the qubit space as [35]

$$\hat{\mathcal{U}(t)} = \begin{pmatrix} \cos\left(gt\sqrt{\hat{a}\hat{a}^\dagger}\right) & -i\hat{a}\frac{\sin\left(gt\sqrt{\hat{a}^\dagger\hat{a}}\right)}{\sqrt{\hat{a}^\dagger\hat{a}}} \\ -i\hat{a}^\dagger\frac{\sin\left(gt\sqrt{\hat{a}\hat{a}^\dagger}\right)}{\sqrt{\hat{a}\hat{a}^\dagger}} & \cos\left(gt\sqrt{\hat{a}^\dagger\hat{a}}\right) \end{pmatrix}. \tag{3.50}$$

For a given initial state $\hat{\rho}(0) = \hat{\rho}_{\mathrm{Q}}(0) \otimes \hat{\rho}_{\mathrm{R}}(0)$, the temporal evolution takes the form

$$\hat{\rho}(t) = \hat{\mathcal{U}}(t) \big[\hat{\rho}_{\mathrm{Q}}(0) \otimes \hat{\rho}_{\mathrm{R}}(0) \big] \hat{\mathcal{U}}^{\dagger}(t). \tag{3.51}$$

Note that the evolution described by equation (3.51) is unitary only for the system as a whole, and does not prescribe any such unitary evolution for the transmon or the resonator density operators. Despite initially being in the pure state, the transmon and the resonator may be described by entangled states during the evolution. Thus, it is required for us to resort to the reduced density operator description of the transmon and the resonator by taking partial traces $\hat{\rho}_{\mathrm{Q}}(t) = \mathrm{Tr}_{\mathrm{R}}\hat{\rho}(t)$ and $\hat{\rho}_{\mathrm{R}}(t) = \mathrm{Tr}_{\mathrm{Q}}\hat{\rho}(t)$, respectively, as described in section 2.1.

3.3.4 Rabi oscillation: Recipe for NOT gate

One of the important results stemming from the temporal evolution of eq. (3.51) is the so-called Rabi oscillation [35], that is the oscillatory nature of the population inversion of qubit states. This becomes evident by considering the initial state of the resonator to be $\hat{\rho}_{\mathrm{R}}(0) = \sum_{n=0}^{\infty} p(n) |n\rangle \langle n|$ and the transmon to be in the ground state, i.e., $\hat{\rho}_{\mathrm{Q}}(0) = |\mathrm{g}\rangle \langle \mathrm{g}|$.
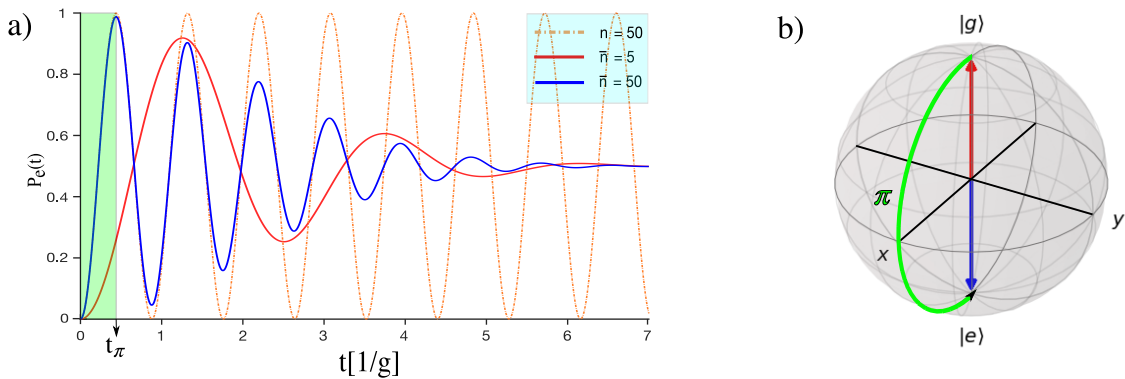
Figure 3.8. *Rabi oscillations.* ***a)*** *Probability of the excited state population seen as a Rabi oscillation, resulting from the temporal evolution under a resonant JC Hamiltonian. A perfect periodic oscillation (orange dashed line) comes about when the initial state of the resonator is described by a Fock state $n = 50$. Damped Rabi oscillations occur when the resonator is in a coherent state with average photon number $\bar{n} = 5$ (red) and $\bar{n} = 50$ (blue).* ***b)*** *A visualization of a NOT gate operation on a Bloch sphere. The qubit is initially in the ground state $|\mathrm{g}\rangle$ (red arrow) makes π-rotation around y-axis to end up at the excited state $|\mathrm{e}\rangle$.*

With these initial conditions and unitary operator from equation (3.50), we obtain [35]

$$P_{\mathrm{e}}(t) = \sum_{n=0}^{\infty} p(n) \sin^2(gt\sqrt{n+1}) \,, \tag{3.52}$$

$$P_{\mathrm{g}}(t) = \sum_{n=0}^{\infty} p(n) \cos^2(gt\sqrt{n+1}) \,, \tag{3.53}$$

where $p(n)$ is the probability density of photon states in the resonator, P_{e} and P_{g} are the occupation probability of the excited and the ground state of the transmon, respectively. For a non-classical Fock state, the probability density $p(n) = \delta(n)$ is essentially a delta function, yielding excited state population probability $P_{\mathrm{e}}(t) = \sin^2(gt\sqrt{n+1})$. We observe that even in the absence of a photon in the resonator, the excited state would evolve in time. This purely quantum-mechanical phenomenon is called the vacuum-field Rabi oscillation. In addition, we observe that the frequency of the Rabi oscillation $\Omega(n) = 2g\sqrt{n+1}$ depends on the number of photons present in the resonator. An example evolution of the excited state probability with photon number $n = 50$ results in perfect periodic oscillation between $|\mathrm{e}\rangle$ and $|\mathrm{g}\rangle$ similar to the semi-classical model [35], see figure 3.8a.

As discussed in section 3.1.3, a number state does not have any classical counterpart and thus, it is difficult to generate number states in the lab. Coherent states, on the other hand, are the most classical of all the other quantum states and approximately describe the interaction in the classical limit. Coherent states with the probability density from equation (3.18) substituted in equation (3.52) result in an excited state probability $P_{\mathrm{e}}(t) = e^{-\bar{n}} \sum_{n=0}^{\infty} \frac{\bar{n}^n}{n!} \sin^2(gt\sqrt{n+1})$. Rabi oscillations with average photon number $\bar{n} = 5 \,\&\, 50$ are depicted in figure 3.8a. Surprisingly, we observe damped oscillation in the coherent state model and recognize that we recover semi-classical Rabi oscillation in the limit $\bar{n} \to \infty$.

The most fruitful outcome from the discussion of Rabi oscillations is the recipe it provides us to implement a quantum version of the NOT gate, i.e, the swapping of the states $|\mathrm{g}\rangle \leftrightarrow |\mathrm{e}\rangle$. We recognize that the population inversion with coherent states takes place at

$$t_{\pi} = \frac{\pi}{2g\sqrt{\bar{n}}}, \tag{3.54}$$

where t_{π} is naturally referred to as a π-pulse length, given the π-phase shift during the population inversion. Thus, a transmon prepared in the ground state is led to interact with a resonator occupied with an average photon number $\bar{n}$ for the duration of t_{π}. This results in the transmon occupying excited state and hence, demonstrating a NOT gate operation. The whole operation can be easily visualized as π-rotation on the Bloch sphere as illustrated in figure 3.8b.

It is customary to quantify the error resulting from a gate operation as discussed in section 2.3.4. This is facilitated by first estimating the fidelity F of the gate operation. In general, fidelity depends on the initial states of the transmon and the resonator and is given by

$$F(\hat{\rho}_{\rm Q}, \hat{\rho}_{\rm R}) = {\rm Tr}\Big[\hat{\chi}_{\rm U}(t_\pi)\hat{\chi}_{\rm K}\Big], \tag{3.55}$$

where $\hat{\chi}_{\rm U}(t_\pi) = {\rm Tr}_{\rm R}[\mathcal{U}(\hat{t}_\pi)(\hat{\rho}_{\rm Q}(0) \otimes \hat{\rho}_{\rm R}(0))\mathcal{U}^\dagger(\hat{t}_\pi)]$ is the state resulting from implementation of the NOT gate described earlier and $\hat{\chi}_{\rm K} = \hat{\sigma}_x\hat{\rho}_{\rm Q}\hat{\sigma}_x^\dagger$ is the targeted ideal swapped state. The error resulting from the NOT gate operation is thus given by $\varepsilon(\hat{\rho}_{\rm Q}, \hat{\rho}_{\rm R}) = 1 - F(\hat{\rho}_{\rm Q}, \hat{\rho}_{\rm R})$. We immediately recognize that the gate error decreases as the average photon number in the resonator increases (see figure 3.8a).

3.4 Quantum driving

Experimentally, we demonstrate transmon–resonator interaction by introducing a classical microwave drive into the system. The drive is used to generate coherent states in the resonator from the vacuum state [35] and thus, controlling the state of the transmon. This process of controlling the state of the transmon via coherent states generated from classical drive is called quantum driving. The external drive is modelled as a QHO with the Hamiltonian $\hat{H}_{\rm D} = \hbar\omega_{\rm d}\hat{d}^\dagger\hat{d}$. The description of a resonator coupled to an external drive is encapsulated in the Hamiltonian [54]

$$\hat{H}_{\rm DR} = \big(\mathcal{E}(t)e^{{\rm i}\omega_{\rm d}t} + \mathcal{E}^*(t)e^{-{\rm i}\omega_{\rm d}t}\big) \otimes (\hat{a} + \hat{a}^\dagger), \tag{3.57}$$

where $\mathcal{E}(t)$ and $\omega_{\rm d}$ are the complex amplitude and the frequency of the drive, respectively. The total Hamiltonian including the effect of drive now reads

$$\hat{H} = \hat{H}_{\rm JC} + \hat{H}_{\rm D} + \hat{H}_{\rm DR}, \tag{3.58}$$

where $\hat{H}_{\rm JC}$ is the standard JC Hamiltonian from equation (3.44). The external drive is operated with very large amplitude fields, where quantum fluctuations are considered negligible. Therefore, the drive is considered to be in a highly coherent state and is described by classical fields. To incorporate this, we make use of the time-dependent displacement operator in equation (3.19) and employ the displacement transformation [54, 55]

$$\hat{H}' = \hat{D}^\dagger\hat{H}\hat{D} - {\rm i}\hat{D}^\dagger(\partial_t\hat{D}), \tag{3.59}$$

$$= \hbar\omega_{\rm r}\hat{a}^\dagger\hat{a} + \frac{\hbar}{2}\omega_{\rm q}\hat{\sigma}_z + \hbar g(\hat{\sigma}_- \otimes \hat{a}^\dagger + \hat{\sigma}_+ \otimes \hat{a}) + \hbar g(\alpha^*\hat{\sigma}_- + \alpha\hat{\sigma}_+), \tag{3.60}$$

where $\alpha(t)$ is chosen to satisfy $\dot{\alpha} = -\mathrm{i}(\omega_{\mathrm{r}}\alpha + \mathcal{E}(t)e^{-\mathrm{i}\omega_{\mathrm{d}}t})$, eliminating direct driving of the resonator. The displaced Hamiltonian in equation (3.59) can be further simplified by moving to a rotating frame of the drive through an unitary transformation, yielding the driven JC Hamiltonian

$$\hat{H}'' = \hat{U}_d^\dagger \hat{H}' \hat{U}_d^\dagger - \mathrm{i}(\partial_t \hat{U}_d)\hat{U}_d^\dagger, \tag{3.61}$$

$$= \hbar\Delta_{\mathrm{r}}\hat{a}^\dagger\hat{a} + \frac{\hbar}{2}\Delta_{\mathrm{q}}\hat{\sigma}_z + \hbar g(\hat{\sigma}_- \otimes \hat{a}^\dagger + \hat{\sigma}_+ \otimes \hat{a}) + \frac{\hbar}{2}(\Omega_{\mathrm{r}}^*(t)\hat{\sigma}_- + \Omega_{\mathrm{r}}(t)\hat{\sigma}_+), \tag{3.62}$$

where $\hat{U}_d = \exp[\mathrm{i}\omega_{\mathrm{d}}t(\hat{a}^\dagger\hat{a} + \hat{\sigma}_z/2)]$, $\Delta_{\mathrm{r}} = \omega_{\mathrm{r}} - \omega_{\mathrm{d}}$ and $\Delta_{\mathrm{q}} = \omega_{\mathrm{q}} - \omega_{\mathrm{d}}$ are the detuning of the resonator and transmon from the drive frequency, and $\Omega_{\mathrm{r}}(t) = 2g\alpha(t)$ is the Rabi frequency in the coherent state regime. For a constant drive amplitude $\mathcal{E} \to \alpha = \mathcal{E}/\Delta_{\mathrm{r}}$, the Rabi frequency becomes $\Omega_{\mathrm{r}} = 2g\mathcal{E}/\Delta_{\mathrm{R}}$. In the limit $\Delta_{\mathrm{R}} \gg \kappa/2$, the average photon number in the resonator can be estimated to be $\bar{n} \approx (\mathcal{E}/\Delta_{\mathrm{R}})^2$. Thus, we are able to generate coherent states with photon number $\bar{n}$ by simply connecting a classical RF source to the driving resonator. Utilizing this, we can perform a NOT gate operation with the desired average number of photons in the resonator.

This section provides us with a tool to generate coherent states from classical fields. Experimentally, the transition from classical fields to quantum-mechanical coherent states is facilitated by the use of a drive resonator that only takes discrete eigenmodes, that is, microwave photons. The drive resonator is connected to an external microwave source that injects RF pulses at the fundamental frequency of the drive resonator. The average photon number can be optimized by choosing a suitable pulse amplitude and length as described above. In the absence of the drive resonator, we recover the classical description of the microwave electromagnetic field.

3.5 Dispersive regime: off-resonant interaction

On resonance, interaction leads to maximally entangled states of the qubit, which are not ideal for quantum information processing tasks [54]. In addition, the control of the transmon states is limited in speed due to the high finesse of the resonator. To circumvent this, the interaction is modelled in the dispersive regime, where detuning $\Delta = |\omega_{\mathrm{q}} - \omega_{\mathrm{r}}|$ between the transmon and the resonator is large compared to coupling strength $g \ll \Delta$. To encapsulate this, we apply unitary transformation to the driven JC Hamiltonian in equation (3.61) [25]

$$\hat{H}_{\mathrm{UT}} = \hat{U}_{\mathrm{disp}}^\dagger \hat{H}'' \hat{U}_{\mathrm{disp}}^\dagger, \tag{3.63}$$

with unitary operator $\hat{U}_{\mathrm{disp}} = \exp\left[\frac{g}{\Delta}(\hat{\sigma}_- \otimes \hat{a}^\dagger + \hat{\sigma}_+ \otimes \hat{a})\right]$. After expanding the result to the second order correction in g/Δ, we attain the driven dispersive Hamiltonian in the

moving frame with the drive as

$$\hat{H}_{\text{disp}} = \hbar\Delta'_{\text{r}}\hat{a}^\dagger\hat{a} + \frac{\hbar}{2}(\Delta'_{\text{q}} + 2\chi\hat{a}^\dagger\hat{a})\hat{\sigma}_z + \hbar(\Omega^*_{\text{r}}(t)\hat{\sigma}_- + \Omega_{\text{r}}(t)\hat{\sigma}_+), \qquad (3.64)$$

where $\chi = -\frac{g^2}{\Delta}$ is referred to as the dispersive shift, $\Delta'_{\text{r}} = \Delta_{\text{r}} - \frac{g^2}{\Delta}$ and $\Delta'_{\text{q}} = \Delta_{\text{q}} + \frac{g^2}{\Delta}$ are the dressed frequencies for the resonator and the transmon, respectively. One can obtain a slightly more accurate results for the dispersive shift and the shift in the resonator frequency by employing the generalized JC Hamiltonian (3.43) in eq. (3.58). In the multi-level transmon approximation, the correction to the dispersive shift yields $\chi = -\frac{g^2 E_{\text{C}}/\hbar}{\Delta(\Delta - E_{\text{C}}/\hbar)}$ and the shift in the resonator frequency $\Delta'_{\text{r}} = \Delta_{\text{r}} - \frac{g^2}{\Delta - E_{\text{C}}/\hbar}$.

In the dispersive regime, transmon–resonator interaction offers two distinct interpretations: shift of the dressed qubit frequency (ac Stark shift) as a function of the average photon number in the resonator, or the dispersive shift of the dressed resonator frequency as a function of the transmon state. Depending on the task, one of these interpretations will be employed. For example, quantum nondemolition measurement (QND) [56, 57] of the transmon state will require the dispersive shift of the dressed resonator frequency, whereas calibrating the average photon number in the resonator will make use of the ac Stark shift of the qubit frequency.

In our discussion of the transmon–resonator system, we have assumed a dissipation-free time evolution of the coupled interaction. In a general discussion of an interacting quantum system, it is very important to include the effects of the dissipation introduced by resonator transmission losses κ, transmon spontaneous emission γ, and the dephasing γ_ϕ, which is caused by the random fluctuation of transmon eigenenergies [58, 59]. This is usually referred to as pure dephasing, which leads to loss of information of relative phase between the transmon eigenstates [60]. To describe the evolution of such system, one employs Lindblad master equation under Markovian-Born approximation [36]. However, the Pauli-X gate is implemented in a time frame much smaller than the relaxation or the dephasing times and thus, can be regarded as a unitary evolution.

4 METHODS

In this chapter, we put forward the numerical and the experimental techniques employed during the development of this thesis. Particularly, we make use of Quantum Toolbox in Python (QuTiP) library for the numerical study of the transmon–resonator interaction, and SONNET electromagnetic suites for the designing of the superconducting-circuit used in the experiments. We discuss briefly the cryogenics and the radio frequency control lines used for experiments in the measurement setup section. Finally, we conclude with the sample characterization schemes and methods for the implementation of the Pauli-X gate under the quantum driving experiments section.

4.1 Numerical study

In chapter 3, we looked at some of the analytical results of the JC Hamiltonian. In particular, on-resonant interaction in a standard JC Hamiltonian, resulting from the truncation of the transmon energy levels to the first two eigenstates. Consequently, we observed the Rabi oscillations that gave us a recipe to implement the Pauli-X gate operation. Additionally, we recognized that the error resulting from this operation goes down as we increase the average photon number in the resonator. However, the two-level approximation does not reveal the exact behavior that we observe in the experiments. Thus, we resort to numerical schemes to include the effect of the higher energy levels of the transmon in the description of the transmon–resonator interaction.

We take advantage of an open-source quantum toolbox built on Python's object-oriented framework, namely QuTiP [62, 63] for simulating the transmon–resonator interaction. QuTiP makes use of the standard scientific libraries like NumPy, Scipy, and optimization library Cython to efficiently simulate tasks that otherwise would take considerable amount of time due to exponential increase in computational parameters resulting from the increase in the size of the Hilbert space. Supplemented by the use of Matplotlib library, QuTiP offers a number of tools that aid in visualization of the quantum states, coherent superposition of the different basis states, and including, but not limited to, the qubit gate rotations on the Bloch sphere. All the available functionality required for a comprehensive study of an interacting quantum systems are shown in figure 4.1a.

With the help of the QuTiP library, one can build a description of an open or a closed
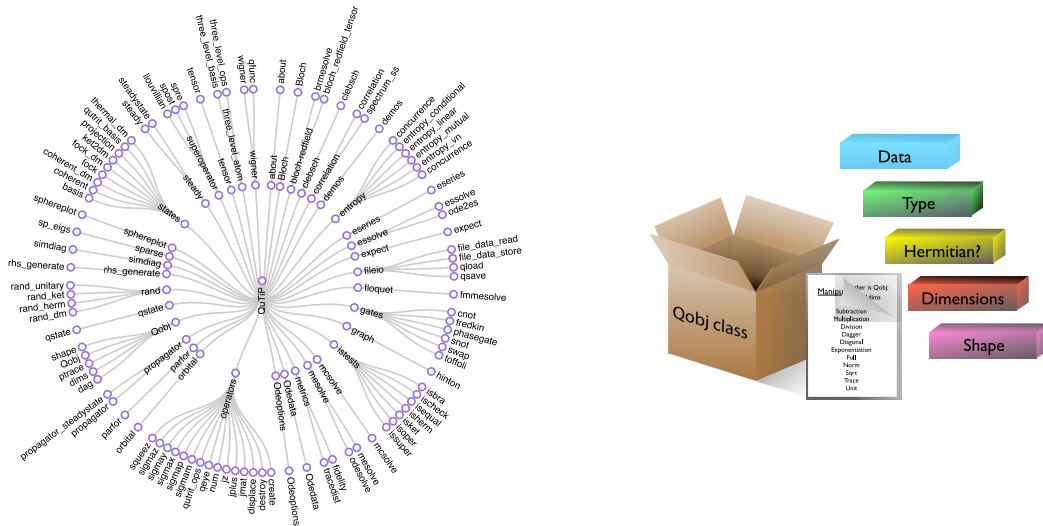
Figure 4.1. *QuTiP framework [61] **a)** An overview of the available functionality in the QuTiP library. The inner circle represents submodules of the library, whereas the outer circle displays all the functions and classes each submodule contains. **b)** A schematic description of object classes and the properties each object inherits when defined, alongside a few of the standard operations that can be done on the object.*

quantum system in matrix representations of the state vectors, density operators and relevant operators (Pauli, creation, annihilation, . . .), which are defined as object classes **Qobj**. Associated with each Qobj, there are class specific properties that describe a quantum state or an operator as depicted in figure 4.1b. In addition, QuTiP provides a dense library of standard functions and operations like partial trace **ptrace()** and tensor product **tensor()** to name a few [61].

As we have adopted density operator formalism for the discussion of an interacting quantum system, we choose operator-class objects to construct the quantum system describing the transmon–resonator interaction that we introduced in chapter 3. To facilitate this, we set up a time-dependent Hamiltonian (equation 3.61) in the rotating frame with the drive by using the associated set of operator objects. The time dependence in the Hamiltonian is introduced by simply adding the time-dependent drive Hamiltonian to the time-independent part in a Python list.

Once the Hamiltonian is constructed, we employ the master equation solver **mesolve()** in a finite dimensional Hilbert space setting, where the transmon and the resonator are truncated to $j = 3$ and $N = 200$ energy levels, respectively. This introduces an upper bound on the average number of photons ($\sqrt{\bar{n}} \ll N - \bar{n}$) that could be used for the implementation of the Pauli-X gate operation numerically. Furthermore, the inclusion of the first excited state $|\mathrm{f}\rangle$ results into an additional interaction term $\hbar\sqrt{2}g\big(|\mathrm{e}\rangle\langle\mathrm{f}| \otimes \hat{a}^{\dagger} + |\mathrm{f}\rangle\langle\mathrm{e}| \otimes \hat{a}\big)$ in the Hamiltonian (3.61) as suggested by the equation (3.43).

4.2 Superconducting-circuit design

In this section, we introduce the steps involved in the design process of the superconducting circuit used for the quantum driving experiments. The layout of the circuit corresponding to the desired parameters involves a few iterations of building the circuit layout and simulating it with an electromagnetic simulation software suite. We make use of an open-source layout editor KLayout for generating the circuit layout and commercial software Sonnet suites [64] for simulation of the circuit.
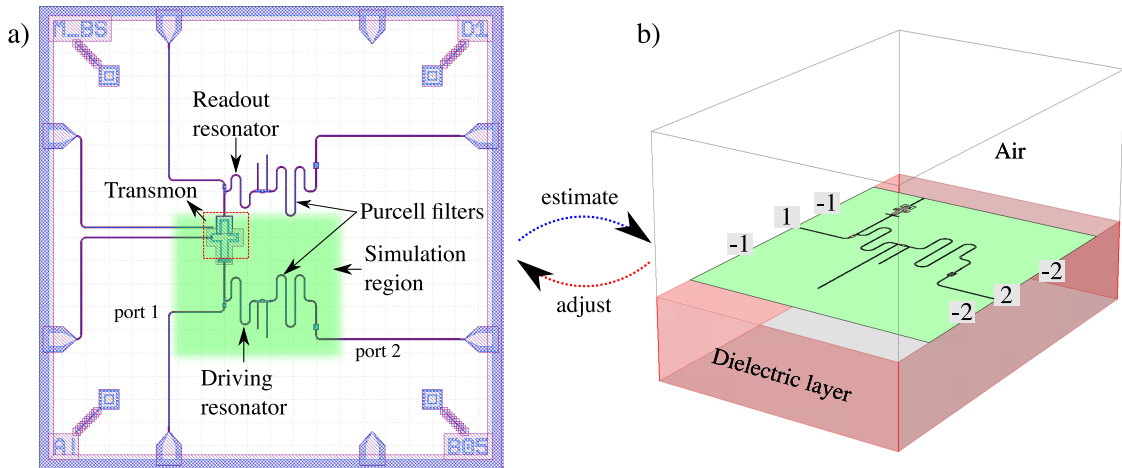
Figure 4.2. *Superconducting-circuit design scheme requiring a few iterations of generating circuit layout and its simulation.* **a)** *A schematic layout of a quantum driving sample with 1 transmon, 2 resonators, and 8 contact pads for control and readout use. In addition, each of the resonators, readout and driving, are weakly capacitively coupled to the Purcell filters to suppress the transmon decay rate. Due to relatively large size of the circuit and the memory cost of simulating such a large structure, only certain area (green) is exported to Sonnet for the estimation of the circuit parameters.* **b)** *A schematic illustration of the Sonnet simulation environment consisting of the superconducting-circuit inside a metal box, acting as a shield from an external electromagnetic field. The four sidewalls of the box are lossless metals and can be used for port connections as they provide perfect ground reference. The top and the bottom of the box can be freely chosen to correspond to any metal type, allowing modelling of the distinct loss mechanisms in the dielectric layers. After the simulation, the circuit layout is adjusted if the simulated results do not match with the expected design parameters.*

Sonnet performs an electromagnetic analysis of a 3D planar circuit enclosed in a shielded metal box by solving the Maxwell's equations using techniques like the method of moments and FFT (Fast Fourier Transform) [65, 66]. The analysis involves subdivision of a planar circuit into small rectangular subsections. Due to the voltage applied at the input port, a current distribution is expected on the planar surface of the circuit. Consequently, each subsection is analysed individually by keeping track of the current in section. Current induces tangential electric fields at the boundaries of each subsection. Having built a network of the tangential electric fields, resulting from each subsection, the current is ad-

justed such that the total tangential electric field vanishes for all metal surfaces in a planar circuit. Once the adjusted surface currents are known, the result of the analysis comes out as a N-port scattering matrix [45], which is processed further with either Matlab or Python.

We generate the circuit model using the layout editor and export it to Sonnet for electromagnetic simulation as discussed in figure 4.2. The size of the circuit is relatively large and takes long to simulate, thus we divide the circuit into smaller simulation regions and analyse them one at a time. The superconducting-circuit is modelled as a zero-thickness planar metal structure supported on a $500\,\mu m$ thick silicon substrate and with $2\,mm$ thick air layer on top of the circuit. In practice, the metal structure is fabricated with $200\,nm$ thin superconducting Niobium layer. Since the circuit is implemented as CPW structure, ground planes are assigned with negative port numbers and the center conductor with the positive ones, see figure 4.2b. The frequency response of the circuit is studied by analysing a 2x2 scattering matrix, in particular with the S_{21} parameter, as the circuit design is a transmission-type setup.

Since the superconducting-circuit is operated inside a dilution refrigerator, where temperature goes well below $20\,mK$, we set the material parameters such that they correspond to cryogenic temperatures. In this scenario, Niobium exhibits superconductivity and thus, requires us to consider kinetic inductance as its only material parameter. We do so by approximating the London penetration depth λ_L using the Ref. [67] and estimating sheet inductance of $L_{\mathrm{sh}} \approx 50\,fH$ at sub-kelvin temperature. As for the silicon substrate, we use the following standard parameters: $\epsilon_{\mathrm{r}} = 11.45$, $\mu_{\mathrm{r}} = 1$, $\tan\delta_{\mathrm{e}} = 10^{-6}$, and $\tan\delta_{\mathrm{m}} = 10^{-6}$, corresponding to relative permittivity, permeability and their loss tangents respectively.

Quantum driving sample

To demonstrate quantum driving of the transmon for gate error analysis, we require two resonators coupled to the transmon (see figure 4.2a). One of these resonator will be used for reading out the state of the transmon. Thus, we shall call this resonator naturally, a readout resonator. The transmon and the readout resonator interaction is modelled in a dispersive regime as discussed in section 3.5. We address the second resonator as a driving resonator, since it will be utilized to generate coherent states with $\bar{n}$ average photons by means of a classical drive as mentioned in section 3.4. The interaction of the transmon coupled to a driving resonator is required to take place in both on-resonant and off-resonant regime, the exact details of which are discussed in section 4.5.

The resonator frequency can be designed to any desired value by selectively choosing the center conductor width w and spacing s between the ground plane and the center conductor, and length d (see figures 3.2a and 3.2b) as established by the conformal mapping technique described in full details in Ref. [46] and briefly in section 3.1.2. There

is also a contribution from the kinetic inductance [68], however it is two orders of magnitude smaller than the geometrical inductance arising from the conformal mapping and therefore, can be disregarded. In addition to the Sonnet simulations, we employ Quite Universal Circuit Simulator (QUCS) - an intergrated circuit simulator and the methods presented in Ref. [69] for the estimation of the resonator frequency.

The qubit frequency cannot be rigorously simulated with Sonnet as there aren't any circuit elements that can effectively describe a non-linear Josephson junction. We can however, use the Josephson inductance relation (3.23) and define an ideal linear inductance sweep that will approximately simulate the flux behaviour of a Josephson junction in Sonnet. Furthermore, equation (3.23) in conjunction with Ambegaokar–Baratoff relation [70, 71]

$$I_\mathrm{C} R_\mathrm{N} = \frac{\pi}{2} \frac{\Delta(t)}{e} \tanh \frac{\Delta(t)}{2K_\mathrm{B}T} \tag{4.1}$$

yields the Josephson energy and inductance

$$E_\mathrm{J} = \frac{\phi_0}{4R_\mathrm{N}} \frac{\Delta(t)}{e} \tanh \frac{\Delta(t)}{2K_\mathrm{B}T} \, , \tag{4.2}$$

$$L_\mathrm{J}(\phi) = \frac{\phi_0}{\pi^2 \cos\left(\frac{2\pi\phi}{\phi_0}\right)} \frac{R_\mathrm{N}}{\Delta(t)} \frac{e}{\tanh \frac{\Delta(t)}{2K_\mathrm{B}T}} \, , \tag{4.3}$$

respectively. Here I_C is the critical current of the junction, R_N is the normal state resistance of the junction, i.e., at room temperature, and $\Delta(t)$ is the superconducting gap energy as a function of time. This relationship allows us to design the qubit frequency by fabricating a junction with an appropriate room temperature resistance, which can be controlled very precisely with electron-beam lithography (EBL) technique. In our case, we use superconducting aluminium for the fabrication of the junction. Additionally, we can disregard the contribution from the junction capacitance in Sonnet simulations as it will be very small compared to the parallel shunt capacitance.

In section 3.5 we briefly discussed the source of decoherence in a superconducting-circuit, which led to the reduced lifetime of the transmon. The resonators coupled to the transmon are one decay channel introducing enhanced relaxation rates. To minimize the relaxation rate (often called the Purcell decay rate) imposed by a resonator, we capacitively couple (weakly) both the readout and the driving resonators to the Purcell filters (figure 4.2a) to suppress the transmon decay rates [72, 73].

Purcell filters introduce impedance mismatch at the transmon frequency, while allowing signals to be transmitted at the resonator frequency [74]. In quantum driving samples, both the resonator and the Purcell filter are fabricated as $\lambda/4$- CPW resonators with a matching resonant frequency.

4.3 Measurement setup

In this section, we discuss the use of the dilution refrigerator to create a cryogenic temperature environment needed for the operation of a superconducting-circuit and present the measurement setup used for the sample characterization and the quantum driving experiments.
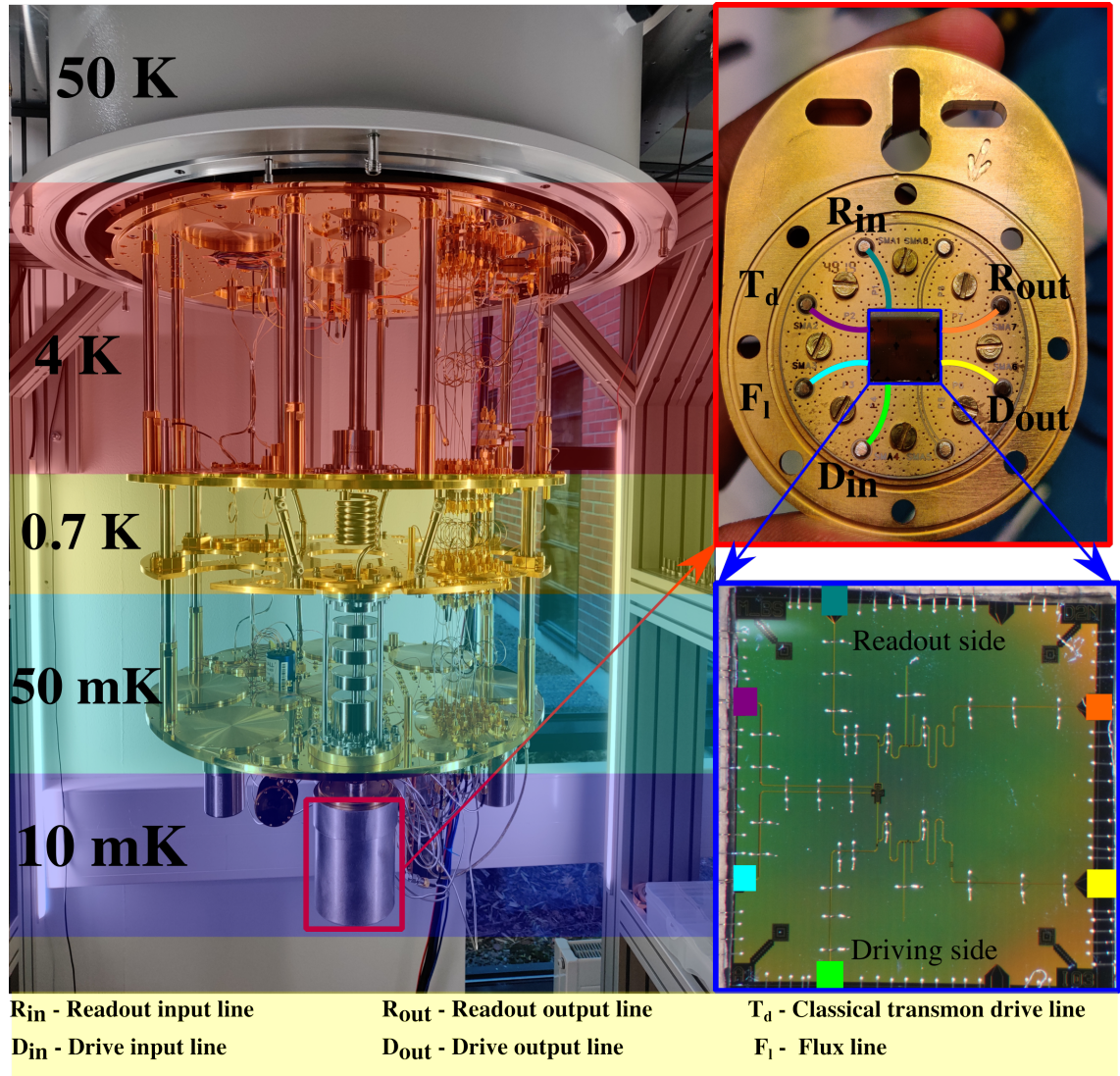
Figure 4.3. *Schematic depiction of a dilution refrigerator with several cooling stages marked with different colors and are annotated with attained base temperatures. Control lines are connected through each of these stages to the sample, allowing transmitting and receiving signals to/from the sample. These signals are passed through a series of electrical components like attenuators, isolators, amplifiers, and couplers, aiding in the minimization of the signal noise. The quantum driving sample (blue rectangle) is kept inside a sample holder, which itself is placed inside a magnetic shield (red rectangle) at 10 mK. The sample holder is marked with the port details, facilitating an ease of connecting them to the control and the output lines (top right). An optical microscope image of a quantum driving sample with corresponding color marked ports (bottom right).*

Dilution refrigerator

A typical working frequency of a resonator or a transmon is in the range of $3\,\text{GHz}$ to $10\,\text{GHz}$, which corresponds to a temperature range of $140\,\text{mK}$ to $480\,\text{mK}$. If the super-conducting circuits were to operate at the room temperature ($T = 300\,\text{K}$), we would not observe any quantum mechanical phenomena due to large thermal fluctuations in the circuit. Consequently, inhibiting us to exploit the associated quantum degrees of freedom offered by superconducting-circuits. Luckily, with the significant development in low temperature physics in the last 50 years, we are able to utilize commercially available dilution refrigerators that reach temperatures well in cryogenic region. We will not discuss in details the working principle of a dilution refrigerator as the subject is very rich and dense in itself.

In this thesis, we have utilized a commercial dilution refrigerator from BlueFors that does reach a base temperature of $10\,\text{mK}$. The dilution refrigerator consists of five distinct cooling stages, starting from $50\,\text{K}$ at the very top (hidden inside the outer cylinder of the cryostat) down to $10\,\text{mK}$ at the very bottom, where the sample is placed inside a magnetic shielding container. The details of the different cooling stages, control lines, and sample installation are briefly mentioned in figure 4.3.

Microwave control setup

In order to generate the coherent states, we apply the displacement operator on a vacuum state. Experimentally, this is done by connecting the input ports of the resonators to an external time-dependent voltage source $\mathcal{E}(t) = \mathcal{E}_0 \cos(\omega_\text{d} t + \varphi_\text{d})$, which creates continuously oscillating microwave signal at the desired frequency ω_d. Additionally, we require a microwave pulse rather than a continuous signal for the fast control and measurement of the transmon. Thus, we synthesize the desired microwave pulse $\Omega(t) = \Omega_0(t) \cos(\omega_\text{d} t + \varphi_\text{d})$ with the pulse envelope $\Omega_0(t) = \mathcal{E}_0 f(t)$, where $f(t)$ defines the pulse shape. We generate the pulse envelopes using an arbitrary waveform generator (AWG), which is implemented with field-programmable gate arrays (FPGA).

For all practical purposes, the microwave pulse is expressed in the complex representation $\tilde{\Omega}(t) = \Omega_0(t) e^{i\varphi_\text{d}} e^{i\omega_\text{d} t}$, where the original pulse is recovered by taking the real component. As a result, we are able to further separate the phasor term $\Omega_0(t) e^{i\varphi_\text{d}} = I(t) + iQ(t)$ into in-phase component $I(t) = \Omega_0(t) \cos(\varphi_\text{d})$ and π-shifted quadrature component $Q(t) = \Omega_0(t) \sin(\varphi_\text{d})$. This facilitates the characterization of the microwave signal in the phase space that is described by the in-phase and the quadrature components. In addition, the pulse envelopes for both IQ quadratures can be generated separately by choosing a desired phase φ_d, which can be effectively attained by utilizing the FPGAs. Pauli-X and Pauli-Y gates are implemented by setting the phase $\varphi_\text{d} = 0$ and $\varphi_\text{d} = \pi/2$,

respectively.
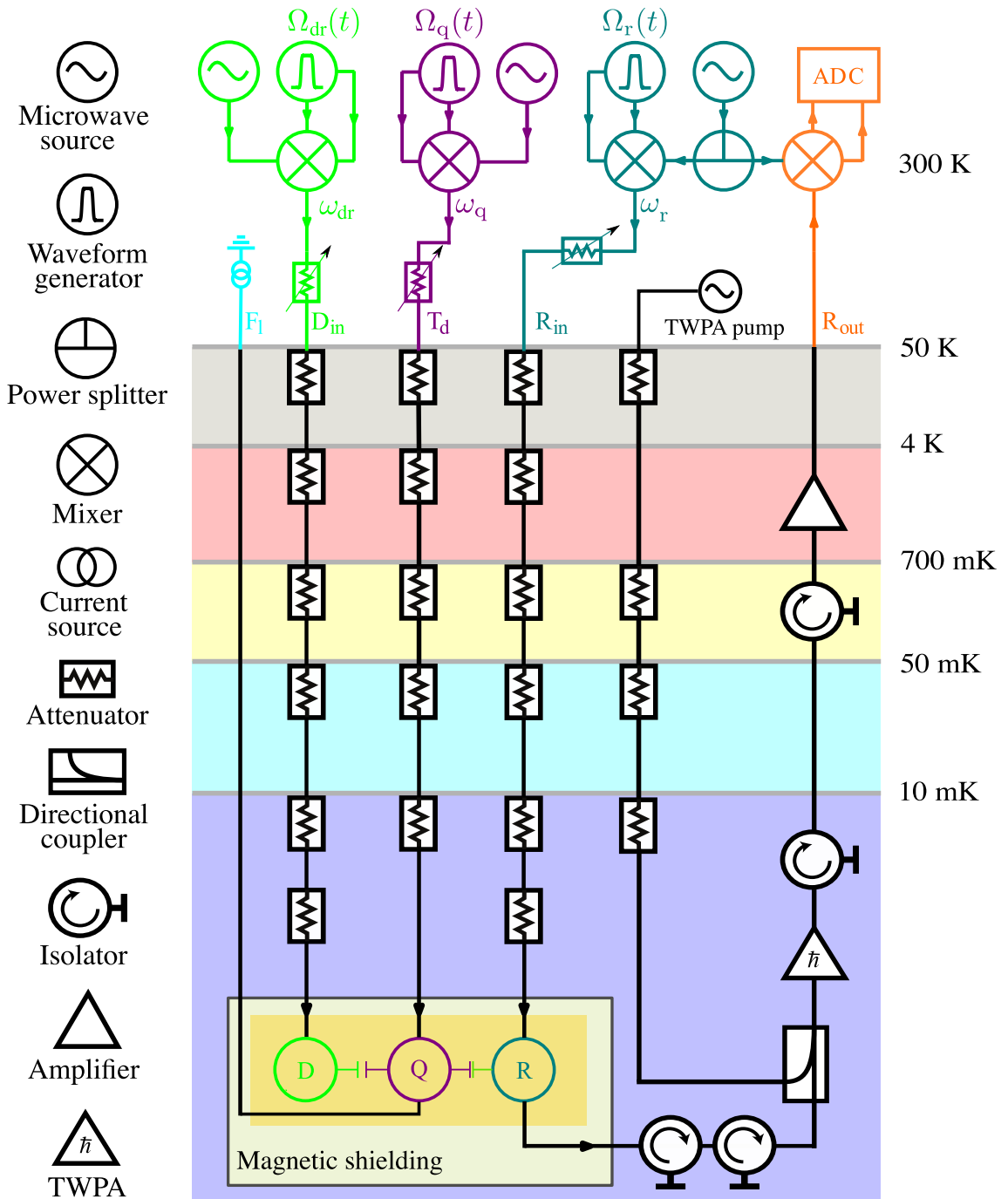
Figure 4.4. *A schematic representation of the heterodyne measurement setup, detailing the routing of control lines to the sample. Two RF lines are directed to the readout and driving input ports, marked with R_{in} and D_{in}, respectively. The flux behaviour of the Josephson junction is controlled by supplying bias current to it through the flux line F_l. A classical RF drive line T_d is used to control the state of the transmon independently from the readout/driving resonator and is mainly used for sample characterization. The output signal from the sample is transmitted through line R_{out}. To enhance the SNR of output signal, quantum-limited amplifier Josephson TWPA is used, which is controlled through TWPA pump line. In addition, attenuators distributed throughout the cooling stages and at room temperature are utilized to minimize the thermal noise coming from input lines.*

For quantum driving experiments, we require three sets of microwave pulse generators, each of which utilize a continuous microwave source, an AWG realized by a FPGA, and a mixer as shown in figure 4.4. We use a mixer to create for example, a readout pulse, where a microwave source generated continuous signal at ω_{r} is multiplied with readout pulse envelope $\Omega_{\mathrm{R}}(t)$ produced by a FPGA. Similarly, we create pulses separately for the classical transmon drive at ω_{q} and for driving resonator at ω_{dr} with pulse envelopes Ω_{q} and Ω_{dr} respectively. Each of these pulses are sent to their corresponding input ports on the sample via their own RF lines (see figure 4.4).

All the input lines are connected to a series of attenuators at each cooling stage inside the dilution refrigerator. These attenuators help to minimize the thermal noise introduced from the outside environment. Thus, we have used $60\,\mathrm{dB}$ attenuation for both readout R_{in} and driving D_{in} input lines, and $50\,\mathrm{dB}$ for transmon drive line T_{d}. In addition to these fixed attenuators installed inside the cryostat, we have also connected variable attenuators at room temperature to these lines.

The output signal from the readout resonator is transmitted through the line R_{out}, which is amplified by the quantum-limited nonlinear amplifier - Josephson traveling wave parametric amplifier (TWPA) - at $10\,\mathrm{mK}$. Additionally, we have also used a linear amplifier at $4\,\mathrm{K}$. The Josephson TWPA amplifier is controlled by a RF TWPA pump line, with $40\,\mathrm{dB}$ attenuation contributing directly from attenuators and $20\,\mathrm{dB}$ from the directional coupler. We have installed cryogenic isolators to prevent the reflection and thermal noise entering the sample from the output line. Furthermore, we have added a flux line F_{l}, which is connected to a DC current source. The flux line biases the Josephson junction, thus making the transmon frequency flux tunable. A full measurement setup, detailing the microwave control of the superconducting-circuit is presented in figure 4.4.

4.4 Sample characterization

The quantum driving sample needs to be characterized before proceeding with the experiments. The characterization of the sample helps us extract important parameters such as the readout and the driving resonator frequencies, the transition frequency ω_{ge} of the transmon, and in particular the π-pulse length for the implementation of the Pauli-X gate. In this section, we utilize standardized schemes presented in Ref. [75] for the characterization of a superconducting-circuit. Since the transmon is coupled to both the readout and the driving resonators, we start out with the characterization of the readout side and after that, we move on to the driving side of the sample.

The first step in the characterization process involves resonator spectroscopy, which is essentially carried out by employing the single-tone spectroscopy technique. In the single-tone spectroscopy, the resonator is continuously driven with a coherent tone at a probe frequency ω_{p} and either the reflected or transmitted signal is recorded; in our case, we

study the transmission spectrum. If the probe frequency is near to the resonator frequency, we see a peak in the transmission spectrum, since the resonator is brought in resonance by the probe tone. Note that the recorded resonator frequency includes the dispersive shift and does not correspond to the bare resonator frequency, as we are working in the dispersive regime.

Additionally, a flux sweep is introduced in the single-tone spectroscopy by applying a range of bias currents through the flux line. This causes the transition frequency of the transmon to shift as a function of an applied bias current I_ϕ as described in section 3.2.3. As a result, the observed resonator frequency shifts as a function of a bias current as [75]

$$\omega'_{\mathrm{r}}(I_\phi) = \frac{\omega_{\mathrm{r}} + \omega_{\mathrm{ge}}(I_\phi)}{2} \pm \sqrt{(2\pi g)^2 + \left[\frac{\omega_{\mathrm{ge}}(I_\phi) - \omega_{\mathrm{r}}}{4}\right]^2}, \qquad (4.4)$$

where ω'_{r} is the resonator frequency with a dispersive shift introduced by the ground state of the transmon and ω_{r} is a bare resonator frequency in an uncoupled environment. The flux dependent transition frequency of the transmon with a symmetrical SQUID is described by

$$\omega_{\mathrm{ge}}(I_\phi) = \omega_{\mathrm{ge}}^{\mathrm{max}} \left| \cos\left(\frac{\pi(I_\phi - I_{\mathrm{ss}})}{\Pi}\right) \right|^{\frac{1}{2}}, \qquad (4.5)$$

where $\omega_{\mathrm{ge}}^{\mathrm{max}}$ is the maximum transition frequency attained at bias current I_{ss}, usually referred to as the sweet-spot, and Π is the periodicity of the transmon in current. The maximum transmon frequency occurs exactly at an integer multiple of the normalized flux ϕ/ϕ_0. This gives us a one-to-one mapping between the bias current and the normalized flux. The conversion relation is extracted from the fitting of the measured resonator frequency with theoretical model dictated by equation (4.4). For the rest of the characterization, we make use of the normalized flux value instead of the bias current. In addition to the current–flux relationship, we also get an estimation for the bare transmon frequency and the coupling constant g from the fitting.

Having extracted the parameters from the fitting, we again measure the resonator frequency around the sweet-spot with a 2-µs-long readout pulse. With this measurement, we set the resonator frequency and normalized flux corresponding to the sweet-spot for the rest of the characterization process. In order to characterize the transmon frequency, we adopt a two-tone spectroscopy method, where we probe the resonator transmission at a frequency $\omega'_{\mathrm{r}}(\phi)$, while driving the transmon at a frequency ω_{d} with a pulse length of 10 µs. Consequently, when the drive frequency is far from the transmon frequency for a given flux value, the resonator transmission will be unaffected. However, when driven at resonance, the resonator transmission will experience a dispersive shift and will result in a lower transmission amplitude. Therefore, we locate the dip in the spectrum when performing the two-tone spectroscopy. This process is again repeated for a range of flux values thus, yielding us a flux behaviour of a transmon frequency. We remind that the

measured transmon frequency includes the dispersive shift.

Next, we calibrate the π-pulse length for the excitation of the transmon from the ground state. This is accomplished by driving the transmon at the measured transition frequency through the line T_d with a pulse envelope

$$\Omega_\mathrm{q}(t) = \begin{cases} \mathcal{E}_0 \sin^2\left(\pi \frac{t-t_0}{t_\mathrm{e}-t_0}\right), & t \in [t_0, t_\mathrm{e}], \\ 0, & \text{otherwise}, \end{cases}$$

where $\mathcal{E}_0$ is the amplitude of the pulse and $t_\mathrm{e} - t_0$ is the pulse length. For the estimation of the π-pulse, the amplitude is kept constant, while the length is varied until a proper Rabi oscillation is observed. Note that this π-pulse length is not the same as the one that will be used for the quantum driving experiments, where the π-pulse length is calibrated for the driving resonator and is discussed in details in the next section.

It is customary and most of the times very useful to report the experimental values of the dissipation parameters that were introduced in section 3.5. In order to estimate the transmon lifetime T_1, the transmon is driven to the excited state with the previously calibrated π-pulse [76]. During the decay of the transmon to the ground state, the resonator transmission is probed at the measured resonator frequency by sweeping the readout pulse delay. On the other hand, the dephasing time T_2 is obtained through the Ramsey interferometry [77, 78], where two $\pi/2$-pulses are applied at a certain interval apart. During this time interval, the transmon precesses freely on the equator of the Bloch sphere, thus quantifying the dephasing time.

Lastly, we measure the dispersive shift χ by exciting the transmon with a π-pulse and immediately probing the resonator transmission to measure the resonator frequency with the dispersive shift introduced by the excited state.

4.5   Quantum driving with coherent states

In this thesis, we are attempting to minimize the error resulting from the implementation of a Pauli-X gate operation. Keeping this in mind, we recognize the observation we made in section 3.3.4, that is, the inverse dependence of the π-pulse length on the fluctuation of the photon number $\Delta n = \sqrt{\bar{n}}$. Immediately, we realize that by increasing the number of average coherent photons in the resonator, we shorten the π-pulse length and thus, make the gate operation faster. A fast gate operation is always preferred as it allows us to perform many operations before the dissipation comes into effect. Furthermore, we will see in the numerical results section that the error from the gate operation also decreases as the average photon number is increased in the driving resonator.

For the experimental implementation, we propose the following gate operation protocol:

(i) The resonator is initialized in the ground state $|g\rangle$ by simply blocking any signal going to the driving resonator.

(ii) An average photon number $\bar{n}$ is pumped to the driving resonator.

(iii) The transmon is immediately tuned to the driving resonator frequency through the flux pulse.

(iv) The transmon–resonator interaction takes place for the duration of the π-pulse length in the resonant picture.

(v) The transmon is detuned back to the frequency at the sweet spot.

(vi) The state of the transmon is measured by probing the readout resonator at its measured frequency corresponding to the excited state.

(vii) For a given $\bar{n}$, steps (ii)-(vi) are repeated to calculate an ensemble average of the resulting error from the Pauli-X gate operation.

(viii) Steps (i)-(vii) are repeated by varying the average photon number in the driving resonator.

As required by step (ii), we establish an empirical method that allows us to pump a desired average photon number to the driving resonator. To achieve this, we first consider the interaction of the transmon and driving resonator in the dispersive regime, where the transmon frequency acquires an ac Stark shift. In the limit, $\kappa > \chi$, i.e., the driving resonator linewidth being larger than the dispersive shift, the ac Stark shift is given by

$$\Delta_{\mathrm{Stark}} = 2\chi\bar{n}\,, \tag{4.6}$$

which tells us that the transmon frequency acquires a frequency shift of 2χ per photon in the driving resonator. This allows us to calibrate the photon number in the driving resonator by performing the power spectroscopy of the transmon. In power spectroscopy, we vary the input power sent to the input line of the driving resonator and measure the Stark shift induced in the transmon frequency.

In our setup, we change the input power to the driving resonator by varying the attenuation of the variable attenuator installed outside of the dilution refrigerator as shown in figure 4.4. For a given attenuation value, we excite the transmon through the drive line T_{d}, while the driving resonator is driven simultaneously. Immediately after the drive pulse ends, the resonator is probed to measure the shift in the transmon frequency. Having repeated the measurement with a range of attenuation values, we extract the conversion rate between the attenuation and the photon number. This allows us to pump any number of coherent photons in the driving resonator by setting the variable attenuator to a value given by the conversion rate.

Since the driving resonator and the transmon are initially far-detuned, we need to bring
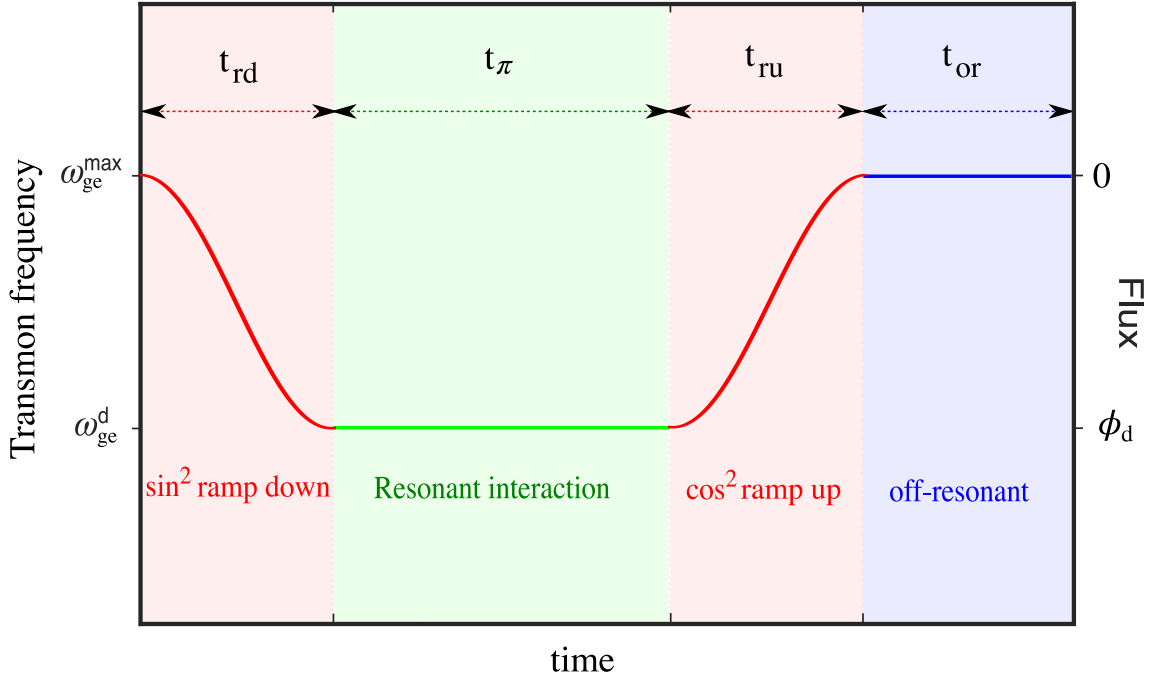
Figure 4.5. *Flux pulse sequence. The transmon is brought to the driving frequency $\omega_{\mathrm{dr}} = \omega_{\mathrm{ge}}^{\mathrm{d}}$ from the maximum frequency $\omega_{\mathrm{ge}}^{\mathrm{max}}$. The flux values corresponding to these frequencies are extracted from the sample characterization process. The pulse sequence describes the steps (iii)-(v) of the gate protocol.*

the transmon to the driving resonator frequency by applying a sequence of flux pulses to the flux line F_l. These sequences are generated using a FPGA. Mathematically, the flux pulse is written as (see figure 4.5 for the visualization of the pulse sequence)

$$\phi(t) = \begin{cases} \phi_{\mathrm{d}} \sin^2\left(\pi\frac{t-t_0}{2t_{\mathrm{rd}}}\right), & t \in [t_0, t_{\mathrm{rd}}], \\ \phi_{\mathrm{d}}, & t \in [t_{\mathrm{rd}}, t_{\mathrm{rd}}+t_\pi], \\ \phi_{\mathrm{d}} \cos^2\left(\pi\frac{t-(t_{\mathrm{rd}}+t_\pi)}{2t_{\mathrm{ru}}}\right), & t \in [t_{\mathrm{rd}}+t_\pi, t_{\mathrm{rd}}+t_\pi+t_{\mathrm{ru}}], \\ 0, & t \in [t_{\mathrm{rd}}+t_\pi+t_{\mathrm{ru}}, t_{\mathrm{rd}}+t_\pi+t_{\mathrm{ru}}+t_{\mathrm{or}}]. \end{cases}$$

As described in step (iv) of the protocol, we require a calibration of the π-pulse length for the driving resonator. To this end, we choose the pulse envelope as described in section 3.4. Having extracted the transmon–resonator coupling constant g_{dr} for the driving resonator, we define a rectangular pulse $\Omega_{\mathrm{dr}}(t) = 2g_{\mathrm{dr}}\sqrt{\bar{n}}$ for some $t \in [t_0, t_1]$ and 0 elsewhere. With rectangular pulse, we can easily choose the average number of photons by setting the pulse length $t_1 - t_0$ to a desired value.

5 RESULTS AND ANALYSIS

We devote this chapter in presenting the numerical and the experimental results that were gathered during the course of this thesis. All the results are obtained using the tools discussed in chapter 4.

5.1 Numerical simulations

In this section, we produce the outcomes of the numerical study of the Jaynes–Cummings Hamiltonian in the resonant picture. In addition, we also numerically investigate the Pauli-X gate operation under the full gate protocol as outlined in section 4.5.

Resonant interaction

It is necessary for any numerical study to start with a simpler model that can be validated by a corresponding analytical results and afterwards build the complexity gradually for a comprehensive study of the cases that do not have any analytical solutions. To that extent, we begin with the resonant interaction between the transmon and the resonator, where both the transmon and the resonator are truncated to $j = 3$ and $N = 200$ energy levels, respectively. In all of the simulations, we have initialized the transmon in the ground state, marked by a red arrow pointing to the north pole of the Bloch sphere (figure 5.1).

We start by analyzing the results presented in figure 5.1, where the solutions of the resonant JC Hamiltonian are expressed in terms of the expected value of the Pauli operators and the projection operator to the first excited state as a function of time. The time evolution of the Pauli operators can be effectively visualized as the trajectory traced by a Bloch vector in the Bloch sphere. We observe that both the Pauli-Y and Pauli-Z operators oscillate between their eigenvalues, whereas the Pauli-X operator remains fairly close to 0, resulting in π-rotation around the x-axis. Thus, performing the desired Pauli-X gate operation. As expected, we also recognize the $\bar{n}$-dependence in the resulting oscillations of the operators depicted in figure 5.1(a,b), similar to the Rabi oscillations seen in figure 3.8. Thus, by increasing the average photon number in the resonator, we make the gate operation faster and higher in fidelity. Lastly, we note the tilting of the trajectory of the Bloch vector with respect to the z-axis, resulting in a quantifiable error induced from the

gate operation.
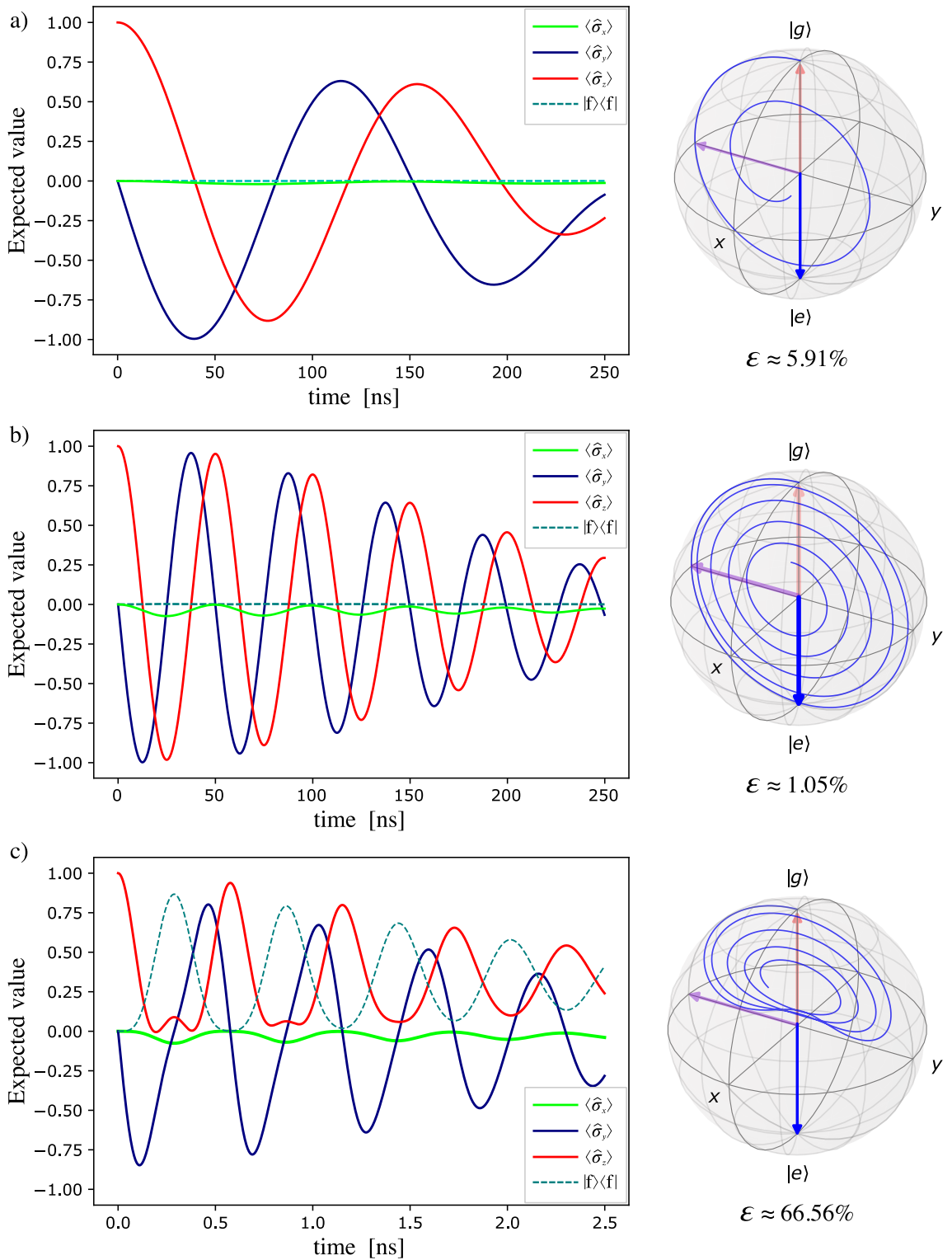
Figure 5.1. *Resonant interaction. The time evolution of the expected value of the Pauli operators and the projection operator to the first excited state. Visualization of the Pauli-X gate rotation on the Bloch sphere, where the trajectory of the rotation is given by the Pauli operators. The figures are obtained with conditions: **a)** $\bar{n} = 10$ and $g/2\pi = 1\,\mathrm{MHz}$, **b)** $\bar{n} = 100$ and $g/2\pi = 1\,\mathrm{MHz}$, and **c)** $\bar{n} = 100$ and $g/2\pi = 100\,\mathrm{MHz}$ with resulting gate error of 5.91%, 1.05%, and 66.56%, respectively.*

Additionally, we also examine the affect of the vacuum Rabi coupling strength g on the temporal evolution of the pauli-operators and the projection operator. For an average photon number $\bar{n} = 100$, we obtain the figures 5.1b and 5.1c corresponding to the coupling strength $g/2\pi = 1$ MHz and $g/2\pi = 100$ MHz, respectively. We notice that the large increase in the coupling strength leads to the occupation of the second excited state with a substantial probability, thus indicating a failure of the two-level approximation in the standard JC Hamiltonian. Consequently, we fail to perform the desired Pauli-X gate operation as the rotation of the Bloch vector is confined between the top half of the Bloch sphere, and thus resulting in a large gate error.

The π-pulse length is inversely proportional to both the coupling strength and the average photon number. Thus, it is only reasonable to make both larger in order to implement a faster gate operation. However, as seen earlier, increasing the coupling constant leads to a large gate error. As a result, we need to find an optimal value for the coupling strength that will keep the gate error small, while reducing the π-pulse length simultaneously. Motivated by this, we perform a simulation by varying both the average photon number in the resonator and the coupling strength and present the results in figure 5.2.
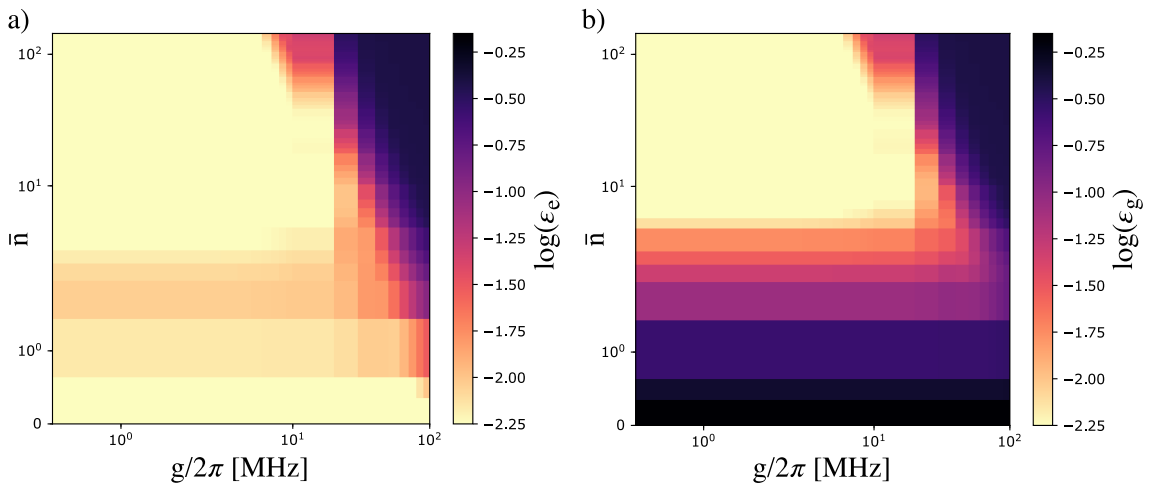
Figure 5.2. *Dependence of the gate error on the coupling strength g and the average photon number $\bar{n}$. The transmon is initialized **a)** in the excited state and **b)** in the ground state.*

The results depicted in figure 5.2 are acquired by varying the average photon number and the coupling strength in the range $\bar{n} \in [0, 100]$ and $g/2\pi \in [0.1, 100]$ MHz, respectively. For each combination of the coupling strength and the average photon number, we compute the gate error ε for each time step and record the minimum error resulting at the π-pulse length. As expected, we observe that the gate error gets better as the average photon number is increased in the resonator. However, we notice that the error does not improve with the increasing average photon number for larger coupling strength values. With this observation, we target the coupling strength $g/2\pi \leq 10$ MHz between the driving resonator and the transmon.
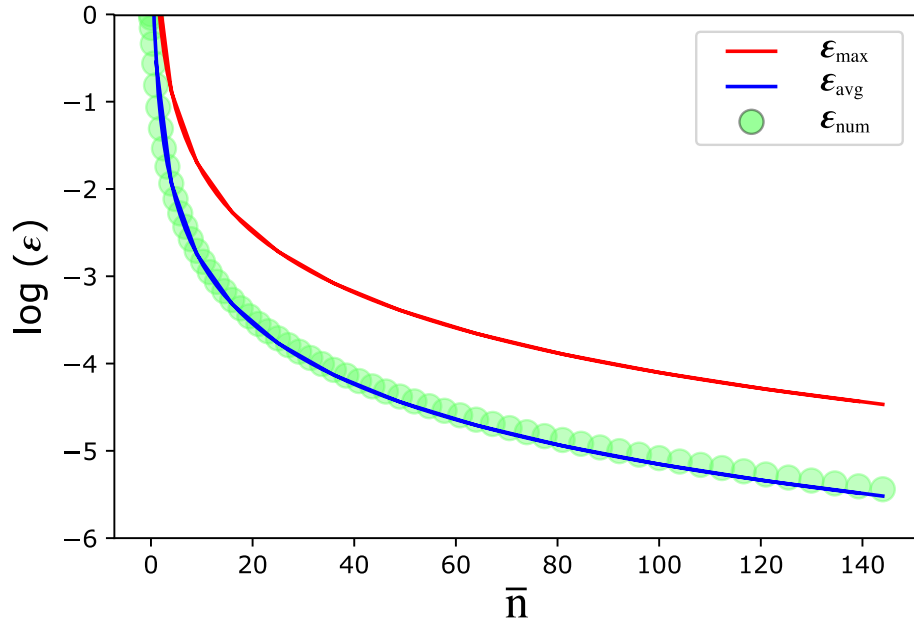
Figure 5.3. *Comparison of the gate error resulting from the numerical and the theoretical models. The gate error ε is plotted as a function of the average photon number $\bar{n}$, where the errors $\varepsilon_{\mathrm{max}}$ and $\varepsilon_{\mathrm{avg}}$ are given by the analytical expressions [37]. Numerical gate error $\varepsilon_{\mathrm{num}}$ corresponds to the slice at $g/2\pi = 1\,\mathrm{MHz}$ from figure 5.2b.*

Finally, we conclude the discussion of the resonant interaction by comparing the gate error resulting from the numerical simulations with the analytical expressions derived in Ref. [37]. We contrast the numerical gate error $\varepsilon_{\mathrm{num}}$ taken from the slice at $g/2\pi = 1\,\mathrm{MHz}$ in figure 5.2b with the analytical expressions of the average gate error $\varepsilon_{\mathrm{avg}}$ and the maximum gate error $\varepsilon_{\mathrm{max}}$. Here, $\varepsilon_{\mathrm{avg}} = (4 + \pi^2)/24\bar{n}$ is the ensemble average of the gate error over an uniformly distributed initial states of the transmon on the Bloch sphere, whereas $\varepsilon_{\mathrm{max}} = (4 + 4\pi + \pi^2)/16\bar{n}$ corresponds to the maximum error arising from one of the states in the uniformly distributed ensemble. We notice that the numerical results are in agreement with the analytical expression given by the average gate error. Note, that these analytical expressions are only valid for the Pauli-X gate rotation performed with the coherent photon states.

Full gate protocol

The resonant interaction does not describe the exact Pauli-X gate operation protocol outlined in section 4.5. The transmon frequency is initially detuned ($\omega_{\mathrm{q}} > \omega_{\mathrm{dr}}$) far from the driving resonator frequency and thus requires us to tune the transmon frequency by applying a flux bias in the SQUID. Following the steps from the protocol, we apply a drive pulse with the pulse amplitude $\Omega_{\mathrm{dr}}/2\pi = 90\,\mathrm{MHz}$ and the pulse length of $12\,\mathrm{ns}$, which corresponds to an average photon occupation of roughly $\bar{n} = 81$ in the driving resonator. Immediately, we apply a flux pulse with the characteristic pulse sequence lengths $t_{\mathrm{rd}} = t_{\mathrm{ru}} = 4\,\mathrm{ns}$, $t_{\pi} = \pi/18\,\mathrm{ns}$, and $t_{\mathrm{or}} = 20\,\mathrm{ns}$ (see figure 4.5 for the detailed description

of the flux pulse envelope); thus, resulting in the implementation of the full gate protocol. We compute the gate error at the end of the non-resonant interaction, which simulates the effect of the readout pulse on the Pauli-X gate operation.
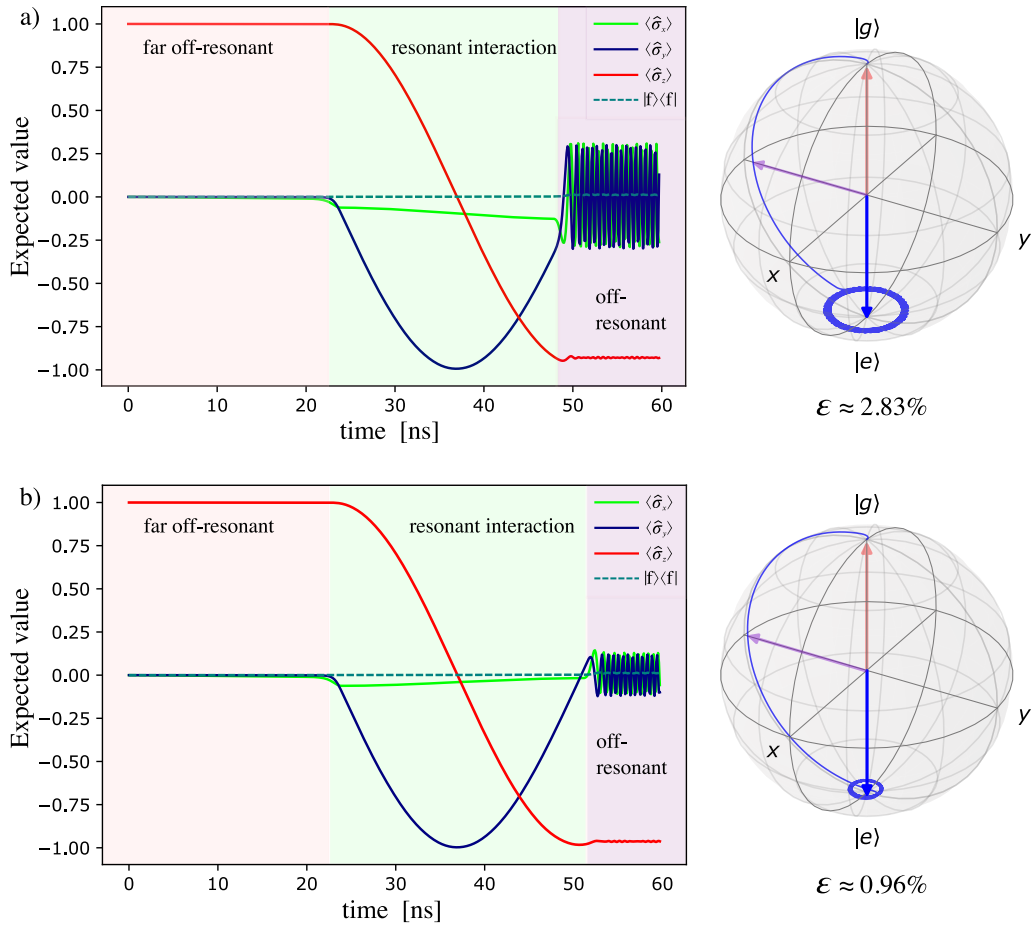

Figure 5.4. *Full gate protocol. The time evolution of the expected value of the Pauli operators and the projection operator to the first excited state. Visualization of the Pauli X-gate rotation on the Bloch sphere, where the trajectory of the rotation is given by the Pauli operators. The figures are obtained with the conditions:* $\Omega_{\mathrm{dr}}/2\pi = 90\,\mathrm{MHz}$ *and* $g/2\pi = 1\,\mathrm{MHz}$ *and detuning **a)** $\Delta/2\pi = 0$, and **b)** $\Delta/2\pi = -1\,\mathrm{MHz}$ between the transmon and the resonator during the resonant interaction with resulting gate error of* 2.83%, *and* 0.96%, *respectively.*

As one would expect, the transmon and the resonator stay unperturbed during the tuning of the transmon frequency. This is easily visualized in figure 5.4, where the expectation value of the Pauli operators remain constant in time. As soon as the transmon is tuned to the drive frequency, we observe an expected π-rotation of the Bloch vector, taking it from the ground state to the excited state. Additionally, we notice a large oscillation in the trajectory of the Bloch vector near the south pole of the Bloch sphere as shown in figure 5.4a, which results in a large gate error. This is minimized by introducing a slight detuning of 1 MHz as depicted in figure 5.4b. Note that we have not included the effect of dissipation in any of the simulations, since the time scale of the gate operation is assumed to be much smaller compared to the transmon lifetime and the dephasing time.

5.2 Superconducting-circuit design

In this section, we present the optimized design parameters for the quantum driving sample obtained from the Sonnet simulations. We begin by setting up the simulation for both the readout and driving side separately as mentioned in section 4.2. The geometry of a typical transmon–resonator system is defined in the simulation box and shown in figure 5.5a. The outcome of the simulation is processed with Matlab and is presented in figure 5.5b.
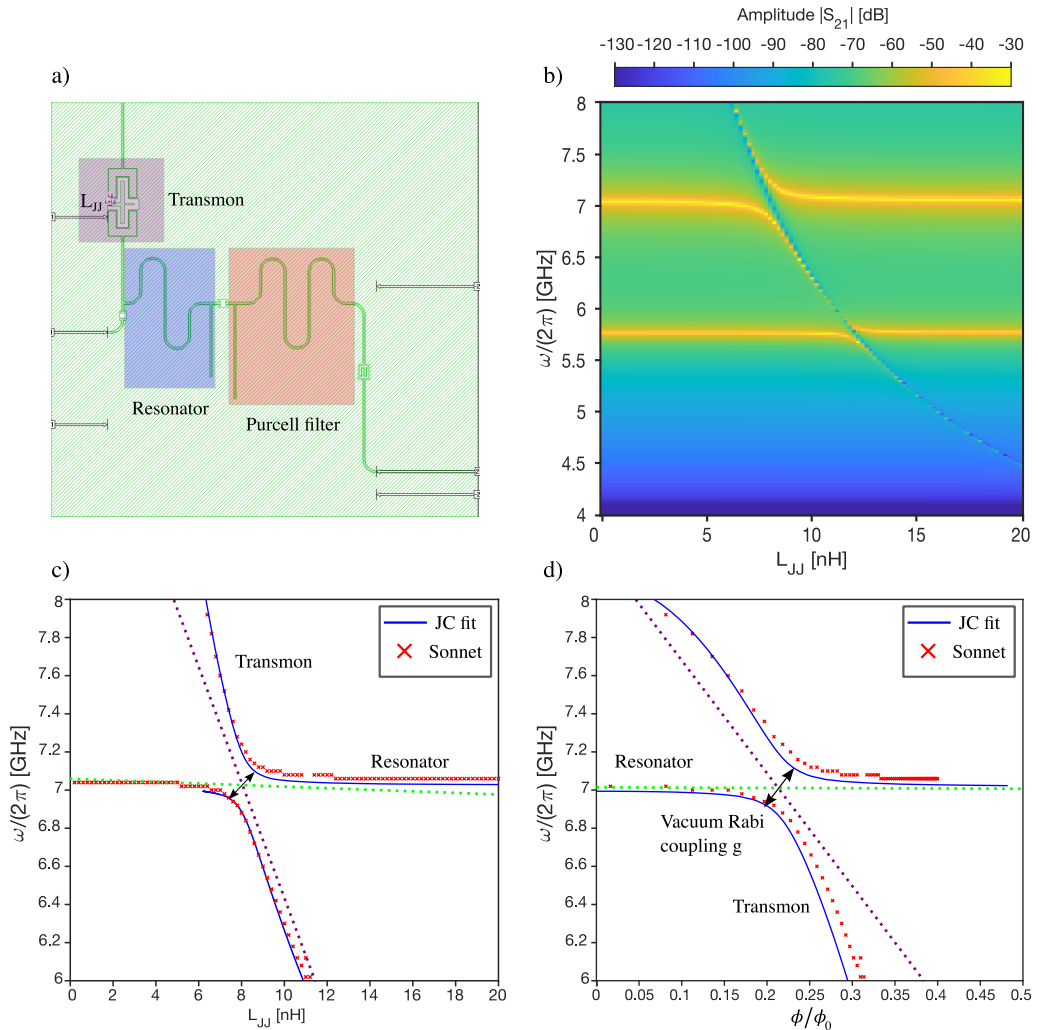
Figure 5.5. **a)** *A geometry of the transmon coupled to a resonator, which itself is weakly coupled to a Purcell filter.* **b)** *The frequency response of the coupled transmon–resonator system as a function of the Josephson inductance L_{JJ}. The bright yellow lines correspond to the resonant frequency of the resonator and the Purcell filter. The tunable transmon frequency leads to the avoided crossing at both the resonator and Purcell filter resonant frequencies. The avoided crossing corresponding to the resonator (larger separation) is fitted to a diagonalized standard JC Hamiltonian and the results are plotted against* **c)** *the Josephson inductance L_{JJ}, and* **d)** *an equivalent normalized flux ϕ/ϕ_0.*

We extract the essential parameters for the simulated design by fitting the frequency response of the transmon–resonator system to a standard JC Hamiltonian (3.44). As a

result, we attain the plot for eigenfrequencies of the JC Hamiltonian as a function of the Josephson inductance L_{JJ} and the normalized flux ϕ/ϕ_0 as shown in figure 5.5c and 5.5d, respectively. The most important parameter that we obtain from the fitting is the coupling strength of the transmon to the drive resonator. For the results presented in figure 5.5, the coupling strength is found to be $g/2\pi = 157.5\,\mathrm{MHz}$, which indicates a strong coupling of the resonator to the transmon.
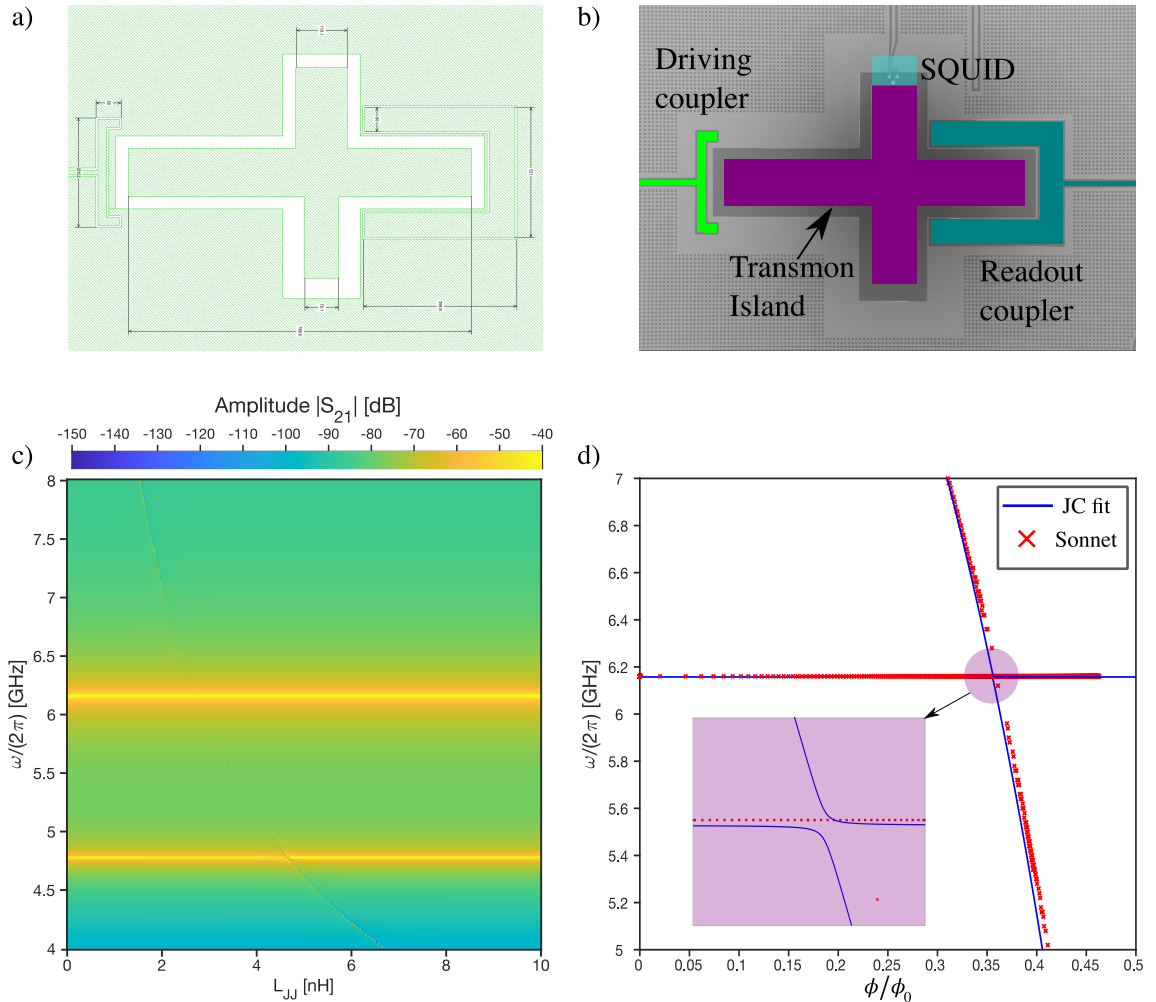
Figure 5.6. *Quantum driving sample.* **a)** *Sonnet geometry of the transmon island coupled to a weak driving coupler and a strong readout coupler.* **b)** *SEM image of the fabricated design.* **c)** *Frequency response of the driving resonator with a weak coupler as a function of the Josephson inductance* L_{JJ}. *A tunable transmon frequency (faint trace) introducing a negligible separation at the avoided crossing, as expected from a weakly coupled resonator.* **d)** *JC Hamiltonian fit to the simulated results, yielding fit parameters including coupling strength.*

For the quantum driving sample, we require a strongly coupled resonator for readout purpose and a weakly coupled resonator for driving the transmon as discussed in section 5.1. In section 3.3.1, we observed that the coupling strength depends on the ratio $g \sim C_{\mathrm{G}}/C_{\Sigma}$. Thus, by changing the ratio, we can effectively attain a desired value for the coupling strength. The design of the transmon island for the quantum driving sample

that fulfils the required criteria is shown in figure 5.6, alongside the SEM image of the fabricated sample and the simulated results. All the extracted parameters are recorded in table 5.1.

Simulation results.		
Parameters	**Symbol**	**Value**
Readout resonator	$\omega_{\mathrm{r}}/2\pi$	6.15 GHz
Driving resonator	$\omega_{\mathrm{dr}}/2\pi$	6.19 GHz
Coupling strength (Readout)	$g_{\mathrm{r}}/2\pi$	150 MHz
Coupling strength (Driving)	$g_{\mathrm{dr}}/2\pi$	7.50 MHz
Charging energy	$E_{\mathrm{C}}/\hbar$	70 MHz

Table 5.1. *Extracted parameters for the quantum driving sample.*

5.3   Sample characterization

This section includes the results from the characterization of the quantum driving sample. After the fabrication, the sample is installed inside of the dilution refrigeration with properly connected control lines, the details of which are discussed in section 4.3.
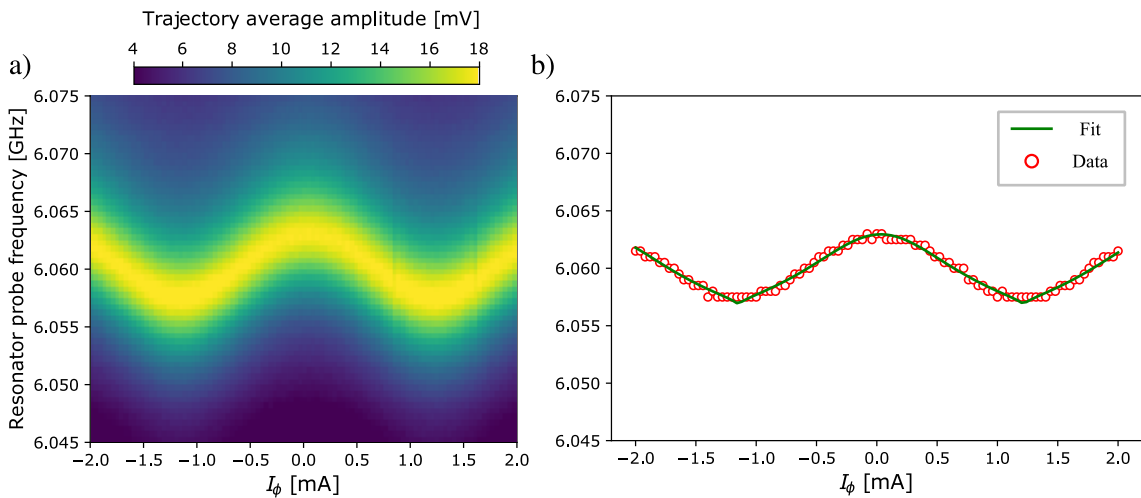
Figure 5.7.   *Single-tone spectroscopy.   **a)** Frequency response of the resonator as a function of the applied bias current I_ϕ and the probe frequency.   **b)** Obtained resonant frequencies (red circle) corresponding to the peak in the transmission spectra for a given bias current. The resonant frequencies are fitted (green line) to extract the flux conversion rate corresponding to the sweet spot.*

Since there are two resonators coupled to the transmon, one could characterize the sample using either of the resonators. We use the readout resonator for the characterization of the sample for convenience, as the driving resonator is weakly coupled to the transmon. The characterization follows sequential steps as described in section 4.4, starting with a single-tone spectroscopy of the resonator as shown in figure 5.7a.

The resonant frequency of the resonator is obtained from the spectroscopy data by locating the transmission peak for each bias current I_ϕ and is fitted using the equation (4.4). The fitting yields the flux conversion rate, which is taken at the sweet spot. Additionally, the fit also gives an estimation for the transmon frequency and the coupling strength. With these estimations, we perform two-tone spectroscopy of the transmon near the sweet spot. The resulting frequency response of the transmon as a function of the probe frequency and the normalized flux ϕ/ϕ_0 is shown in figure 5.8a. Thus, we obtain the readout resonator and the transmon frequencies $\omega_r/2\pi = 6.063$ GHz and $\omega_{ge}/2\pi = 3.5525$ GHz, respectively. The flux is set to the sweet spot corresponding to the maximum of the transmon frequency for the rest of the characterization. Next, we carry out the measurement of the Rabi oscillation to obtain the π-pulse length by driving the transmon at the frequency $\omega_{ge}/2\pi = 3.5525$ GHz as described in section 4.4. The measured Rabi oscillation with a π-pulse length $t_\pi = 64$ ns is shown in figure 5.8b.
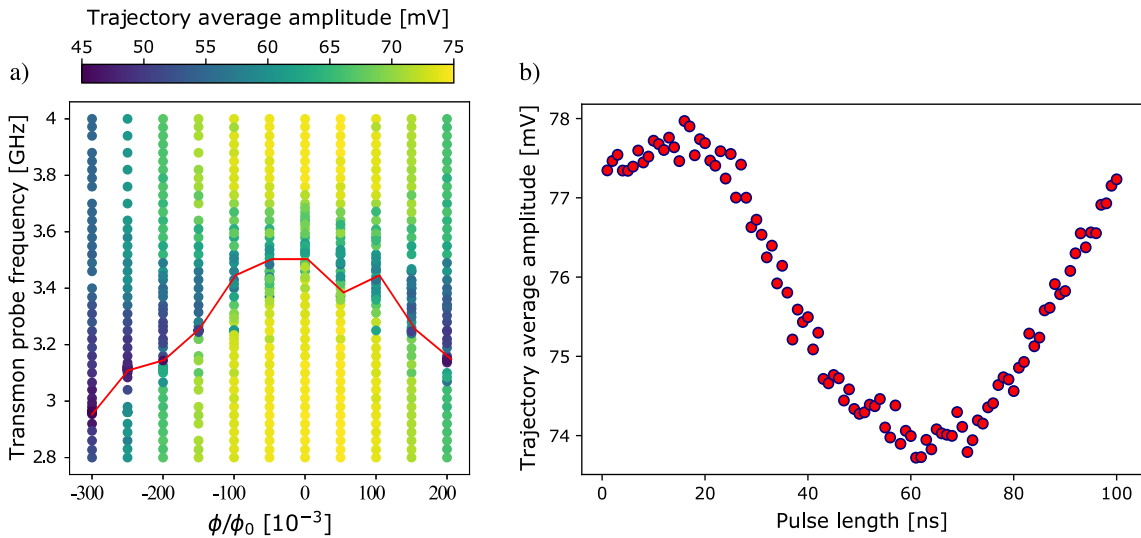
Figure 5.8. a) *Two-tone spectroscopy, yielding the frequency response of the transmon as a function of the normalized flux ϕ/ϕ_0 and the probe frequency. The resonant frequencies of the transmon are obtained by locating the dip in the transmission spectrum for each flux points and are fitted (red line) to extract the flux value corresponding to the sweet spot.* **b)** *Measured Rabi oscillation for the calibration of the π-pulse length. Each data point is obtained by taking an average of 10^4 repeated measurements.*

In order to obtain the dephasing time, we perform Ramsey interferometry by varying the precession time between two successive $\pi/2$-pulses and measuring the state of the transmon. As the precession time increases, the excited state population experiences a decay with a characteristic decay rate equal to the dephasing time T_2. Additionally, we obtain a precise transition frequency of the transmon from the Ramsey spectroscopy. Furthermore, Ramsey measurement for the second transition between states $|e\rangle - |f\rangle$ is also carried out to measure the anharmonicity of the transmon, which is found to be $E_C/\hbar = 70$ MHz. Results from the Ramsey measurement of the first and the second transition frequencies of the transmon are shown in figure 5.9a and b, respectively.
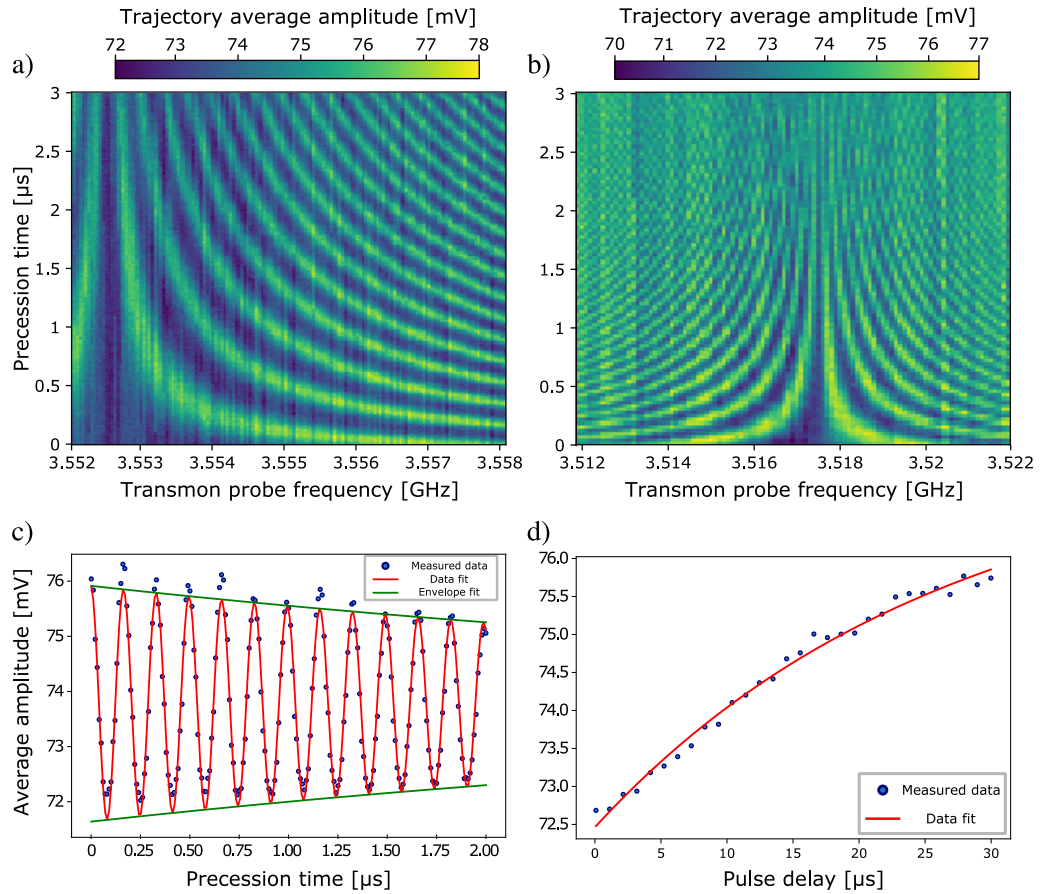
Figure 5.9. *Decoherence and dephasing characterization. Ramsey interferometry corresponding to the transition between states **a)** $|g\rangle - |e\rangle$, and **b)** $|e\rangle - |f\rangle$. **c)** Fitting of the Ramsey oscillation taken at the probe frequency $\omega_q/2\pi = 3.553\,\text{GHz}$ to an exponentially decaying envelope, yielding the dephasing time. **d)** Fitting of the data corresponding to the excited state population as a function of pulse delay. The decay constant of the exponential fit characterizes the relaxation time.*

We obtain the value for the dephasing time by fitting the data corresponding to the slice taken at the probe frequency $\omega_q/2\pi = 3.553\,\text{GHz}$ in figure 5.9a to an exponentially decaying oscillation as shown in figure 5.9c. Each of the data points in 5.9c is acquired by iterating the measurement 50 times, resulting in a dephasing time $T_2 = 5.02\,\mu\text{s}$. For the relaxation time T_1, we drive the transmon to the excited state through the transmon drive line F_l and probe the resonator to study the evolution of the excited state of the transmon with varying readout pulse delays. The measurement is repeated several times and the average amplitude is plotted against the readout pulse delay as presented in figure 5.9d. We fit the data to an exponential curve and obtain the relaxation time $T_1 = 26.37\,\mu\text{s}$. In general, the dephasing time should be twice as large as the relaxation time. However, due to the presence of other sources of decoherence, we obtain a small value for the dephasing time compared to the relaxation time.

Having the readout side of the sample characterized, we obtain the resonant frequency of the driving resonator by using a vector network analyser (VNA). After obtaining the rele-

vant characterization results, we encounter two of the major limitations making the quantum driving experiment unfeasible. First, the transmon frequency $\omega_{\mathrm{ge}} < \omega_{\mathrm{dr}} = 5.01\,\mathrm{GHz}$ must be larger than the frequency of the driving resonator, since we are required by the gate protocol to bring the transmon in resonance with the resonator for resonant interaction. Secondly, the anharmonicity of the transmon is quite small, which makes it difficult to fabricate a Josephson junction corresponding to a large transmon frequency, as the junction will have to be quite large as well. Additionally, small anharmonicity leads to the occupation of higher excited states as the transmon energy level resembles a harmonic oscillator.
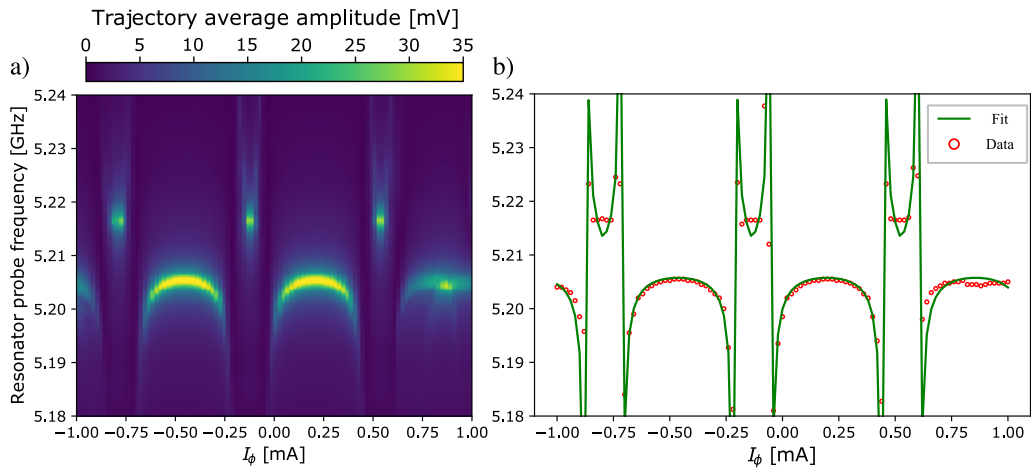
Figure 5.10. *Single-tone spectroscopy of the strongly coupled quantum driving sample.* **a)** *Frequency response of the resonator as a function of the applied bias current I_ϕ and the probe frequency. The tunable transmon frequency leads to an avoided crossing at the resonator frequency.* **b)** *Obtained resonant frequencies (red circles) correspond to the peak in the transmission spectra for a given bias current. The resonant frequencies are fitted (green line) to extract the flux conversion rate corresponding to the sweet spot.*

Despite the limitations introduced by the quantum driving sample, we perform some of the experimental tasks required in the implementation of the gate protocol for future study. Thus, we make use of an alternative sample, which has the exact same features as the quantum driving sample with a notable exception of a strongly coupled driving resonator. That is, both the readout and the driving resonator are strongly coupled to the transmon. Furthermore, the intention is to also test the numerical results corresponding to the large coupling strength of the strongly coupled driving resonator. We follow the similar steps and obtain the essential parameters for the strongly coupled quantum driving sample. Almost all of the characterization results of the strongly coupled sample exhibit similar features as the weakly coupled quantum driving sample, except for the outcome of the resonator spectroscopy. Since the transmon frequency in the strongly coupled sample is larger than both of the resonators, we observe an avoided crossing when the transmon frequency is tuned to the resonator frequency as depicted in figure 5.10a. Similar fitting process is adopted to extract the flux conversion rate as shown in figure 5.10b. The

results from the characterization of both samples are presented in table 5.2.

Sample characterization results.			
Parameters	**Symbol**	**Value: S1**	**Value: S2**
Resonator frequency (Readout)	$\omega_{\mathrm{r}}/2\pi$	6.063 GHz	5.205 GHz
Resonator frequency (Driving)	$\omega_{\mathrm{dr}}/2\pi$	5.01 GHz	5.59 GHz
Coupling strength (Readout)	$g_{\mathrm{r}}/2\pi$	206.31 MHz	114.26 MHz
Coupling strength (Driving)	$g_{\mathrm{dr}}/2\pi$	8.5 MHz	77.57 MHz
Transmon frequency	$\omega_{\mathrm{ge}}/2\pi$	3.5525 GHz	8.851 GHz
Transmon anharmonicity	$E_{\mathrm{C}}/\hbar$	70 MHz	285 MHz
π-pulse length	t_π	64 ns	100 ns
Relaxation time	T_1	26.37 µs	1.883 µs
Dephasing time	T_2	5.02 µs	0.245 µs
Dispersive shift	$\chi/2\pi$	0.46 MHz	0.0078 MHz

Table 5.2. *Essential parameters obtained from the measurements. Samples S1 and S2 correspond to the weakly and strongly coupled quantum driving samples, respectively.*

5.4 Quantum driving experiments

We utilize a strongly coupled sample to demonstrate two of the most important steps required for the implementation of a full gate protocol: photon number calibration and tunability of the transmon, so to match the resonant frequency of the driving resonator. In this section, we investigate and analyse the results associated with these two steps. We begin by examining the photon number calibration in the resonator using a power spectroscopy scheme as discussed in section 4.5. Before performing the power spectroscopy, we inspect the frequency response of the resonator as a function of the drive power, which is controlled by varying the attenuation of the variable attenuator, see figure 4.4.
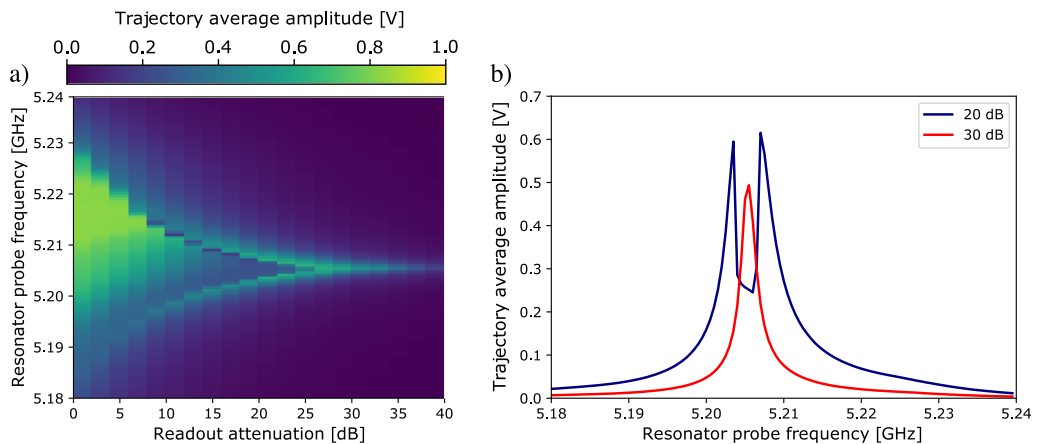
Figure 5.11. *Nonlinear vacuum Rabi splitting.* ***a)*** *Measured transmission spectra of the resonator as a function of an applied attenuation to the drive power.* ***b)*** *Supersplitting of a single transmission peak at* 30 dB *into a doublet at* 20 dB *attenuation.*

A transmon–resonator system exhibits the vacuum Rabi splitting, where a transmission peak of an uncoupled resonator splits into two in the presence of the transmon [44]. The separation of the resulting peaks is given by $2g$, which is a linear-response effect. Remarkably, we observe a further splitting of the transmission peak when the coupled two-level system is driven at high drive powers, corresponding to lower attenuation values as shown in figure 5.11. This nonlinear response is only obtained with a heterodyne measurement setup [79].
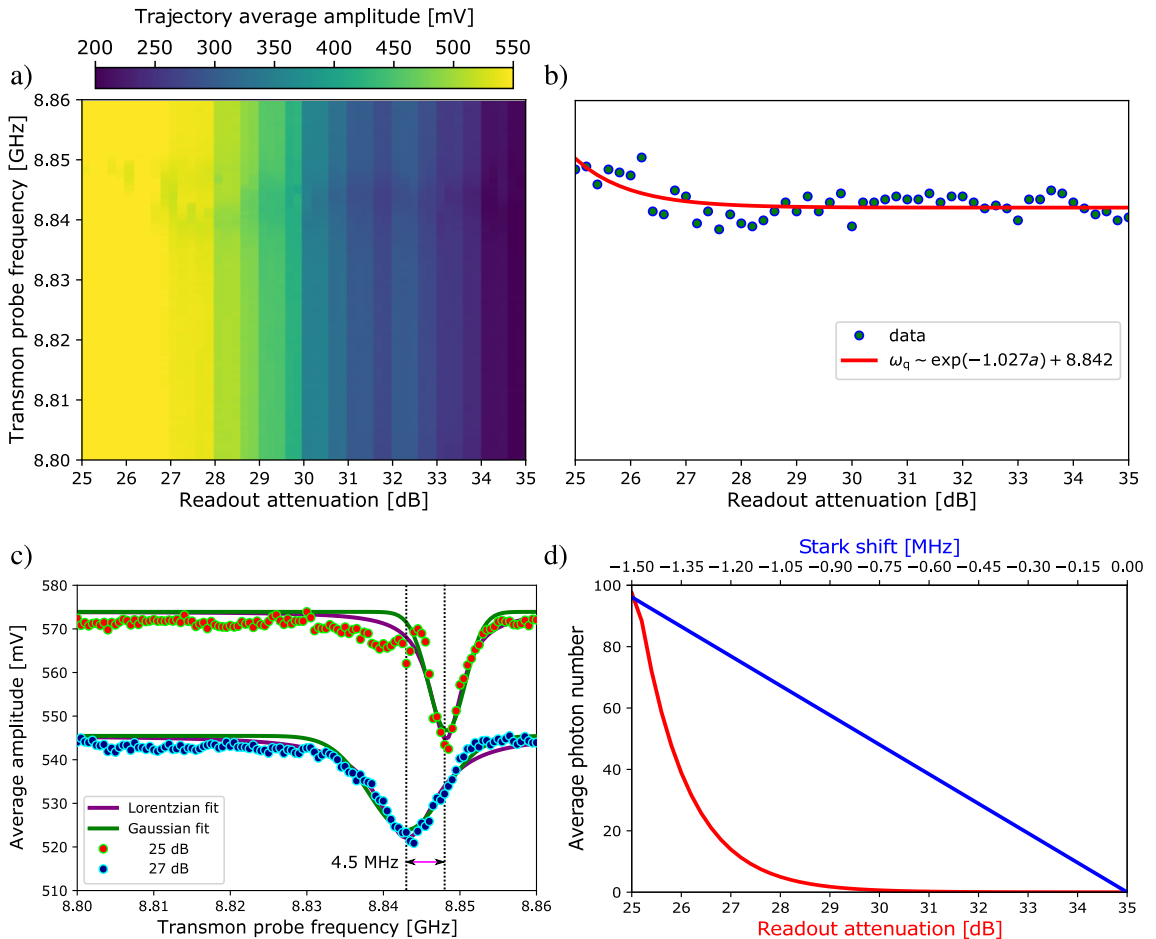
Figure 5.12. *Photon number calibration.* **a)** *Measured frequency response of the transmon as a function of an applied attenuation to the input line.* **b)** *Extracted transmon frequencies (blue circles) by locating the dip in the transmon spectra for each attenuation value. An exponential curve (red line) is fit to the extracted data.* **c)** *Transmon frequency response, taken at* 25 dB *(red circles) and* 27 dB *attenuation values, are fit to the Lorentzian (purple) and the Gaussian curves (green). The dip in the fittings is used to calculate the ac Stark shift of* 4.5 MHz. **d)** *Photon number is computed using equation* (4.6) *and plotted against attenuation (red) and ac Stark shift (blue).*

We perform the power spectroscopy in the linear regime by limiting the variable attenuator to only take values larger than 25 dB. We obtain the frequency response of the transmon as a function of the applied attenuation to the drive line as depicted in figure 5.12a. By changing the attenuation, we are effectively controlling the average number of photons in the resonator. This leads to a photon dependent shift (ac Stark effect) of the transmon

frequency. Thus, by studying the shift in the transition frequency, we calibrate the photon number in the resonator as a function of the attenuation.

Following the power spectroscopy, we extract the transmon frequencies by locating the dip in the spectra for each attenuation value and fit an exponentially decaying curve to the extracted data as presented in figure 5.12b. We obtain the average photon number by employing the equation (4.6), where the Stark shift is computed from the fitted exponential curve. For the strongly coupled quantum driving sample, we have experimentally found the dispersive shift to be $\chi/2\pi = 0.0078\,\text{MHz}$. Thus, the transmon must acquire a frequency shift of 2χ per photon, see figure 5.12d. Note that the variable attenuation is applied on top of the fixed $60\,\text{dB}$ attenuation, which is installed inside the cryostat.

Finally, we conclude this section by briefly discussing the possible difficulties that may arise when bringing the transmon in resonance with the driving resonator via flux spectroscopy. From figure 5.13, we realize that the transmon trace gets dimmer when moving away from the sweet spot. Operating the transmon far from the sweet spot will result into drastic flux noise as the slope gets rapidly steeper. Especially, in this case where we wish to bring the transmon frequency from $\omega_{\text{dr}}/2\pi = 8.85\,\text{GHz}$ to the drive resonator frequency $\omega_{\text{dr}}/2\pi = 5.59\,\text{GHz}$. Therefore, the bare transmon frequency must be designed such that we stay within the dispersive regime and are able to tune the transmon to the resonator frequency by setting the flux as close as possible to the the sweet spot flux value.
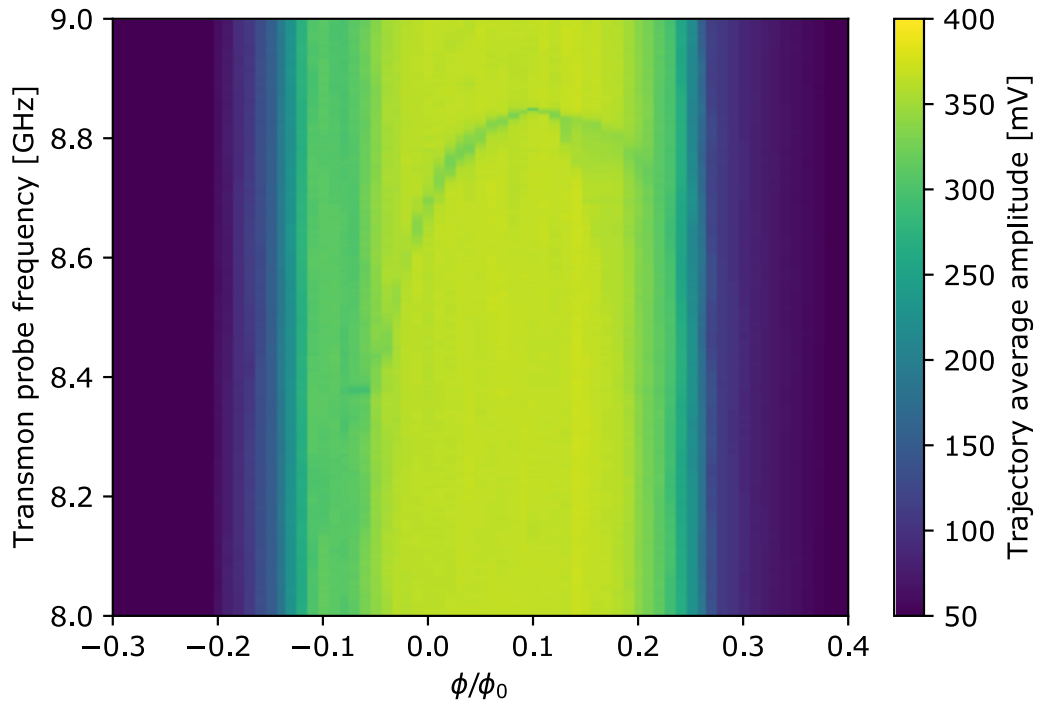
Figure 5.13. *Measured frequency response of the transmon as a function of the flux.*

6 CONCLUSIONS AND OUTLOOK

In this thesis, we set out to investigate both numerically and experimentally, a single-qubit gate operation scheme that minimizes the error resulting from the operation. In particular, we implement a Pauli-X gate, an equivalent operation to a classical NOT gate, on a superconducting transmon qubit. Traditionally, the gate operation is performed by directly driving the qubit with a classical field for the duration of a π-pulse in a dispersive regime. Alternatively, we propose a gate operation protocol that involves the quantum driving of the qubit, where the classical drive of the qubit is replaced by a coherent drive. Additionally, the gate operation is mediated by a resonant interaction between the qubit and the resonator, followed by an off-resonant interaction.

From the numerical simulations, we observed $1/\bar{n}$ - dependence of the gate error as predicted by the theory. Thus, by increasing the average photon number in the simulations, we effectively saw the reduction in the obtained error per gate operation. In addition, we also noticed an improvement in the gate error for smaller values of the coupling strength between the qubit and the resonator. For large coupling strength values, the occupation of the higher excited states were observed, which resulted in an incomplete implementation of the Pauli-X gate operation. Finally, in the simulations of the full gate protocol, we discovered large residual oscillations at the end of the gate operation for a fully resonant interaction. However, when introduced to a small detuning of $\Delta/2\pi = 1\,\mathrm{MHz}$ between the qubit and the resonator frequencies, we obtained small residual oscillations, which further improved the gate error results.

To facilitate the quantum driving experiments, we designed the layout of the superconducting circuit using a layout editor and optimized the parameters by performing an electromagnetic analysis with the Sonnet software. The superconducting-circuit consisted of a transmon qubit, strongly coupled to a readout resonator for the measurement of the qubit state, and a weakly coupled driving resonator for controlling the state of the qubit. Guided by the results from the numerical simulations, we targeted a coupling strength of $g_{\mathrm{dr}}/2\pi = 7.5\,\mathrm{MHz}$ for the driving resonator and $g_{\mathrm{dr}}/2\pi = 150\,\mathrm{MHz}$ for the readout resonator. The designed layout was imprinted on a photomask for the fabrication of the superconducting-circuit using the optical lithography process.

The fabricated sample was characterized to extract the parameters that were essential for

carrying out the quantum driving experiments. While targeting a lower coupling strength for the driving resonator, we significantly reduced the charging energy of the transmon qubit. Unfortunately, the charging energy also dictates the transmon frequency and the anharmonicity between the adjacent transition frequencies. Consequently, this rendered the sample unfeasible for the quantum driving experiments. However, we have utilized an alternative sample with the similar design as the quantum driving sample for carrying out the photon calibration measurement. The alternative sample provides an increased anharmonicity but strongly coupled transmon to the driving resonator.

First, we carried out the power spectroscopy of the resonator by varying the attenuation in the drive line, while probing the resonator transmission. We observed a nonlinear vacuum Rabi splitting at lower values of the attenuation. We performed a similar measurement for the calibration of the photon occupation in the resonator by studying the ac Stark shift of the transmon frequency as a function of the attenuation. In the dispersive regime, the transmon frequency acquires a shift of 2χ per photon, thus giving us a measure of the average photon occupation in the resonator as a function of the attenuation values.

Although we still haven't managed to experimentally demonstrate the proposed gate protocol, the work carried out during the course of this thesis provides a concrete foundation for the future work. Firstly, we have already designed and fabricated a second version of the quantum driving sample by resolving the low charging energy issue present in the first version. Secondly, we have also identified some of the details in the current measurement setup that require modifications for the execution of the quantum driving experiments. In particular, the current setup does not allow to work with a microwave pulse of lengths larger than $4\,\mu$s for the resonator drive line. We require a long drive pulse for an improved photon calibration measurement, as the long pulse to the resonator ensures that the transmon occupies an excited state.

Finally, we make couple of remarks about the possible issues that may arise in the practical implementations of the quantum driving experiments. The flux spectroscopy mediating the resonant interaction may not work if the resonator is far-detuned from the transmon. Since, operating the transmon far from the sweet spot may lead to a drastic flux noise. We also acknowledge that there is an upper bound for the average photon occupation in the resonator set by the strong drive limit. Since the strongly driven transmon–resonator system can no longer be described by a two-level system, we are required to operate in the linear regime to avoid the nonlinear Rabi splitting of the transmission peak of the resonator. The imposed restriction on the photon occupation also sets a limit on the gate error that can be obtained experimentally.

REFERENCES

[1] Landauer, R. The physical nature of information. *Physics Letters, Section A: General, Atomic and Solid State Physics* (1996). ISSN: 03759601. DOI: `10.1016/0375-9601(96)00453-7`.

[2] Landauer, R. Information is physical. *Proceedings of the Workshop on Physics and Computation, PhysComp 1992*. 1992. ISBN: 0818634200. DOI: `10.1109/PHYCMP.1992.615478`.

[3] Benioff, P. The computer as a physical system: A microscopic quantum mechanical Hamiltonian model of computers as represented by Turing machines. *Journal of Statistical Physics* (1980). ISSN: 00224715. DOI: `10.1007/BF01011339`.

[4] Bennett, C. H. *The thermodynamics of computation-a review*. 1982. DOI: `10.1007/BF02084158`.

[5] Feynman, R. P. Simulating physics with computers. *International Journal of Theoretical Physics* (1982). ISSN: 00207748. DOI: `10.1007/BF02650179`.

[6] Deutsch, D. Quantum theory as a universal physical theory. *International Journal of Theoretical Physics* (1985). ISSN: 00207748. DOI: `10.1007/BF00670071`.

[7] Shor, P. Algorithms for quantum computation: discrete logarithms and factoring. 1994. DOI: `10.1109/sfcs.1994.365700`.

[8] Grover, L. K. Quantum mechanics helps in searching for a needle in a haystack. *Physical Review Letters* (1997). ISSN: 10797114. DOI: `10.1103/PhysRevLett.79.325`.

[9] Bennett, C. H., Brassard, G. and Mermin, N. D. Quantum cryptography without Bell's theorem. *Physical Review Letters* (1992). ISSN: 00319007. DOI: `10.1103/PhysRevLett.68.557`.

[10] Bennett, C. H. and Brassard, G. Quantum cryptography: Public key distribution and coin tossing. *Theoretical Computer Science* (2014). ISSN: 03043975. DOI: `10.1016/j.tcs.2014.05.025`.

[11] DiVincenzo, D. P. *The physical implementation of quantum computation*. 2000. DOI: `10.1002/1521-3978(200009)48:9/11<771::AID-PROP771>3.0.CO;2-E`. arXiv: `0002077 [quant-ph]`.

[12] Cirac, J. I. and Zoller, P. Quantum computations with cold trapped ions. *Physical Review Letters* (1995). ISSN: 00319007. DOI: `10.1103/PhysRevLett.74.4091`.

[13] Nayak, C., Simon, S. H., Stern, A., Freedman, M. and Das Sarma, S. Non-Abelian anyons and topological quantum computation. *Reviews of Modern Physics* (2008). ISSN: 00346861. DOI: `10.1103/RevModPhys.80.1083`. arXiv: `0707.1889`.

[14] Ogburn, R. W. and Preskill, J. Topological quantum computation. *Lecture Notes in Computer Science (including subseries Lecture Notes in Artificial Intelligence and Lecture Notes in Bioinformatics)*. 1999. ISBN: 354065514X. DOI: `10.1201/9781315181509-14`. arXiv: `0101025 [quant-ph]`.

[15] Loss, D. and DiVincenzo, D. P. Quantum computation with quantum dots. *Physical Review A - Atomic, Molecular, and Optical Physics* (1998). ISSN: 10941622. DOI: `10.1103/PhysRevA.57.120`. arXiv: `9701055 [cond-mat]`.

[16] Gershenfeld, N. A. and Chuang, I. L. Bulk spin-resonance quantum computation. *Science* (1997). ISSN: 00368075. DOI: `10.1126/science.275.5298.350`.

[17] Knill, E., Laflamme, R. and Milburn, G. J. A scheme for efficient quantum computation with linear optics. *Nature* (2001). ISSN: 00280836. DOI: `10.1038/35051009`.

[18] Bouchiat, V., Vion, D., Joyez, P., Esteve, D. and Devoret, M. H. Quantum coherence with a single cooper pair. *Physica Scripta T* (1998). ISSN: 02811847. DOI: `10.1238/physica.topical.076a00165`.

[19] Devoret, M. H. and Martinis, J. M. Implementing qubits with superconducting integrated circuits. *Quantum Information Processing* (2004). ISSN: 15700755. DOI: `10.1007/s11128-004-3101-5`.

[20] Wallraff, A., Schuster, D. I., Blais, A., Frunzio, L., Huang, R. S., Majer, J., Kumar, S., Girvin, S. M. and Schoelkopf, R. J. Strong coupling of a single photon to a superconducting qubit using circuit quantum electrodynamics. *Nature* (2004). ISSN: 00280836. DOI: `10.1038/nature02851`.

[21] Vandersypen, L. M., Breyta, M., Steffen, G., Yannoni, C. S., Sherwood, M. H. and Chuang, I. L. Experimental realization of Shor's quantum factoring algorithm using nuclear magnetic resonance. *Nature* (2001). ISSN: 00280836. DOI: `10.1038/414883a`. arXiv: `0112176 [quant-ph]`.

[22] Arute, F., Arya, K., Babbush, R., Bacon, D., Bardin, J. C., Barends, R., Biswas, R., Boixo, S., Brandao, F. G., Buell, D. A., Burkett, B., Chen, Y., Chen, Z., Chiaro, B., Collins, R., Courtney, W., Dunsworth, A., Farhi, E., Foxen, B., Fowler, A., Gidney, C., Giustina, M., Graff, R., Guerin, K., Habegger, S., Harrigan, M. P., Hartmann, M. J., Ho, A., Hoffmann, M., Huang, T., Humble, T. S., Isakov, S. V., Jeffrey, E., Jiang, Z., Kafri, D., Kechedzhi, K., Kelly, J., Klimov, P. V., Knysh, S., Korotkov, A., Kostritsa, F., Landhuis, D., Lindmark, M., Lucero, E., Lyakh, D., Mandrà, S., McClean, J. R., McEwen, M., Megrant, A., Mi, X., Michielsen, K., Mohseni, M., Mutus, J., Naaman, O., Neeley, M., Neill, C., Niu, M. Y., Ostby, E., Petukhov, A., Platt, J. C., Quintana, C., Rieffel, E. G., Roushan, P., Rubin, N. C., Sank, D., Satzinger, K. J., Smelyanskiy, V., Sung, K. J., Trevithick, M. D., Vainsencher, A., Villalonga, B., White, T., Yao, Z. J., Yeh, P., Zalcman, A., Neven, H. and Martinis, J. M. Quantum supremacy using a programmable superconducting processor. *Nature* (2019). ISSN: 14764687. DOI: `10.1038/s41586-019-1666-5`.

[23] Shor, P. W. Fault-tolerant quantum computation. *Annual Symposium on Foundations of Computer Science - Proceedings*. 1996. DOI: `10.1142/9789812385253_0008`. arXiv: `9712048` [`quant-ph`].

[24] Campbell, E. T., Terhal, B. M. and Vuillot, C. *Roads towards fault-tolerant universal quantum computation*. 2017. DOI: `10.1038/nature23460`. arXiv: `1612.07330`.

[25] Koch, J., Yu, T. M., Gambetta, J., Houck, A. A., Schuster, D. I., Majer, J., Blais, A., Devoret, M. H., Girvin, S. M. and Schoelkopf, R. J. Charge-insensitive qubit design derived from the Cooper pair box. *Physical Review A - Atomic, Molecular, and Optical Physics* (2007). ISSN: 10502947. DOI: `10.1103/PhysRevA.76.042319`. arXiv: `0703002` [`cond-mat`].

[26] Barends, R., Kelly, J., Megrant, A., Sank, D., Jeffrey, E., Chen, Y., Yin, Y., Chiaro, B., Mutus, J., Neill, C., O'Malley, P., Roushan, P., Wenner, J., White, T. C., Cleland, A. N. and Martinis, J. M. Coherent josephson qubit suitable for scalable quantum integrated circuits. *Physical Review Letters* (2013). ISSN: 00319007. DOI: `10.1103/PhysRevLett.111.080502`. arXiv: `1304.2322`.

[27] Nakamura, Y., Pashkin, Y. A. and Tsai, J. S. Coherent control of macroscopic quantum states in a single-Cooper-pair box. *Nature* (1999). ISSN: 00280836. DOI: `10.1038/19718`. arXiv: `9904003` [`cond-mat`].

[28] Barends, R., Kelly, J., Megrant, A., Veitia, A., Sank, D., Jeffrey, E., White, T. C., Mutus, J., Fowler, A. G., Campbell, B., Chen, Y., Chen, Z., Chiaro, B., Dunsworth, A., Neill, C., O'Malley, P., Roushan, P., Vainsencher, A., Wenner, J., Korotkov, A. N., Cleland, A. N. and Martinis, J. M. Superconducting quantum circuits at the surface code threshold for fault tolerance. *Nature* (2014). ISSN: 14764687. DOI: `10.1038/nature13171`.

[29] Ghirardi, G. and Silverman, M. P. Sneaking A Look At God's Cards: Unraveling The Mysteries of Quantum Mechanics (translation). *American Journal of Physics* (2005). ISSN: 0002-9505. DOI: `10.1119/1.1904624`.

[30] Nielsen, M. A. and Chuang, I. L. *Quantum computation and quantum information*. 2000. ISBN: 9780521635035. DOI: `10.2277/0521635039`.

[31] Sakurai, J. J. and Commins, E. D. Modern Quantum Mechanics, Revised Edition. *American Journal of Physics* (1995). ISSN: 0002-9505. DOI: `10.1119/1.17781`.

[32] Nakahara, M. and Ohmi, T. *Quantum computing: From linear algebra to physical realizations*. 2008, 1–422. ISBN: 9781420012293.

[33] Goldstein, H., Poole, C., Safko, J. and Addison, S. R. Classical Mechanics, 3rd ed. *American Journal of Physics* (2002). ISSN: 0002-9505. DOI: `10.1119/1.1484149`.

[34] Dirac, P. A. M. *The Principles of Quantum Mechanics*. Comparative Pathobiology - Studies in the Postmodern Theory of Education. Clarendon Press, 1981. ISBN: 9780198520115. URL: `https://books.google.fi/books?id=XehUpGiM6FIC`.

[35] Gerry, C. and Knight, P. *Introductory Quantum Optics*. 3rd ed. Cambridge University Press, 2004. ISBN: 978-0-521-52735-4.

[36]   Breuer, H. P. and Petruccione, F. *The Theory of Open Quantum Systems*. 2007. ISBN: 9780191706349. DOI: `10.1093/acprof:oso/9780199213900.001.0001`.

[37]   Ikonen, J., Salmilehto, J. and Möttönen, M. Energy-efficient quantum computing. *npj Quantum Information* (2017). ISSN: 20566387. DOI: `10.1038/s41534-017-0015-5`. arXiv: `1609.02732`.

[38]   Gilchrist, A., Langford, N. K. and Nielsen, M. A. Distance measures to compare real and ideal quantum processes. *Physical Review A - Atomic, Molecular, and Optical Physics* (2005). ISSN: 10941622. DOI: `10.1103/PhysRevA.71.062310`. arXiv: `0408063` [quant-ph].

[39]   Haroche, S. and Raimond, J. M. *Exploring the Quantum: Atoms, Cavities, and Photons*. 2010. ISBN: 9780191708626. DOI: `10.1093/acprof:oso/9780198509141.001.0001`.

[40]   Bouwmeester, D., Pan, J. W., Mattle, K., Eibl, M., Weinfurter, H. and Zeilinger, A. Experimental quantum teleportation. *Nature* (1997). ISSN: 00280836. DOI: `10.1038/37539`. arXiv: `1901.11004`.

[41]   Brune, M., Hagley, E., Dreyer, J., Maître, X., Maali, A., Wunderlich, C., Raimond, J. M. and Haroche, S. Observing the progressive decoherence of the "meter" in a quantum measurement. *Physical Review Letters* (1996). ISSN: 10797114. DOI: `10.1103/PhysRevLett.77.4887`.

[42]   Pellizzari, T., Gardiner, S. A., Cirac, J. I. and Zoller, P. Decoherence, continuous observation, and quantum computing: A cavity QED model. *Physical Review Letters* (1995). ISSN: 00319007. DOI: `10.1103/PhysRevLett.75.3788`.

[43]   Turchette, Q. A., Hood, C. J., Lange, W., Mabuchi, H. and Kimble, H. J. Measurement of conditional phase shifts for quantum logic. *Physical Review Letters* (1995). ISSN: 00319007. DOI: `10.1103/PhysRevLett.75.4710`.

[44]   Blais, A., Huang, R. S., Wallraff, A., Girvin, S. M. and Schoelkopf, R. J. Cavity quantum electrodynamics for superconducting electrical circuits: An architecture for quantum computation. *Physical Review A - Atomic, Molecular, and Optical Physics* (2004). ISSN: 10502947. DOI: `10.1103/PhysRevA.69.062320`. arXiv: `0402216` [cond-mat].

[45]   Pozar, D. M. *Microwave Engineering, 4th Edition*. 2012. ISBN: 978-0-470-63155-3.

[46]   Göppl, M., Fragner, A., Baur, M., Bianchetti, R., Filipp, S., Fink, J. M., Leek, P. J., Puebla, G., Steffen, L. and Wallraff, A. Coplanar waveguide resonators for circuit quantum electrodynamics. *Journal of Applied Physics* (2008). ISSN: 00218979. DOI: `10.1063/1.3010859`. arXiv: `0807.4094`.

[47]   Greiner, W. and Reinhardt, J. *Field Quantization*. 1996. DOI: `10.1007/978-3-642-61485-9`.

[48]   Tinkham, M. and Emery, V. Introduction to Superconductivity. *Physics Today* (1996). ISSN: 0031-9228. DOI: `10.1063/1.2807811`.

[49] Kittel, C. Introduction to Solid State Physics, 8th edition. *Wiley & Sons, New York, NY* (2004).

[50] Buttiker, M. Zero-current persistent potential drop across small-capacitance josephson junctions. *Physical Review B* (1987). ISSN: 01631829. DOI: `10.1103/PhysRevB.36.3548`.

[51] Cohen-Tannoudji, C., Diu, B. and Laloe, F. *Quantum Mechanics, Volume 2: Angular Momentum, Spin, and Approximation Methods*. 2nd. New York: John Wiley & Sons, New York, 1997. ISBN: 978-3-527-34554-0.

[52] Jones, P. J., Salmilehto, J. and Möttönen, M. Highly controllable qubit-bath coupling based on a sequence of resonators. *Journal of Low Temperature Physics* (2013). ISSN: 00222291. DOI: `10.1007/s10909-013-0889-3`. arXiv: `1304.4829`.

[53] Shore, B. W. and Knight, P. L. The Jaynes–Cummings model. *Journal of Modern Optics* (1993). ISSN: 13623044. DOI: `10.1080/09500349314551321`.

[54] Blais, A., Gambetta, J., Wallraff, A., Schuster, D. I., Girvin, S. M., Devoret, M. H. and Schoelkopf, R. J. Quantum-information processing with circuit quantum electrodynamics. *Physical Review A - Atomic, Molecular, and Optical Physics* (2007). ISSN: 10502947. DOI: `10.1103/PhysRevA.75.032329`. arXiv: `0612038 [cond-mat]`.

[55] Glauber, R. J. Coherent and incoherent states of the radiation field. *Physical Review* (1963). ISSN: 0031899X. DOI: `10.1103/PhysRev.131.2766`.

[56] Braginsky, V. B., Vorontsov, Y. I. and Thorne, K. S. Quantum nondemolition measurements. *Science* (1980). ISSN: 00368075. DOI: `10.1126/science.209.4456.547`.

[57] Lupaşcu, A., Saito, S., Picot, T., De Groot, P. C., Harmans, C. J. and Mooij, J. E. Quantum non-demolition measurement of a superconducting two-level system. *Nature Physics* (2007). ISSN: 17452481. DOI: `10.1038/nphys509`.

[58] Reed, M. D., Johnson, B. R., Houck, A. A., Dicarlo, L., Chow, J. M., Schuster, D. I., Frunzio, L. and Schoelkopf, R. J. Fast reset and suppressing spontaneous emission of a superconducting qubit. *Applied Physics Letters* (2010). ISSN: 00036951. DOI: `10.1063/1.3435463`. arXiv: `1003.0142`.

[59] Houck, A. A., Schreier, J. A., Johnson, B. R., Chow, J. M., Koch, J., Gambetta, J. M., Schuster, D. I., Frunzio, L., Devoret, M. H., Girvin, S. M. and Schoelkopf, R. J. Controlling the spontaneous emission of a superconducting transmon qubit. *Physical Review Letters* (2008). ISSN: 00319007. DOI: `10.1103/PhysRevLett.101.080502`. arXiv: `0803.4490`.

[60] Krantz, P., Kjaergaard, M., Yan, F., Orlando, T. P., Gustavsson, S. and Oliver, W. D. A quantum engineer's guide to superconducting qubits. *Applied Physics Reviews* (2019). ISSN: 19319401. DOI: `10.1063/1.5089550`. arXiv: `1904.06560`.

[61] Johansson, R. and Nation, P. QuTiP: A framework for the dynamics of open quantum systems using SciPy and Cython. *Proceedings of the 11th Python in Science Conference*. 2012. DOI: `10.25080/majora-54c7f2c8-00a`.

[62] Johansson, J. R., Nation, P. D. and Nori, F. QuTiP: An open-source Python framework for the dynamics of open quantum systems. *Computer Physics Communications* (2012). ISSN: 00104655. DOI: 10.1016/j.cpc.2012.02.021. arXiv: 1110.0573.

[63] Johansson, J. R., Nation, P. D. and Nori, F. QuTiP 2: A Python framework for the dynamics of open quantum systems. *Computer Physics Communications* (2013). ISSN: 00104655. DOI: 10.1016/j.cpc.2012.11.019. arXiv: 1211.6518.

[64] Sonnet. *High Frequency Electromagnetic Software SONNET Suites*. North Syracuse, NY, 2017.

[65] Barrington, R. F. *Field computation by moment methods*. 1993. ISBN: 9780470544631. DOI: 10.1109/9780470544631.

[66] Rautio, J. C. and Harrington, R. F. *An electromagnetic time-harmonic analysis of shielded microstrip circuits*. 1987. DOI: 10.1109/TMTT.1987.1133738.

[67] Gubin, A. I., Il'in, K. S., Vitusevich, S. A., Siegel, M. and Klein, N. Dependence of magnetic penetration depth on the thickness of superconducting Nb thin films. *Physical Review B - Condensed Matter and Materials Physics* (2005). ISSN: 10980121. DOI: 10.1103/PhysRevB.72.064503.

[68] Watanabe, K., Yoshida, K. and Aoki, T. Kinetic inductance of superconducting coplanar waveguides. *Japanese Journal of Applied Physics* 33.10R (1994), 570–572. ISSN: 13474065. DOI: 10.1143/JJAP.33.5708.

[69] Heinsoo, J., Andersen, C. K., Remm, A., Krinner, S., Walter, T., Salathé, Y., Gasparinetti, S., Besse, J. C., Potočnik, A., Wallraff, A. and Eichler, C. Rapid High-fidelity Multiplexed Readout of Superconducting Qubits. *Physical Review Applied* (2018). ISSN: 23317019. DOI: 10.1103/PhysRevApplied.10.034040. arXiv: 1801.07904.

[70] Ambegaokar, V. and Baratoff, A. Tunneling between superconductors. *Physical Review Letters* (1963). ISSN: 00319007. DOI: 10.1103/PhysRevLett.11.104.

[71] Likharev, K. K. Superconducting weak links. *Reviews of Modern Physics* (1979). ISSN: 00346861. DOI: 10.1103/RevModPhys.51.101.

[72] Bronn, N. T., Magesan, E., Masluk, N. A., Chow, J. M., Gambetta, J. M. and Steffen, M. Reducing Spontaneous Emission in Circuit Quantum Electrodynamics by a Combined Readout/Filter Technique. *IEEE Transactions on Applied Superconductivity* (2015). ISSN: 10518223. DOI: 10.1109/TASC.2015.2456109. arXiv: 1504.04353.

[73] Cleland, A. Y., Pechal, M., Stas, P. J. C., Sarabalis, C. J., Wollack, E. A. and Safavi-Naeini, A. H. Mechanical Purcell filters for microwave quantum machines. *Applied Physics Letters* (2019). ISSN: 00036951. DOI: 10.1063/1.5111151. arXiv: 1905.08403.

[74] Bronn, N. T., Liu, Y., Hertzberg, J. B., Córcoles, A. D., Houck, A. A., Gambetta, J. M. and Chow, J. M. Broadband filters for abatement of spontaneous emission in circuit

quantum electrodynamics. *Applied Physics Letters* (2015). ISSN: 00036951. DOI: 10.1063/1.4934867. arXiv: 1508.01743.

[75]　Fedorov, G. P. and Ustinov, A. V. Automated analysis of single-tone spectroscopic data for cQED systems. *Quantum Science and Technology* (2019). ISSN: 20589565. DOI: 10.1088/2058-9565/ab478b. arXiv: 1907.05198.

[76]　Burnett, J. J., Bengtsson, A., Scigliuzzo, M., Niepce, D., Kudra, M., Delsing, P. and Bylander, J. Decoherence benchmarking of superconducting qubits. *npj Quantum Information* (2019). ISSN: 20566387. DOI: 10.1038/s41534-019-0168-5. arXiv: 1901.04417.

[77]　Ramsey, N. F. A molecular beam resonance method with separated oscillating fields. *Physical Review* (1950). ISSN: 0031899X. DOI: 10.1103/PhysRev.78.695.

[78]　Clemmen, S., Farsi, A., Ramelow, S. and Gaeta, A. L. Ramsey Interference with Single Photons. *Physical Review Letters* (2016). ISSN: 10797114. DOI: 10.1103/PhysRevLett.117.223601.

[79]　Bishop, L. S., Chow, J. M., Koch, J., Houck, A. A., Devoret, M. H., Thuneberg, E., Girvin, S. M. and Schoelkopf, R. J. Nonlinear response of the vacuum Rabi resonance. *Nature Physics* (2009). ISSN: 17452481. DOI: 10.1038/nphys1154. arXiv: 0807.2882.